Final Progress Report to
NASA MARSHALL SPACE FLIGHT CENTER
Dr. Robert Thom
Non-Destructive Testing and Tribology Research Branch
NASA Marshall Space Flight Center
Mail Code EH-13, Huntsville, ALABAMA 85812

BULK-FLOW ANALYSIS OF HYBRID THRUST BEARINGS FOR ADVANCED CRYOGENIC TURBOPUMPS

By
Dr. Luis San Andrés,
Principal Investigator
Mechanical Engineering Department
Texas A&M University
College Station, TX 77843-3123
phone (409) 845-0160
LsanAndres@Mengr.tamu.edu

NASA MSFC grant NAG8-1395

September 30, 1998

BULK-FLOW ANALYSIS OF HYBRID THRUST BEARINGS FOR ADVANCED CRYOGENIC TURBOPUMPS

LUIS SAN ANDRÉS, PRINCIPAL INVESTIGATOR

EXECUTIVE SUMMARY

A bulk-flow analysis and computer program for prediction of the static load performance and dynamic force coefficients of angled injection, orifice-compensated hydrostatic / hydrodynamic thrust bearings have been completed. The product of the research is an efficient computational tool for the design of high-speed thrust bearings for cryogenic fluid turbopumps. The study addresses the needs of a growing technology that requires of reliable fluid film bearings to provide the maximum operating life with optimum controllable rotordynamic characteristics at the lowest cost.

The motion of a cryogenic fluid on the thin film lands of a thrust bearing is governed by a set of bulk-flow mass and momentum conservation and energy transport equations. Mass flow conservation and a simple model for momentum transport within the hydrostatic bearing recesses are also accounted for. The bulk-flow model includes flow turbulence with fluid inertia advection, Coriolis and centrifugal acceleration effects on the bearing recesses and film lands. The cryogenic fluid properties are obtained from realistic thermophysical equations of state. Turbulent bulk-flow shear parameters are based on Hirs' model with Moody's friction factor equations allowing a simple simulation for machined bearing surface roughness. A perturbation analysis leads to zeroth-order nonlinear equations governing the fluid flow for the thrust bearing operating at a static equilibrium position, and first-order linear equations describing the perturbed fluid flow for small amplitude shaft motions in the axial direction. Numerical solution to the zeroth-order flow field equations renders the bearing flow rate, thrust load, drag torque and power dissipation. Solution to the first-order equations determines the axial stiffness, damping and inertia force coefficients. The computational method uses well established algorithms and generic subprograms available from prior developments.

The Fortran90 computer program *hydrothrust* runs on a Windows 95/NT personal computer. The program, help files and examples are licensed by Texas A&M University Technology License Office.

The study of the static and dynamic performance of two hydrostatic/hydrodynamic bearings demonstrates the importance of centrifugal and advection fluid inertia effects for operation at high rotational speeds. The first example considers a conceptual hydrostatic thrust bearing for an advanced liquid hydrogen turbopump operating at 170,000 rpm. The large axial stiffness and damping coefficients of the bearing should provide accurate control and axial positioning of the turbopump and also allow for unshrouded impellers, therefore increasing the overall pump efficiency. The second bearing uses a refrigerant R134a, and its application in oil-free air conditioning compressors is of great technological importance and commercial value.

The computed predictions reveal that the LH_2 bearing load capacity and flow rate increase with the recess pressure (i.e. increasing orifice diameters). The bearing axial

stiffness has a maximum for a recess pressure ratio ~0.55, while the axial damping coefficient decreases as the recess pressure ratio increases. The computer results from three flow models are compared. These models are a) inertialess, b) fluid inertia at recess edges only, and c) full fluid inertia at both recess edges and film lands. The full inertia model shows the lowest flow rates, axial load capacity and stiffness coefficient but on the other hand renders the largest damping coefficients and inertia coefficients. The most important findings are related to the reduction of the outflow through the inner radius and the appearance of subambient pressures.

The performance of the refrigerant hybrid thrust bearing is evaluated at two operating speeds and pressure drops. The computed results are presented in dimensionless form to evidence consistent trends in the bearing performance characteristics. As the applied axial load increases, the bearing film thickness and flow rate decrease while the recess pressure increases. The axial stiffness coefficient shows a maximum for a certain intermediate load while the damping coefficient steadily increases. The computed results evidence the paramount of centrifugal fluid inertia at low recess pressures (i.e. low loads), and where there is actually an inflow through the bearing inner diameter, accompanied by subambient pressures just downstream of the bearing recess edge. These results are solely due to centrifugal fluid inertia and advection transport effects.

Recommendations include the extension of the computer program to handle flexure pivot tilting pad hybrid bearings and the ability to calculate moment coefficients for shaft angular misalignments.

NOMENCLATURE

A_o	$(\pi d_o^2/4)$. Effective orifice area [m^2].
A_B	$\pi\,(R_{out}^2 - R_{in}^2\,)$. Bearing surface area [m^2].
A_R	$\frac{1}{2}\Theta_R\left(R_{Ro}^2 - R_{Ri}^2\right) = \frac{1}{2}\Theta_R\, D_R\, l_R$. Recess (pocket) area [m^2].
	$\overline{A}_R = A_R / R_*^2$
b_R	recess arc length [m]. $\overline{b}_R = b_R / R_*$
C	H_2. Nominal (minimum) film clearance [m].
C_p	Fluid specific heat [J/kg · °K]. $\overline{C}_p = C_p / C_{p*}$
C_d	Orifice discharge coefficient.
C_{ZZ}	Damping force coefficient [Ns/m]. $\overline{C}_{ZZ} = C_{ZZ}\, C\Omega / \left[A_B\left(P_s - P_a\right)\right]$
C_d	Orifice discharge coefficient
D_{out}	$2 \cdot R_{out}$. Bearing outer diameter [m].
D_{in}	$2 \cdot R_{in}$. Bearing inner diameter [m].
D_R	$2 \cdot R_R$. Recess center diameter [m].
d_o	Orifice diameter [m]
E_c	$\frac{U_*}{T_* C_{p*}}$. Eckert heat transfer dimensionless number.
F_Z	Fluid film axial force [N]. $\overline{F}_Z = F_Z / \left[A_B\left(P_s - P_a\right)\right]$
$f_{S,B}$	$a_M\left[1 + \left(c_M \frac{r_{S,B}}{H} + \frac{b_M}{Re_{S,B}}\right)^{e_M}\right]$; $a_M = 0.001375$, $b_M = 5 \cdot 10^5$; $c_M = 1 \cdot 10^4$, $e_M = \frac{1}{3}$
	Turbulent flow Moody's friction factors at shaft and bearing surfaces.
H,h	Film thickness [m], H/C_*
$H_{1,2,3,4}$	Pad film thickness at leading edge, trailing edge, and midplane inner and outer radius [m].
H_B,H_S	convection heat flow coefficients on bearing and shaft surfaces [watt/m^2°K]. $\overline{H}_B = H_B / H_{B*}$; $\overline{H}_S = H_S / H_{S*}$
H_R	Recess depth [m]. $h_R = H_R / C$

h_1	$\frac{\Delta z}{C}$. Small perturbation in axial displacement (dimensionless).
K_{ZZ}	Stiffness force coefficient [N/m]. $\overline{K}_{ZZ} = K_{ZZ}\, C / \left[A_B \left(P_s - P_a\right)\right]$
L	$(R_{out} - R_{in})$. Bearing radial length [m].
l_R	$(R_{Ro} - R_{Ri})$. Recess radial length [m].
M	Bearing mass flow rate [kg/s].
M_{Rin}, M_{Rout}	Mass flow rates through inner and outer diameters of bearing [kg/s].
M_R	Mass flow through recess orifice [kg/s]. $\overline{M}_R = M_R / \left(\rho_* U_* C\, R_*\right)$
M_Γ	$\oint_\Gamma \rho H \vec{U} \cdot \vec{\eta}\; d\Gamma$. Mass flow from recess boundary into to film lands [kg/s]. $\overline{M}_\Gamma = M_\Gamma / \left(\rho_* U_* C\, R_*\right)$
M_{ZZ}	Inertia force coefficient [kg]. $\overline{M}_{ZZ} = M_{ZZ}\, C\Omega^2 / \left[A_B \left(P_s - P_a\right)\right]$
N_{rec}	Number of hydrostatic recesses (pockets) on bearing pad.
N_{pad}	Number of pads on bearing.
P, $\overline{P}$	Fluid pressure [N/m^2], $(P-P_a)/(P_s-P_a)$.
P_R, P_s	Recess pressure, supply pressure [N/m^2].
P_{Re}^- , P_{Re}^+	Edge recess pressures [N/m^2].
P_{Din} , P_{Dout}	Fluid pressures at inner and outer bearing diameters [N/m^2].
P_a	Characteristic pressure, MIN[P_{Din} , P_{Dout}] [N/m^2].
P_{dyn}	$\frac{1}{2} \Delta(\forall \Sigma R_R)^2$. Pressure due to centrifugal inertia effect at pocket radius
Q_{BS}	$Q_B + Q_S$. Radial heat flow through bearing, $Q_B = H_B(T-T_B)$, and shaft, $Q_S = H_S(T-T_S)$, surfaces [watt/m^2].
R,r	Radial coordinate [m], R / R_*.
R_*	R_{out}. Characteristic bearing radius [m].
Re	$\left(\rho_* \Omega\, R_* C / \mu_*.\right)$ Nominal circumferential flow Reynolds number.
Re_p	$\left(\rho_* U_* C / \mu_*\right)$. Nominal pressure flow Reynolds number.
Re_{p*}	$\left(Re_p\, C / R_*\right)$. Nominal modified pressure flow Reynolds number.
Re_Φ	$\left(\rho_* \omega C^2 / \mu_* = \sigma\, Re_{p*}\right)$. Squeeze film Reynolds number.
Re_B,Re_S	$(\Delta H/:) [U_R^2 + U_2^2]^{1/2}$, $(\Delta H/:) [U_R^2 + (U_2 - \Sigma R)^2]^{1/2}$

	Flow Reynolds numbers relative to bearing and shaft surfaces.
r_S, r_B	Roughness depths of shaft and bearing surfaces [m].
s	R/R_R. Local radial coordinate from pocket radius.
t	Time [s].
$T, \overline{T}$	Temperature, $\overline{T} = T / T_s$
T_s	Fluid supply temperature [°K].
T_B, T_S	bearing and shaft surface temperatures [°K].
T_o	Shear induced torque on bearing surface [Nm]. $\overline{T_o} = T_o C / \left(\mu_* U_* R_*^3\right)$
U_*	$C^2\left(P_s - P_a\right) / \mu_* R_*$. Characteristic fluid flow velocity [m/s].
U_r,U_2	Bulk-flow velocities in radial and circumferential directions [m/s].
u_r,u_2	$U_r / U_*, U_\theta / U_*$. Dimensionless radial and tangential velocities
V_R	$[A_R(H+H_R)+V_{supply}]$. Recess volume including supply line volume [m^3]. $\overline{V_R} = V_R / R_*^2 C$
W_Z	External axial load on bearing [N]. $\overline{W_Z} = W_Z / \left[A_B\left(P_s - P_a\right)\right]$
α	Fluid inlet swirl ratio at recess.
β_P	$+(1/\rho)(\partial\rho/\partial P)$. Liquid compressibility coefficient [m^2/N].
β_T	$-(1/\rho)(\partial\rho/\partial T)$. Liquid volumetric expansion coefficient [1/°K].
$*_2$, $*_r$	$(H_1-H_2)/C$, $(H_3-H_4)/C$. Pad circumferential and radial tapers [-].
$)\vartheta_{rZ}$,$)\vartheta_{2Z}$	$\frac{\mu}{H} k_r U_r ; \frac{\mu}{H}\left(k_\theta U_\theta - \frac{1}{2} k_S \Omega R\right)$ Wall shear stress differences in radial and circumferential directions [N/m^2].
$\tau_{\theta R}\|^H$	$\frac{1}{2}\frac{H}{R}\frac{\partial P}{\partial \theta} + \frac{\mu}{4H}\left\{\kappa_\theta U_\theta - \kappa_S\left(U_\theta - \Omega R\right)\right\}$. Turbulent wall shear stress at runner surface [N/m^2].
δ_{Ro}	$\frac{C_d A_o \left(2\rho_*\left[P_s - P_a\right]\right)^{1/2}}{\left(\rho U C R\right)_*}$. Dimensionless feed orifice coefficient.
(	First order shear coefficients (Appendix A).
$\kappa_r = \kappa_2$	$½(\kappa_S + \kappa_B)$. Turbulence shear factors in $(r,2)$ flow directions.

κ_S, κ_B	$f_S \cdot Re_S$, $f_B \cdot Re_B$. Turbulent shear parameters at shaft and bearing.
ρ, μ	Fluid density [kg/m^3], viscosity [Ns/m^2].
$\mathcal{2}$	circumferential coordinate [rad].
Θ_P	angular extent of a bearing pad [rad].
Θ_{l_pad}	Leading edge of a bearing pad [rad].
Θ_R	angular extent of hydrostatic recess (pocket) [rad].
ξ_{xu}, ξ_{xd}	Empirical recess-edge entrance loss coefficients in circumferential (upstream, downstream) direction.
ξ_{ri}, ξ_{ro}	Empirical recess-edge entrance loss coefficients in radial direction, inner and outer radii boundaries.
ϑ	Tt. Dimensionless time.
$\mathcal{7},\Phi$	$\Omega R_* / U_*$; $\omega R_* / U_*$. Circumferential speed and whirl frequency numbers
Ω, ω	shaft rotational speed, excitation or whirl frequency [rad/s]

Subscripts refer to:

o	recess feed orifice
s	Refer to pressure supply condition.
0,1	zeroth and first-order variables.
R,e	Bearing recesses and edges (entrance).
u,d	Upstream and downstream of recess.
B,S	Refer to bearing and shaft (collar) surfaces.

Overbar denotes dimensionless variable

TABLE OF CONTENTS

	page
EXECUTIVE SUMMARY	i
NOMENCLATURE	iii
LIST OF TABLES	vii
LIST OF FIGURES	vii
ACKNOWLEDGEMENTS	viii
INTRODUCTION	1
ANALYSIS	3
Bulk-flow equations on the film lands of a hydrostatic thrust bearing	3
Bulk-flow equations at the recess of a hydrostatic thrust bearing	5
Governing equations in dimensionless form	7
Film thickness expression and boundary conditions	9
Perturbation analysis of the flow field	11
Zeroth-order bulk-flow equations on the film lands	
First-order bulk-flow equations on the film lands	
Zeroth- and first-order flow equations at a bearing recess	
Fluid film reaction force and axial force coefficients	14
Numerical method of solution of flow equations on the film lands	15
The iterative scheme for balance of flow at bearing recesses	17
Numerical solution of the first-order bulk-flow equations	19
THE COMPUTER PROGRAM HYDROTHRUST	21
NUMERICAL RESULTS AND DISCUSSION	21
Example of a hydrostatic thrust bearing for a cryogenic turbopump	22
Example of a hydrostatic thrust bearing for a refrigerant compressor	25
CONCLUSIONS	28
RECOMMENDATIONS	29
REFERENCES	31
FIGURES 4-24	33 - 46
APPENDIX A. FIRST-ORDER WALL SHEAR STRESS COEFFICIENTS	
APPENDIX B. ALGEBRAIC BULK-FLOW EQUATIONS ON THE THIN FILM LANDS OF A THRUST BEARING	

LIST OF TABLES

		PAGE
1	Hydrostatic thrust bearing for an advanced cryogenic fluid turbopump	22
2	Hydrostatic thrust bearing for R134a compressor application	25

LIST OF FIGURES

		page
1	Geometry of hydrostatic/hydrodynamic thrust bearing.	3
2	Description of bearing pad and tapered film thickness.	10
3	Staggered control volumes for integration of bulk-flow equations in polar coordinates (r,2).	16
4	Orifice diameter vs. recess pressure ratio for ALH thrust bearing. (Effects of fluid inertia at film lands and recess edges).	33
5	Fluid film force vs. recess pressure ratio for ALH thrust bearing.	33
6	Pressure distributions for LH2 thrust bearing. (a) at pocket diameter for varying pressure ratios, (b) pressure contours and (c) pressure surfaces for pratio=0.50.	34
7	a) Flow rate vs. recess pressure ratio for ALH thrust bearing (b) Flow rates through inner and outer radii vs. recess pressure ratio for ALH thrust bearing	35
8	Axial stiffness coefficient (K_{zz}) vs. recess pressure ratio for ALH thrust bearing.	36
9	Axial damping coefficient (C_{zz}) vs. recess pressure ratio for ALH thrust bearing.	36
10	Axial inertia coefficient (M_{zz}) vs. recess pressure ratio for ALH thrust bearing.	37
11	Drag torque vs. recess pressure ratio for ALH thrust bearing. (Effects of fluid inertia at film lands and recess edges).	37
12	Maximum and minimum flow Reynolds numbers vs. recess pressure ratio for ALH thrust bearing. (Effects of fluid inertia at film lands and recess edges).	38
13	Maximum fluid speed flow Reynolds numbers vs. recess pressure ratio for ALH thrust bearing.	39
14	Film clearance (C) versus thrust load (W_z) for refrigerant thrust bearing. (Effects of fluid inertia at film lands and recess edges).	40
15	Recess pressure ratio versus dimensionless thrust load ($\bar{W}_z$) for refrigerant thrust bearing.	40
16	(a) Dimensionless bearing mass flow rate versus thrust load ($\bar{W}_z$) for refrigerant thrust bearing. (b) Mass flow rates (dim.) through inner and outer radii vs. versus thrust load ($\bar{W}_z$) for refrigerant thrust bearing.	41
17	Dimensionless axial stiffness ($\bar{K}_{zz}$) coefficient vs. versus load ($\bar{W}_z$) for refrigerant thrust bearing.	42
18	Dimensionless axial damping ($\bar{C}_{zz}$) coefficient versus load ($\bar{W}z$) for refrigerant thrust bearing.	42
19	Dimensionless axial inertia ($\bar{M}_{zz}$) coefficient versus load ($\bar{W}_z$)for refrigerant thrust bearing.	43
20	Dynamic stiffness coefficient ($\bar{K}_{zzd}= \bar{K}_{zz} - \bar{M}_{zz}\Omega^2$) versus load ($\bar{W}_z$) for refrigerant thrust bearing.	43
21	Dimensionless drag torque ($\bar{T}_{o**}$) versus load ($\bar{W}_z$) for refrigerant thrust bearing.	44
22	Maximum Reynolds numbers versus recess pressure ratio for refrigerant thrust bearing.	44
23	Maximum and minimum film (dimensionless) pressures versus recess pressure ratio for refrigerant thrust bearing.	45
24	Film Pressures from full inertia model. (a) pressure at recess diameter for p_{ratio}=0.93, 0.58, 0.22, (b) pressure surface and contours for p_{ratio}=0.58.	46
B.1	Staggered control volumes for integration of bulk-flow equations in polar coordinates (r,θ).	B.2
B.2	P-control volume for integration of continuity equation and pressure correction equation.	B.3
B.3	U-control volume for integration of circumferential bulk-flow momentum equation.	B.4
B.4	V-control volume for integration of radial bulk-flow momentum equation	B.6
B.5	T-control volume for integration of energy transport (fluid temperature) equation.	B.8

ACKNOWLEDGEMENTS

Thanks to Dr. Robert Thom and Mr. Tim Jett from NASA MSFC for their support and interest on this work. I am indebted to Mr. Tom Haykin from Pratt & Whitney for his valuable help and insightful discussions in regard to the thrust bearings for the ALH turbopump. The important advice of Mr. Philip Pelfrey was also critical for the completion of the work. The interest of Mr. Richard LeClaire from the AF Research Laboratory is also acknowledged.

INTRODUCTION

The importance of hybrid (combination hydrostatic and hydrodynamic) journal and thrust bearings and damping seal bearings as radial support elements in cryogenic turbomachinery has steadily grown over the past few years. Advanced primary power cryogenic turbopumps are compact - low count part units, operate at very high shaft speeds, and require of externally pressurized fluid film bearings to support the expected large thrust and lateral radial loads (Pelfrey, 1995). Fluid film bearings enable smaller and lighter turbopumps through no bearing DN life limitation and no sub-critical rotor operation. These mechanical elements have durability, low friction and wear, accuracy of positioning, and large direct stiffness and damping force coefficients. These features enable the design (and operation) of unshrouded impellers with a significant increase in the turbopump mechanical efficiency.

The growth of an "all-fluid-film- bearing" technology for advanced and less costly (per launching cost) turbopumps demands the development of analytical models and design tools, the testing of components, and the implementation of the technology. San Andrés (1990-1996) has performed the thermohydrodynamic analysis and developed computer programs for prediction of the static and dynamic force response of radial fluid film bearings for cryogenic applications. The research addresses effectively the most important theoretical and practical issues related to the operation and dynamic performance of cryogenic fluid film bearings, i.e. namely, geometric configuration, operating conditions, flow turbulence, fluid inertia, fluid compressibility, thermal effects, and two-phase flow phenomena. The computational programs are not restricted in their application to cryogenic fluid film bearings and seals. The codes have been validated with experimental data from *process fluid* film bearings with mineral oils, water and air in regimes of operation ranging from laminar flow to turbulent flows, and including the transition zone to fully developed turbulence.

Further applications of compressible fluid thrust bearings in the Thermal Management System of the Space Station *Freedom* also motivate further the need for advanced models and computational tools. Current thrust bearing computational programs are based on the Reynolds lubrication of classical lubrication, lack a comprehensive thermohydrodynamic, do not include real fluid properties, and neglect fluid inertia (Coriolis and centrifugal) effects on the bearing film lands.

Pinkus and Lund (1981) study the effects of centrifugal inertia on the performance of hydrodynamic thrust bearings. Hashimoto (1989, 1990) extend the analysis to include fluid advection transport effects. These original references have been instrumental to the present development. Centrifugal forces, most important in the performance of parallel plate bearings and seals, lead to subambient pressures and may induce lubricant cavitation. Thus, large areas of the bearing surface could be denuded of fluid with a significant reduction in the bearing load capacity. Operation at high rotational speeds will also generate large circumferential fluid speeds with a tremendous impact on the inertial pressure drop at the edges of the bearing recesses.

A bulk-flow analysis for prediction of the static load performance and dynamic force coefficients of angled injection, orifice-compensated hydrostatic / hydrodynamic thrust bearings follows. The model accounts for the bulk-flow mass, momentum and thermal energy transport, includes flow turbulence and fluid inertia (advection and centrifugal) effects on film lands and recesses, and incorporates cryogenic fluid properties using a NIST data base (McCarty, 1986). The computer program predicts the flow rate, load capacity, power loss and axial dynamic force coefficients for rigid surface, tapered land hybrid thrust bearings. The static and dynamic forced performance of two hydrostatic bearing geometries of interest for advanced cryogenic turbomachinery and oil-free compressors are discussed in detail. Recommendations for further research close the present development.

ANALYSIS

Consider the turbulent flow of a fluid within the film lands of a hybrid (hydrostatic/hydrodynamic) thrust fluid film bearing. The bearing geometry and coordinate system are depicted in Figure 1. In the following, the bulk-flow equations of motion for the flow on the thin film lands are detailed along with a perturbation analysis for description of the equilibrium flow (zeroth-order) and perturbed flow (first-order) due to shaft small amplitude axial motions.

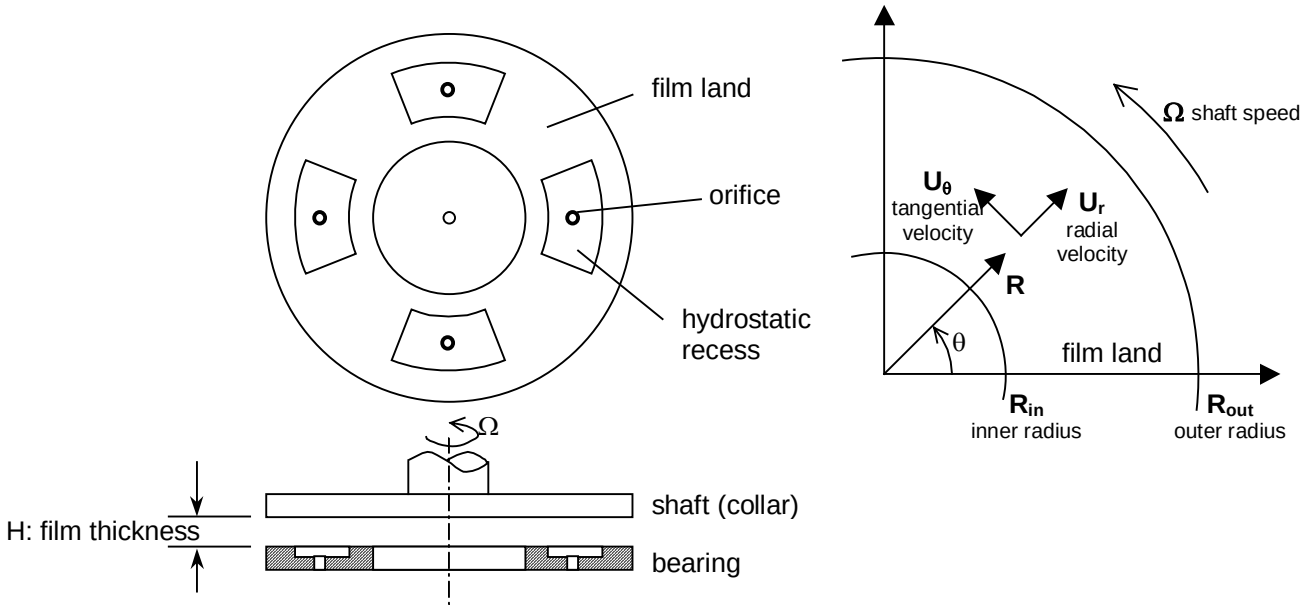

Figure 1. Geometry of a hydrostatic / hydrodynamic thrust bearing

Bulk-flow equations on the film lands of a hydrostatic thrust bearing

Flow turbulence, fluid inertia and compressibility effects are important on the thin film lands of a hydrostatic thrust bearing. The model assumes the fully developed turbulent bulk-flow of a fluid whose material properties depend on its local thermophysical state of pressure and temperature. The equations of mass, radial and circumferential momentum, and energy transport for the bulk-flow velocities, pressure and temperature on the bearing film lands are given as (San Andrés, 1994, 1995):

continuity:

$$\frac{\partial(\rho h)}{\partial t}+\frac{1}{R}\frac{\partial(R\rho HU_r)}{\partial R}+\frac{1}{R}\frac{\partial(\rho HU_\theta)}{\partial\theta}=0 \qquad (1.a)$$

radial momentum:

$$\frac{\partial(\rho HU_r)}{\partial t}+\frac{1}{R}\frac{\partial(R\rho HU_r^2)}{\partial R}+\frac{1}{R}\frac{\partial(\rho HU_rU_\theta)}{\partial\theta}-\frac{1}{R}\rho HU_\theta^2=-H\frac{\partial P}{\partial R}-\Delta\tau_{RZ} \qquad (1.b)$$

circumferential momentum:

$$\frac{\partial(\rho H U_\theta)}{\partial t}+\frac{1}{R}\frac{\partial(R\rho\ H U_r U_\theta)}{\partial R}+\frac{1}{R}\frac{\partial(\rho\ H U_\theta^2)}{\partial\theta}+\frac{1}{R}\rho H U_r U_\theta = -\frac{H}{R}\frac{\partial P}{\partial\theta}-\Delta\tau_{\theta Z} \quad (1.c)$$

energy transport:

$$C_p\left\{\frac{\partial(\rho HT)}{\partial t}+\frac{\partial(\rho HU_r T)}{\partial R}+\frac{1}{R}\frac{\partial(\rho\ HU_\theta T)}{\partial\theta}\right\}= \quad -Q_{BS}+$$

$$\beta_T\ H\ T\left(\frac{\partial P}{\partial t}+U_r\frac{\partial P}{\partial R}+\frac{1}{R}U_\theta\frac{\partial P}{\partial\theta}\right)+R\Omega\cdot\tau_{\theta R}\Big|^h+U_r\cdot\Delta\tau_{RZ}+U_\theta\cdot\Delta\tau_{\theta Z} \quad (1.d)$$

where $Q_{BS}=Q_B+Q_S=H_B(T-T_B)+H_S(T-T_S)$ is the convected heat flow through the bearing and runner (shaft) surfaces. *P* and *T* are the fluid pressure and temperature, and (U_r, U_2) are the bulk-flow velocities in the radial and circumferential directions, respectively. Refer to the Nomenclature for a description of all other variables.

The wall shear stress parameters are determined as local functions of turbulent friction factors, and which depend on the bearing and shaft surface conditions and the flow Reynolds numbers relative to the rotating shaft and stationary bearing surfaces (Hirs, 1973):

$$\Delta\tau_{RZ}=\frac{\mu}{H}\kappa_r U_r \qquad \Delta\tau_{\theta Z}=\frac{\mu}{H}\left(\kappa_\theta U_\theta-\frac{1}{2}\kappa_S\ \Omega R\right) \quad (2)$$

$$\tau_{\theta R}|^H=\frac{1}{2}\frac{H}{R}\frac{\partial P}{\partial\theta}+\frac{\mu}{4H}\{\kappa_\theta U_\theta-\kappa_S(U_\theta-\Omega R)\}$$

where the turbulent flow shear factors $(\kappa_r=\kappa_2,\ \kappa_S)$ are defined in terms of the friction factors (*f*) and Reynolds numbers *(Re)* relative to the stationary bearing (*B*) surface and the shaft (*S*) rotating surface. The functional forms are:

$$\kappa_r=\kappa_\theta=\frac{1}{2}(\kappa_B+\kappa_S);\quad \kappa_B=f_B\ Re_B\ ;\ \kappa_S=f_S\ Re_S \quad (3.a)$$

where

$$Re_B=\left(\frac{\rho H}{\mu}\right)\sqrt{U_R^2+U_\theta^2}\ ;\ Re_S=\left(\frac{\rho H}{\mu}\right)\sqrt{U_R^2+(U_\theta-\Omega R)^2} \quad (3.b)$$

The cryogenic liquid properties $(\Delta,:,C_p)$ are extracted from the Benedict-Web-Rubin equation of

state as given in the standard data base of McCarty (1986).

Bulk-flow equations at the recess of a hydrostatic thrust bearing

In a hydrostatic bearing, the fluid at pressure (P_s) and temperature (T_s) is supplied through orifice restrictors into the bearing pockets or recesses. The continuity equation at a hydrostatic recess establishes a balance among the mass flow through the feed orifice (M_R), the flow through the boundaries of the recess into the film lands (M_Γ), and the accumulation of fluid mass within the recess volume, $V_R=[A_R\,(H+H_R)+V_{supply}]$. The conservation of mass flows at a bearing recess is given as,

$$M_{R_i} = M_{\Gamma i} + \rho_{R_i}\frac{\partial V_{R_i}}{\partial t} + \rho_{R_i} V_{Ri}\left\{\beta_P \frac{\partial P}{\partial t} - \beta_T \frac{\partial T}{\partial t}\right\}_{R_i}, i = 1,...,N_{rec} \tag{4}$$

where $(P,T)_R$ are the averaged pressure and temperature within the recess, and $(\rho,\beta_P,\beta_T)_R$ are the fluid density, fluid compressibility coefficient and thermal expansion coefficient, respectively. Recall that the fluid material coefficients are defined as

$$\beta_P = +\left[\frac{1}{\rho}\frac{\partial \rho}{\partial P}\right]_T;\ \beta_T = -\left[\frac{1}{\rho}\frac{\partial \rho}{\partial T}\right]_P \tag{5}$$

The mass flow (M_R) through the orifice is given in terms of the pressure drop from the feed line at supply pressure (P_s) to the recess inlet pressure (P_R), i.e.

$$M_{Ri} = C_{d_i} A_{o_i}\left[2\rho_{Roi}\left(P_S - P_{R_i}\right)\right]^{1/2}_{i=1,...,N_{rec}} \tag{6}$$

where $A_o = \frac{\pi}{4} d_o^2$ is the orifice area and C_d is an empirical discharge (loss) coefficient. The mass flow rate leaving the i_{th}-recess through its boundary (Γ) and into the thin film lands is given as

$$M_{\Gamma i} = \oint_{\Gamma_i} \rho H \vec{U}\cdot\vec{\eta}\ d\Gamma_i \tag{7}$$

with the fluid velocities evaluated from the governing equations on the film lands.

A global flow energy balance is also accounted for at the bearing recesses. The simple model includes the mechanical energy dissipated by viscous shear, the heat-carry over (advection) from upstream conditions and the thermal mixing effects. The transport of thermal energy equation within a bearing recess is written as:

$$\left\langle C_p V_R \frac{\partial(\rho T)_R}{\partial t} = C_P M_R T_s - \oint_{\Gamma_R} C_p T\left(\rho H \vec{U}\right)\cdot\vec{\eta}\, d\Gamma + T_{oR}\Omega \right\rangle_{i=1,...,N_{rec}} \tag{8}$$

where T_{oR} is the shear viscous drag torque on the recess area.

The analysis also considers the circumferential bulk-flow and pressure rise within the hydrostatic recesses as a one-dimensional Rayleigh-step bearing. The simple model also includes the momentum transfer due to angled fluid injection against shaft direction. San Andrés and Childs (1997) provide full details on this analysis. The edge recess pressure $\left(P_{R_e}^-\right)$ just before the inlet to the film lands is given by the approximate relationship (San Andrés, 1995):

$$P_{Re}^- = P_R + \mu_R \frac{b_R}{2\left(H + H_R\right)^2}\left(\kappa_\theta U_\theta - \kappa_S \frac{\Omega R}{2}\right)_R \tag{9}$$

where b_R is the circumferential length of a hydrostatic recess[1].

High-speed thrust bearings can develop significant centrifugal flow effects. San Andrés (1997) presents a simple model for prediction of the radial pressure rise within the recess region due to the centrifugal fluid acceleration. The radial pressure within the recess is given by:

$$\left\langle P = P_R + P_{R_{dyn}}\left[\left(s^2 - 1\right)\left\{1 + \left(\frac{U_{r_R}}{s U_{\theta_R}}\right)^2\right\} - \frac{2\,\mu\; k_r\, U_{r_R} R}{\rho\left(H + H_R\right)^2 U_{\theta_R}^2} ln(s)\right]\right\rangle_{i=1,\ldots,N_{rec}} \tag{10}$$

where *($s=R/R_R$)*, and *($U_{r_R}, U_{\theta_R} = \alpha\,\Omega\, R_R$)* are the radial and circumferential bulk-flow velocities within the recess, and $P_{R_{dyn}} = \frac{1}{2}\rho\, U_{\theta_R}^2$ is the dynamic pressure head due to centrifugal fluid inertia. The expression above shows the variation of recess pressure due to the following effects:

a) viscous shear decreasing the pressure as the radius grows, i.e. towards the outer side of the bearing.
b) centrifugal forces due to fluid rotation which raise the pressure towards the outer radius of the recess, and
c) advection of fluid momentum in the radial direction that decreases the pressure as the radius within the recess grows.

The viscous and centrifugal fluid inertia effects on the generation of the recess pressure field, equations (9) and (10), are superimposed. This assumption is grounded on simplicity rather than on a thorough analysis of the complex flow field within the hydrostatic pockets.

The local acceleration of fluid from a deep recess into the thin film lands causes a sudden pressure drop. The pressure $\left(P_{R_e}^+\right)$at the entrance to the film lands is modeled from Bernoulli's equation as,

[1] Note that this length varies in the radial direction.

$$P_{R_e}^{-} = P_{R_e}^{+} + \frac{(1+\xi)}{2}\rho_e^{-}\left[1-\left(\frac{\rho_e^{-}}{\rho_e^{+}}\right)\left(\frac{H}{H+H_R}\right)^2\right]U_{r,\theta}^2 \tag{11}$$

where $\xi=\{\xi_i,\xi_o,\xi_{\theta u},\xi_{\theta d}\}$ are empirical entrance loss coefficients for the edges of a recess at its inner radius, outer radius, upstream and downstream circumferential directions, respectively. The sudden pressure drop is accounted for only if the fluid flow effectively enters the thin film lands.

Governing equations in dimensionless form

Let dimensionless coordinates and flow variables be defined as:

$$\begin{aligned} &r=\frac{R}{R_*};\ \tau=\omega_* t\ ;\ h=\frac{H}{C_*};\ u_r=\frac{U_r}{U_*};\ u_\theta=\frac{U_\theta}{U_*};\ \overline{P}=\frac{P-P_a}{P_s-P_a};\ \overline{T}=\frac{T}{T_*};\\ &\overline{\rho}=\frac{\rho}{\rho_*};\ \overline{\mu}=\frac{\mu}{\mu_*};\ \overline{C}_p=\frac{C_p}{C_{p^*}};\ \overline{\beta}_T=T_*\,\beta_T;\ \overline{H}_B=\frac{H_B}{H_{B^*}};\ \overline{H}_S=\frac{H_S}{H_{S^*}} \end{aligned} \tag{12.a}$$

where the (*) denotes characteristic values, and with $U_*=\frac{C_*^2\left(P_S-P_a\right)}{\mu_*\,R_*}$ as a characteristic pressure flow velocity. Dimensionless orifice and recess outflow mass flow rates, recess area and volume are defined as

$$\overline{M}_{R,\Gamma}=\frac{M_{R,\Gamma}}{\left(\rho_*\,U_*\,C_*\,R_*\right)};\qquad \overline{A}_R=\frac{A_R}{R_*^2};\quad \overline{V}_R=\frac{V_R}{R_*^2\,C_*} \tag{12.b}$$

The bulk-flow equations of motion on the **thin film lands** become in dimensionless form:

<u>continuity:</u>

$$\sigma\frac{\partial\left(\overline{\rho}\,h\right)}{\partial\tau}+\frac{1}{r}\frac{\partial\left(r\,\overline{\rho}\,hu_r\right)}{\partial r}+\frac{1}{r}\frac{\partial\left(\overline{\rho}\,hu_\theta\right)}{\partial\theta}=0 \tag{13.a}$$

<u>radial momentum:</u>

$$Re_{p^*}\left[\sigma\frac{\partial\left(\overline{\rho}\,hu_r\right)}{\partial\tau}+\frac{1}{r}\frac{\partial\left(r\,\overline{\rho}\,hu_r^2\right)}{\partial r}+\frac{1}{r}\frac{\partial\left(\overline{\rho}\,hu_r\,u_\theta\right)}{\partial\theta}-\frac{1}{r}\overline{\rho}\,hu_\theta^2\right]+\frac{\overline{\mu}}{h}\kappa_r\,u_r=-h\frac{\partial\overline{P}}{\partial r} \tag{13.b}$$

<u>circumferential momentum:</u>

$$Re_{p^*}\left[\sigma\frac{\partial\left(\overline{\rho}hu_\theta\right)}{\partial\tau}+\frac{1}{r}\frac{\partial\left(r\,\overline{\rho}hu_r\,u_\theta\right)}{\partial r}+\frac{1}{r}\frac{\partial\left(\overline{\rho}hu_\theta^2\right)}{\partial\theta}+\frac{1}{r}\overline{\rho}hu_r\,u_\theta\right]$$

$$+\frac{\overline{\mu}}{h}\left(\kappa_\theta\,u_\theta-\frac{1}{2}\kappa_S\,\Lambda r\right)=-\frac{h}{r}\frac{\partial\overline{P}}{\partial\theta} \tag{13.c}$$

energy transport:

$$\left(\frac{Re_{p^*}}{E_c}\right)\overline{C}_p\left\{\sigma\frac{\partial\left(\overline{\rho}h\overline{T}\right)}{\partial\tau}+\frac{\partial\left(\overline{\rho}hu_r\,\overline{T}\right)}{\partial r}+\frac{1}{r}\frac{\partial\left(\overline{\rho}hu_\theta\overline{T}\right)}{\partial\theta}\right\}+\left(\frac{Re_{p^*}}{E_c}\right)\left(\overline{H}_B+\overline{H}_S\right)\overline{T}=$$

$$\left(\frac{Re_{p^*}}{E_c}\right)\left(\overline{H}_B\overline{T}_B+\overline{H}_S\overline{T}_S\right)+\overline{\beta}_T h\overline{T}\left(\sigma\,\frac{\partial p}{\partial\tau}+u_r\,\frac{\partial\overline{P}}{\partial r}+\frac{1}{r}u_\theta\,\frac{\partial\overline{P}}{\partial\theta}\right) \tag{13.d}$$

$$+\frac{1}{2}\Lambda h\frac{\partial\overline{P}}{\partial\theta}+\frac{\overline{\mu}}{h}\left[\kappa_\theta\left(u_r^2+u_\theta^2+\frac{1}{2}\Lambda\,r\,u_\theta\right)\right]+\frac{\overline{\mu}}{h}\left[\kappa_S\Lambda\,r\left(\frac{1}{4}\Lambda\,r-u_\theta\right)\right]$$

where $\Lambda=\dfrac{\Omega R_*}{U_*}$ and $\sigma=\dfrac{\omega R_*}{U_*}$ are the shaft speed and frequency numbers. $Re_{P^*}=\left(\dfrac{\rho_* U_* C_*}{\mu_*}\right)\dfrac{C_*}{R_*}$ is a nominal Reynolds Number due to pressure flow, and $Re_\sigma=Re_{P^*}\,\sigma=\left(\dfrac{\rho_*\,\omega_* C_*^2}{\mu_*}\right)$ is a squeeze film Reynolds number. $E_c=\dfrac{U_*^2}{T_*\,C_{p^*}}$ is the Eckert heat transfer number, and $\left(\overline{H}_B\,,\overline{H}_S\right)$ are dimensionless convection heat transfer coefficients. The ratio $\left(\dfrac{Re_{p^*}}{E_c}\right)$ may be interpreted as the effect of heat convection relative to shear dissipation.

In dimensionless form, the mass conservation equation at the ***i_{th}*-hydrostatic recess** takes the form,

$$\overline{M}_{R_i}=\overline{M}_{\Gamma_i}+\sigma\,\overline{\rho}_{R_i}\left[\frac{\partial\overline{V}_{R_i}}{\partial\tau}+\overline{V}_{Ri}\left\{\overline{\beta}_P\,\frac{\partial\overline{P}}{\partial\tau}-\overline{\beta}_T\,\frac{\partial\overline{T}}{\partial\tau}\right\}_{R_i}\right];\ i=1,\ldots,N_{rec} \tag{14.a}$$

where $\overline{M}_{R_i}=\delta_{Ro_i}\left[\overline{\rho}_{Roi}\left(1-\overline{P}_{R_i}\right)\right]^{1/2}$, and $\overline{M}_{\Gamma i}=\oint_{B_i}\overline{\rho}\,h\,\vec{u}\cdot\vec{\eta}\,d\overline{\Gamma}_i$ (14.b)

with an orifice parameter defined as,

$$\delta_{Ro} = \frac{C_d \; A_o \left(2\,\rho_* \left[P_s - P_a\right]\right)^{1/2}}{\left(\rho_* \, U_* \, C_* \, R_*\right)} \tag{15}$$

The energy transport balance within a bearing hydrostatic recess is written as:

$$\left\langle \overline{C}_p \overline{V}_{R_i} \frac{\partial(\overline{\rho}\,\overline{T})_{R_i}}{\partial \tau} = \overline{C}_P \, \overline{M}_{R_i} \, \overline{T}_s - \oint_{\Gamma_R} \overline{C}_p \, \overline{T} \left(\overline{\rho}\, h \vec{u}\right).\vec{\eta} \, d\overline{\Gamma}_{R_i} + \left(\frac{E_c}{Re_{p_*}}\right) \overline{T}_{o\,R\,i} \Lambda \right\rangle_{i=1,\ldots,N_{rec}} \tag{16}$$

The circumferential and radial pressure rises within the i_{th}-hydrostatic recess are given in dimensionless form as:

$$\left\langle \overline{P}_{Re}^{-} = \overline{P}_R + \overline{\mu}_R \frac{\Theta_R r_R}{2\left(h + h_R\right)^2} \left(\kappa_\theta \, u_\theta - \kappa_S \frac{\Lambda r}{2} \right)_R \right\rangle_{i=1,\ldots,N_{rec}} \tag{17.a}$$

$$\left\langle \overline{P} = \overline{P}_R + \overline{P}_{R_{dyn}} \left[\left(s^2 - 1\right) \left\{ 1 + \left(\frac{u_{r_R}}{s\, u_{\theta_R}} \right)^2 \right\} - \frac{2\,\overline{\mu}\; k_r \, u_{r_R} r}{Re_{p*} \; \overline{\rho}\left(h + h_R\right)^2 U_{\theta_R}^2} ln(s) \right] \right\rangle_{i=1,\ldots,N_{rec}} \tag{17.b}$$

while the entrance pressures to the film lands bounding the i_{th}-hydrostatic recess are expressed as,

$$\left\langle \overline{P}_{R_e}^{-} = \overline{P}_{R_e}^{+} + \frac{\left(1+\xi\right)}{2} Re_{p*} \; \overline{\rho}_e^{-} \left[1 - \left(\frac{\overline{\rho}_e^{-}}{\overline{\rho}_e^{+}} \right) \left(\frac{h}{h + h_R} \right)^2 \right] u_{r,\theta}^2 \right\rangle_{i=1,\ldots,N_{rec}} \tag{18}$$

Film thickness expression and boundary conditions

The thrust hydrostatic/hydrodynamic bearing maybe composed of:

a) a single continuous (360E) pad with (N_{rec}) recesses distributed around the bearing area, or
b) a number of pads (N_{pad}) separated by radial grooves. Each pad may contain one or more recesses.

For a bearing pad of angular extent (1_{pad}) and with its leading edge at the angular location (1_{l_pad}), the film thickness including circumferential ($*2$) and radial ($*r$) slopes is given by (Pinkus and Lund, 1981):

$$h=\frac{H}{C}=1+\frac{1}{2}\delta\theta\left[1-K\,r\frac{\sin\left(\theta-\frac{\Theta_{pad}}{2}-\Theta_{l\_pad}\right)}{\sin\left(\frac{\Theta_{pad}}{2}\right)}\right]+\frac{1}{2}\delta r\left(\frac{\cos\left(\frac{\Theta_{pad}}{2}\right)}{K-1}\right)\left[1-K\,r\frac{\cos\left(\theta-\frac{\Theta_{pad}}{2}-\Theta_{l\_pad}\right)}{\cos\left(\frac{\Theta_{pad}}{2}\right)}\right] \tag{19}$$

where, referring to the geometry presented in Figure 2, $\delta\theta=\frac{(H_1-H_2)}{C}$; $\delta r=\frac{(H_3-H_4)}{C}$, are the slopes (taper) in the circumferential and radial directions, respectively.

$K^{-1}=\left[1-\frac{1}{2}\frac{(R_{out}-R_{in})}{R_{out}}\right]$ with $C=H_2$ as the film thickness at the midpoint of the pad trailing edge.

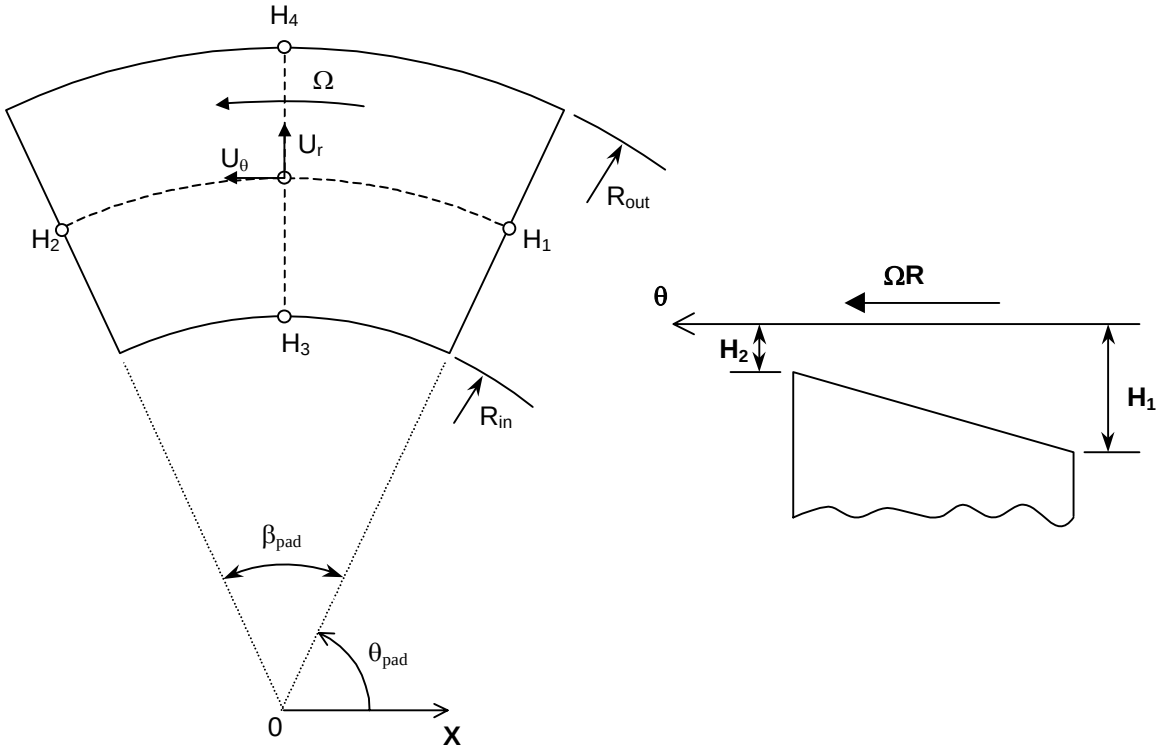

Figure 2. Description of a bearing pad and tapered film thickness.

The pressures at the inner and outer bearing radii are specified as,

$$\overline{P}(r_{in}) = \overline{P}_{D_{in}} \; ; \; \overline{P}(r_{out}) = \overline{P}_{D_{out}} \tag{20}$$

These pressures[2] are regarded as uniform or constant, and consequently, their variation under dynamic shaft motions is nil.

In a 360E bearing, the fluid pressure, temperature and velocities are singled valued in the circumferential direction, i.e.

$$\overline{P}, \overline{T}, u_r, u_\theta \left(r, \theta, t\right) = \overline{P}, \overline{T}, u_r, u_\theta \left(r, \theta + 2\pi, t\right) \tag{21}$$

while for a bearing pad, the pressures at the leading and trailing edges are given as a (known) function of the pressures $(\overline{P}_{D_{in}}, \overline{P}_{D_{out}})$ specified at the inner and outer radii, respectively. A ram-pressure effect due to fluid inertia at the leading edge of a bearing pad is also considered as per the analysis of San Andrés (1996).

Note that the momentum and energy equations on the film lands are of hyperbolic character, and consequently, no boundary conditions are required for the discharge temperature and fluid velocities at the bearing inner and outer radii. The balance of flow leaving the bearing recesses and entering the film lands provides the (inner) boundary conditions for the velocity fields on the thin film flow region, see equations (18).

Perturbation analysis of the flow field

Determination of the bearing dynamic force coefficients requires of a perturbation analysis of the flow field for infinitesimally small shaft axial motions about an equilibrium position. This elegant procedure renders sets of zeroth- and first-order flow equations for evaluation of the bearing static load capacity, shear torque, bearing and recess flow rates, and the dynamic force coefficients.

Consider small amplitude (Δz) axial motions of the thrust collar (shaft or runner) at frequency (Ω) about an equilibrium position denoted by (h_0). The film thickness is expressed in dimensionless form with $h_1 = \left(\frac{\Delta z}{C_*}\right)$ as,

$$h = h_0 + h_1 e^{i\tau} \quad ; \quad \frac{\partial h}{\partial \tau} = i\, h_1 e^{i\tau} \; ; \quad i = \sqrt{-1} \tag{22}$$

All the flow variables, pressure, temperatures and velocities are also expressed as the superposition of zeroth-order and first-order flow fields describing the equilibrium and the perturbed fields, respectively, i.e.,

$$\phi = \phi_0 + \phi_1 e^{i\tau} \; ; \qquad \phi = \left\{ u_r, u_\theta, \overline{P}, \overline{T}, \overline{\rho}, \overline{\mu}, \kappa_r, \kappa_\theta, \kappa_S, etc. \right\} \tag{23}$$

[2] The inner and outer radii pressures may be different depending on the closeness of the bearing to the discharge and suction zones of a centrifugal impeller in a cryogenic turbopump.

Substitution of these definitions into the thin film land equations (13) leads to the zeroth- and first-order governing equations for the fluid flow:

Zeroth-order bulk-flow equations on the film lands

continuity:

$$\frac{1}{r}\frac{\partial\left(r\,\overline{\rho}_0\,h_0\,u_{r0}\right)}{\partial r}+\frac{1}{r}\frac{\partial\left(\overline{\rho}_0\,h_0\,u_{\theta 0}\right)}{\partial\theta}=0 \tag{23.a}$$

radial momentum:

$$Re_{p^*}\frac{1}{r}\left[\frac{\partial\left(r\,\overline{\rho}_{\,0}\,h_0\,u_{r0}^2\right)}{\partial r}+\frac{\partial\left(\overline{\rho}_0\,h_0\,u_{r0}\,u_{\theta 0}\right)}{\partial\theta}-\overline{\rho}_0\,h_0\,u_{\theta 0}^2\right]+\frac{\overline{\mu}_0}{h_0}\kappa_{0r}\,u_{r0}=-h_0\frac{\partial\overline{P}_0}{\partial r} \tag{23.b}$$

circumferential momentum:

$$\begin{aligned}&Re_{p^*}\frac{1}{r}\left[\frac{\partial\left(r\,\overline{\rho}_0\,h_0\,u_{r0}\,u_{\theta 0}\right)}{\partial r}+\frac{\partial\left(\overline{\rho}_{\,0}\,h_0\,u_{\theta 0}^2\right)}{\partial\theta}+\overline{\rho}_0\,h_0\,u_{r_0}\,u_{\theta 0}\right]\\&+\frac{\overline{\mu}_0}{h_0}\left(\kappa_{\theta 0}\,u_{\theta 0}-\frac{1}{2}\kappa_{S0}\,\Lambda\,r\right)=-\frac{h_0}{r}\frac{\partial\overline{P}_0}{\partial\theta}\end{aligned} \tag{23.c}$$

energy transport:

$$\left(\frac{Re_{p^*}}{E_c}\right)\overline{C}_{p0}\left\{\frac{\partial\left(\overline{\rho}_{\,0}h_0\,u_{r0}\,\overline{T}_0\right)}{\partial r}+\frac{1}{r}\frac{\partial\left(\overline{\rho}_0\,h_0\,u_{\theta 0}\overline{T}_0\right)}{\partial\theta}\right\}+\left(\frac{Re_{p^*}}{E_c}\right)\left(\overline{H}_{B0}+\overline{H}_{S0}\right)\overline{T}_0=$$

$$\begin{aligned}&\left(\frac{Re_{p^*}}{E_c}\right)\left(\overline{H}_{B0}\overline{T}_{B0}+\overline{H}_{S0}\overline{T}_{S0}\right)+\overline{\beta}_{T0}h_0\,\overline{T}_0\left(u_{r_0}\,\frac{\partial\overline{P}_0}{\partial r}+\frac{1}{r}u_{\theta 0}\,\frac{\partial\overline{P}_0}{\partial\theta}\right)\\&+\frac{1}{2}\Lambda\,h_0\,\frac{\partial\overline{P}_0}{\partial\theta}+\frac{\overline{\mu}_0}{h_0}\left[\kappa_{\theta 0}\left(u_{r0}^2+u_{\theta 0}^2+\frac{1}{2}\Lambda\,r\,u_{\theta 0}\right)\right]+\frac{\overline{\mu}_0}{h_0}\left[\kappa_{S0}\Lambda\,r\left(\frac{1}{4}\Lambda\,r-u_{\theta 0}\right)\right]\end{aligned} \tag{23.d}$$

First-order bulk-flow equations on the film lands

with $h_1=1$ for pure axial shaft collar motions, i.e. without shaft angulations or dynamic misalignments:

continuity:

$$i\sigma\left(\overline{\rho}_0\, h_1 + \overline{\rho}_1\, h_0\right) +$$

$$\frac{1}{r}\frac{\partial\left\{r\left(\overline{\rho}_1\, h_0\, u_{r0} + \overline{\rho}_0\, h_1\, u_{r0} + \overline{\rho}_0\, h_0\, u_{r1}\right)\right\}}{\partial r} + \frac{1}{r}\frac{\partial\left\{\overline{\rho}_1\, h_0\, u_{\theta 0} + \overline{\rho}_0\, h_1\, u_{\theta 0} + \overline{\rho}_0\, h_0\, u_{\theta 1}\right\}}{\partial\theta} = 0 \qquad (24.a)$$

radial momentum:

$$-h\frac{\partial\overline{P}_1}{\partial r} = \gamma_{rh}h_1 + \gamma_{rr}u_{r1} + \gamma_{r\theta}u_{\theta 1} + \gamma_{rP}\overline{P}_1 + \gamma_{rT}\overline{T}_1 +$$

$$Re_{p^*}\frac{1}{r}\left[\frac{\partial\left(r\overline{\rho}_0 h_0 u_{r0} u_{r1}\right)}{\partial r} + \frac{\partial\left(\overline{\rho}_0 h_0\, u_{\theta 0}\, u_{r1}\right)}{\partial\theta} + \right. \qquad (24.b)$$

$$\left. \overline{\rho}_0\, h_0\; r\left(i\sigma + \frac{\partial u_{r0}}{\partial r}\right)u_{r1} + \overline{\rho}_0\, h_0\left(\frac{\partial u_{r0}}{\partial\theta} - 2u_{\theta 0}\right)u_{\theta 1}\right]$$

circumferential momentum:

$$-\frac{h}{r}\frac{\partial\overline{P}_1}{\partial\theta} = \gamma_{\theta h}h_1 + \gamma_{\theta r}u_{r1} + \gamma_{\theta\theta}u_{\theta 1} + \gamma_{\theta p}\overline{P}_1 + \gamma_{\theta T}\overline{T}_1 +$$

$$Re_{p^*}\frac{1}{r}\left[\frac{\partial\left(r\overline{\rho}_0 h_0 u_{r0} u_{\theta 1}\right)}{\partial r} + \frac{\partial\left(\overline{\rho}_0 h_0\, u_{\theta 1}\, u_{\theta 0}\right)}{\partial\theta} + \right. \qquad (24.c)$$

$$\left. \overline{\rho}_0\, h_0\left(i\sigma r + u_{r0} + \frac{\partial u_{\theta 0}}{\partial\theta}\right)u_{\theta 1} + \overline{\rho}_0\, h_0\left(r\frac{\partial u_{\theta 0}}{\partial r} + u_{\theta 0}\right)u_{r1}\right]$$

energy transport:

$$\left(\frac{Re_{p^*}}{E_c}\right)\overline{C}_{P0}\left\{\frac{\partial\left(\overline{\rho}_0\, h_0\, u_{r0}\,\overline{T}_1\right)}{\partial r} + \frac{1}{r}\frac{\partial\left(\overline{\rho}_0\, h_0\, u_{\theta 0}\,\overline{T}_1\right)}{\partial\theta}\right\} + \left(\gamma_{TT} + i\sigma\,\overline{\rho}_0\, h_0\,\frac{Re_{p^*}}{E_c}\overline{C}_{p0}\right)\overline{T}_1 +$$

$$\gamma_{Th}\,h_1 + \gamma_{Tr}\,u_{r1} + \gamma_{T\theta}\,u_{\theta 1} + \left(\gamma_{TP} - i\sigma\,\overline{\beta}_{T0}\,h_0\,\overline{T}_0\right)\cdot\overline{P}_1 - \frac{\Lambda}{2}h_{0`}\frac{\partial\overline{P}_1}{\partial\theta} \qquad (24.d)$$

$$= \overline{\beta}_{T0}\,h_0\,\overline{T}_0\left(u_{r0}\frac{\partial\overline{P}_1}{\partial r} + \frac{u_{\theta 0}}{r}\frac{\partial\overline{P}_1}{\partial\theta}\right)$$

The first-order wall shear stress coefficients ((‘s) are given in Appendix A.

Zeroth- and first-order flow equations at a bearing recess

Perturbation of the recess mass flow and energy transport equations proceeds with the following linear combination of equilibrium and dynamic fields,

$$\overline{M}_R = \overline{M}_{R0} + \overline{M}_{R1}\, e^{i\tau};\quad \overline{M}_\Gamma = \overline{M}_{\Gamma 0} + \overline{M}_{\Gamma 1}\, e^{i\tau};\overline{P}_R = \overline{P}_{R0} + \overline{P}_{R1}\, e^{i\tau};\overline{T}_R = \overline{T}_{R0} + \overline{T}_{R1}\, e^{i\tau} \tag{25}$$

to render the zeroth and first-order equations for mass flow conservation at each recess, i.e.,

$$\overline{M}_{R_0\, i} = \delta_{Ro_i}\left[\overline{\rho}_{Ro_{0_i}}\left(1-\overline{P}_{R_{0_i}}\right)\right]^{1/2} = \overline{M}_{\Gamma_{0_i}} = \oint_{\Gamma_i} \overline{\rho}_0\, h_0\, \vec{u}_0 \cdot \vec{\eta}\; d\overline{\Gamma}_i\,,\quad i=1,\ldots,N_{rec} \tag{26}$$

and

$$\left\langle -\; C^P_{R_i}\; \overline{P}_{R_{1i}} = \overline{M}_{\Gamma_{1_i}} + i\left(\sigma\, \overline{\rho}_{R_0}\, \overline{A}_{R_0}\right)_i\; h_{1i} + C^T_{R_i}\, \overline{T}_{R_{1_i}} \right\rangle_{i=1,\ldots,N_{rec}} \tag{27}$$

where

$$C^P_{R_i} = \left\{ \frac{\overline{M}_{R_0}}{2(1-\overline{P}_{R_0})}\left[1-\overline{\beta}_{P_R}(1-\overline{P}_{R_0})\right] + i\left(\sigma \overline{V}_{R_0}\, \overline{\beta}_{P_R}\, \overline{\rho}_{R_0}\right)\right\}_i \tag{28.a}$$

$$C^T_{R_i} = \overline{\beta}_{T_R}\left\{ \frac{\overline{M}_{R_0}}{2} - i\left(\sigma \overline{V}_{R_0}\, \overline{\rho}_{R_0}\right)\right\}_i;\quad i=1,\ldots,N_{rec}$$

and $\overline{M}_{\Gamma_1\, i} = \oint_{\Gamma_i}\left(\overline{\rho}_1\, h_0\, \vec{u}_0 + \overline{\rho}_0\, h_1\, \vec{u}_0 + \overline{\rho}_0\, h_0\, \vec{u}_1\right)\cdot\vec{\eta}\, d\overline{\Gamma}_i\,;\; i=1,..,N_{rec}$ (28.b)

are the first-order mass flow rates through the recess boundaries into the film lands.

The first-order energy transport equation at the recess and the pressure rise/drop equations at the recess edges are omitted for brevity.

Fluid film reaction force and axial force coefficients

The fluid film force *(F_Z)* reacting to an applied external load *(W_Z)* is given by integration of the hydrodynamic/hydrostatic pressure field on the bearing surface, i.e.,

$$F_Z = -W_Z = \oint_{A_B}(P - P_a)\, R\, dR\, d\theta \tag{29}$$

Substitution of the calculated zeroth- and first-order pressure fields into the equation above leads to the determination of the bearing load capacity and the dynamic stiffness *(K_{ZZ})*, damping *(C_{ZZ})*, and inertia *(M_{ZZ})* axial force coefficients, i.e.

$$F_Z = (P_s - P_a)\, A_B \oint_{\overline{A}_B} \overline{P}_0\, r\, dr\, d\theta \tag{30}$$

$$K_{ZZ} - \omega^2 M_{ZZ} + i\omega\, C_{ZZ} = \frac{1}{C}(P_s - P_a)\, A_B \oint_{\overline{A}_B} \overline{P}_1\, r\, dr\, d\theta \tag{31.a}$$

In general, bearings operating with incompressible fluids lead to force coefficients independent of the excitation frequency *(T)*. However, compressible fluids and bearings with recesses of large volume give rise to force coefficients that are complicated functions of the frequency *(T)*. In this case, the results from the model should be interpreted as frequency dependent impedance functions whose real and imaginary parts render dynamic stiffness and damping coefficients, respectively, i.e.,

$$K_{ZZ}(\omega) + i\,\omega\, C_{ZZ}(\omega) = \frac{1}{C}(P_s - P_a)\, A_B \oint_{\bar{A}_B} \bar{P}_1\, r\, dr\, d\theta \qquad (31.b)$$

San Andrés (1991) discusses the effects of recess volume – fluid compressibility on the dynamic force response of hydrostatic bearings operating with compressible fluids (such as LH_2) and provides criteria to avoid pneumatic hammer (loss of damping) instability. It is important to note that the notion of frequency dependent force coefficients does not imply these coefficients are nonlinear in terms of the dynamics of a rotor-bearing system, i.e. the force coefficients are not functions of the amplitude of motion[3].

The shear drag torque *(T_o)* on the rotating member is generated by the shear stresses acting on the runner surface, and given as

$$T_o = \oint_{A_B} \tau_{\theta R}\,|^H\; R^2\, dR\, d\theta = \left(\frac{\mu_* U_* R_*^3}{C}\right) \oint_{\bar{A}_B} \left\{ \frac{1}{2}\frac{h}{r}\frac{\partial \bar{P}}{\partial \theta} + \frac{\bar{\mu}}{4h}\left\{ \kappa_\theta\, u_\theta - \kappa_S\,(u_\theta - \Lambda r) \right\} \right\} r^2\, dr\, d\theta \quad (32)$$

Numerical method of solution of flow equations on the film lands

A control-volume finite difference scheme is implemented to solve the coupled, nonlinear PDEs of mass, momentum and energy transport governing the fluid flow in a hybrid/hydrostatic thrust bearing. The flow field is represented by a series of discrete nodal bulk-flow velocities, fluid pressures and temperatures on staggered grids (Patankar, 1980). An advantage of the staggered grid is that the potential unrealistic wavy pressure solutions arising from a single grid are avoided. Algebraic difference equations are obtained by integration of the governing equations on finite size control volumes and using the full advection *SIMPLEC* algorithm of Van Doormaal and Raithby (1984). The effectiveness of the numerical algorithm has been demonstrated on the turbulent bulk-flow analysis of cryogenic fluid film radial bearings and seals (San Andrés, 1990, Yang, 1992, Yang et al., 1994).

Let the dimensionless zeroth- and first-order bulk flow field variables $\{u_r, u_\theta, \bar{P}, \bar{T}\}_{0,1}$ be represented by the discrete fields $\{\mathrm{U}, \mathrm{V}, \bar{\mathrm{P}}, \bar{\mathrm{T}}\}$ and $\{\mathrm{U}_1, \mathrm{V}_1, \bar{\mathrm{P}}_1, \bar{\mathrm{T}}_1\}$, respectively. The continuity equation, circumferential and radial momentum transport equations, and the energy transport equation are integrated on the P-, U-, V-, T-control volumes depicted in Figure 3 to render sets of algebraic difference equations. Appendix B details the steps in the numerical procedure and includes all the equations derived and as implemented in the computer program.

[3] Of course, this last assertion is only valid for truly small amplitude motions about an equilibrium configuration.

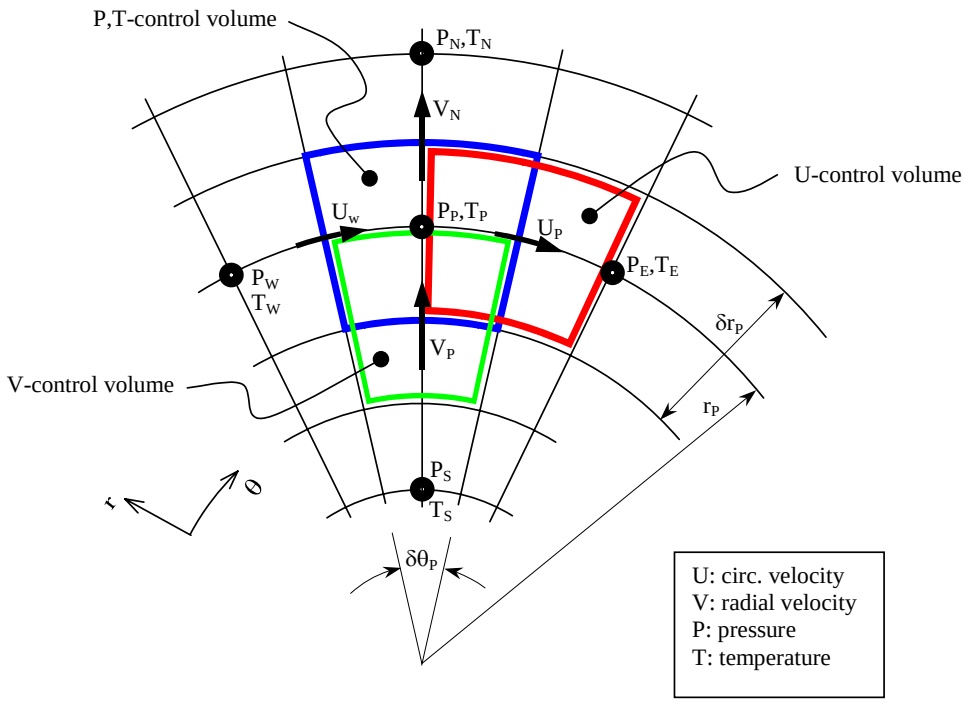

Figure 3. Staggered control volumes for integration of bulk-flow equations in polar coordinates (r,θ)

The governing difference equations on the bearing film lands are solved iteratively. An approximate solution for the flow field variables is used to initiate the calculations[4]. The velocity components $\{U^*, V^*\}$ are first calculated from the circumferential and radial momentum transport equation using an estimated pressure field $(\overline{P}^*)$. Next, the pressure correction equation based on the continuity equation provides a correction pressure $(\overline{p}')$ and velocity fields $\{u', v'\}$. Solution to the energy transport equation renders an estimate of the temperature field $(\overline{T})$. Updated pressure and velocity fields, $\{U = U^* + u';\ V = V^* + v';\ \overline{P} = \overline{P}^* + \overline{p}'\}$, are substituted again into the momentum equations resulting in (generally) more accurate velocity and pressure field solutions. The iterative procedure above is repeated until the sum of (absolute value) residuals of mass flow on the control volumes is below a prescribed tolerance value, typically 0.1% of the global mass flow rate on the whole domain of solution. See Appendix B for full details on the numerical algorithm.

The numerical method proceeds to balance the flow and momentum equations in the recesses of a hydrostatic bearing once a solution to the fluid flow equations on the film lands is obtained with appropriate boundary conditions. A Newton-Raphson algorithm provides

[4] The approximate analytical model corresponds to a highly idealized geometry and overly simplified flow condition. Nonetheless, the approximation provides a reasonable well posed field which allows rapid convergence to the final solution.

improved estimates of the recess pressures and velocity fields. The procedure is continued with the solution of the equations on the film lands until convergence is obtained in both film lands and recesses.

The iterative scheme for balance of flow at bearing recesses.

The recess pressures on each pocket of a hydrostatic bearing are updated after the computation of the flow field on the film lands. This procedure is performed iteratively until the set of mass flow rates into the film lands is balanced by the mass flow through each of the feed orifices in the recesses. Recall that the zeroth-order mass conservation at each recess is given by (the subscript "0" is omitted for brevity):

$$\left\langle \overline{M}_{\Gamma_i} = \overline{M}_{R_i} = \delta_{Ro_i} \left[\overline{\rho}_{R_i} \left(1 - \overline{P}_{R_i} \right) \right]^{1/2} \right\rangle_{i=1,....,N_{rec}} \tag{33}$$

At an intermediate step in the calculation of the flow field a set of "old" values of recess pressures and mass flows into the film lands is known, i.e. $\left\{ \overline{P}_{R_i} ; \overline{M}_{\Gamma_i} \right\}^{(old)}_{i=1,...,N_{rec}}$. A Newton-Raphson scheme allows the determination of "new" or improved recess pressures from the balance of the flow out from the orifices with the flows into the film lands. A first-order Taylor series expansion of the mass flow equation at each recess gives,

$$\overline{M}^{2\,(new)}_{R_i} = \delta^2_{Ro_i} \; \overline{\rho}^{(new)}_{R_i} \left(1 - \overline{P}^{(new)}_{R_i} \right) \; = \; \overline{M}^{2\,(old)}_{\Gamma_i} \; + \; \sum_{k}^{N_{rec}} \; \frac{\partial \, M^2_{B_i}}{\partial \, \overline{P}_{R_k}} \; \Delta \, \overline{P}_{R_k} \; ; \; _{i=1,...,N_{rec}} \tag{34}$$

where $\left(\Delta \overline{P}_R \; = \; \overline{P}^{(new)}_R \; - \; \overline{P}^{(old)}_R \right)_{k=1,..,N_{rec}}$, and define

$$S_{ik} = \frac{\partial \, \overline{M}^2_{\Gamma_i}}{\partial \, \overline{P}_{R_k}} \; \approx \; \frac{M^2_{\Gamma_i} \left(\overline{P}^{(old)}_{R_k} + \Delta \overline{\overline{P}}_{Rk} \right) \; - \; M^2_{\Gamma_i} \left(\overline{P}^{(old)}_{R_k} \right)}{\Delta \, \overline{\overline{P}}_{R_k}} \, , \; i,k \; = \; 1,2,...,N_{rec} \; , \tag{35}$$

as a set of mass flow (from recess to land) influence coefficients calculated with small (finite) pressure increments $\left(\Delta \overline{\overline{P}}_{R_k} \right)_{k=1,..,N_{rec}}$ around the (old) values of recess pressure. The fluid density is also a function of the flow pressure and temperature; and a Taylor series expansion leads to,

$$\begin{aligned} \overline{\rho}^{(new)}_{R_i} \; &\approx \; \overline{\rho}^{(old)}_{R_i} \; + \; \frac{\partial \, \overline{\rho}_{R_i}}{\partial \, \overline{P}_{R_i}} \; \Delta \, \overline{P}_{R_i} + \frac{\partial \, \overline{\rho}_{i\,i}}{\partial \, \overline{T}_{R_i}} \Delta \overline{T}_{R_i} \\ &= \; \overline{\rho}^{(old)}_{i\,i} \left(1 + \overline{\beta}^{(old)}_{P\,R_i} \Delta \, \overline{P}_{R_i} - \overline{\beta}^{(old)}_{T_{R_i} i} \Delta \overline{T}_{R_i} \right) , \quad i = 1,2,...,N_{rec} \end{aligned} \tag{36}$$

where $\left(\Delta\overline{T}_R = \overline{T}_R^{(new)} - \overline{T}_R^{(old)}\right)_{i=1,..N_{rec}}$ are variations in the recess temperatures. Substitution of the expansions into the recess mass flow rate equations for each recess leads to the following linear system of equations:

$$\sum_k^{N_{rec}} \left\{ S_{ik} + \delta_{ik}\, \delta_{Ro_k}^2 \left[1 - \overline{\beta}_{P_{R_k}} (1 - \overline{P}_{R_k}) - \beta_{T_{R_k}}\, \Delta\overline{T}_{R_k} \right] \right\}^{(old)} \overline{P}_{R_k}^{(new)}$$

$$= \left\{ -M_{\Gamma_i}^2 + \delta_{Ro_i}^2 \overline{\rho}_{Ri} \left[1 - \overline{\beta}_{P_{R_k}}\, \overline{P}_{R_i} (1 - \overline{P}_{R_i}) - \beta_{T_{R_i}}\, \Delta\overline{T}_{R_i} \right] + \sum_k^{N_{rec}} S_{ik}\, \overline{P}_{R_k} \right\}^{(old)}$$

i.e, (37)

$$\sum_k^{N_{rec}} \left\{ \overline{\overline{S}}_{ik} \right\}^{(old)} \overline{P}_{R_k}^{(new)} = \{rhs\}_i^{(old)};\ _{i=1,..,N_{rec}}$$

where $\delta_{ik} \begin{cases} 1, & \text{if } i = k \\ 0, & \text{otherwise} \end{cases}$, and from which updated (new) recess pressures are obtained in the iterative process until $\left\langle \overline{M}_{\Gamma_i} = \overline{M}_{R_i} = \delta_{Ro_i} \left[\overline{\rho}_{R_i} \left(1 - \overline{P}_{R_i} \right) \right]^{1/2} \right\rangle_{i=1,....,N_{rec}}$.

The numerical procedure of the iterative scheme is described briefly as:

a) Given initial recess pressures $\left(\overline{P}_{R_i}^{(old)}\right)_{i=1,2,...,N_{rec}}$, calculate the discrete flow fields [$U^*, V^*, \overline{P}^*, \overline{T}^*$, *and* $\left(\overline{T}_{R_i}^*\right)_{i=1,..,N_{rec}}$] on the thin film lands of the bearing.

b) Given a pressure increment to the k_{th} recess ($\Delta\overline{P}_{R_k}$) while all the other recess pressures remain unchanged, $\overline{P}_{R_i}^{(old)}$, $i \neq k$, recalculate the corresponding thin film land flow fields, and determine the mass flow influence coefficients, $[S_{ik}]_{i,j=1,...,N_{rec}}$, and $\left(\Delta\overline{T}_{R_i}^*\right)_{i=1,..,N_{rec}}$, for all recesses in the bearing or pad.

c) Reset the flow fields to the original ones, {U^*, V^*, $\overline{P}^*$, $\overline{T}^*$, and $\left(\overline{T}_{R_i}^*\right)_{i=1,..,N_{rec}}$}, calculated in step (a) and return to step (b) until all the recesses ($k = 1, 2,..,N_{rec}$) are covered.

d) Solve the system of equations (37) to update the recess pressures to $\left(\overline{P}_{R_i}^{(new)}\right)_{i=1,2,...,N_{rec}}$.

e) Return to step (a) and replace the initial recess pressures $\left(\overline{P}_{R_i}^{(old)}\right)_{i=1,2,...,N_{rec}}$ by the updated ones $\left(\overline{P}_{R_i}^{(new)}\right)_{i=1,2,...,N_{rec}}$. The iterative process continues until the difference of the orifice

mass flow, $\left(\overline{M}_{R_i}\right)_{i=1,2,...,N_{rec}}$, and flow rate into the film lands, $\left(\overline{M}_{B_i}\right)_{i=1,2,...,N_{rec}}$, for each recess is within a tolerable value (about 0.6%).

Numerical solution of the first-order bulk-flow equations

Once the solution to the zeroth-order equations on the bearing film lands and hydrostatic recesses has been obtained, the (perturbed) first-order flow fields $\{U_1, V_1, \overline{P}_1, \overline{T}_1\}$ are calculated for a given frequency (T).

The first-order equations are linear with coefficients fully determined by the zeroth-order flow field. The linearity of the equation enables a solution of the first-order flow field to be found by the component (superposition) method introduced by San Andrés (1990). In this procedure, the first-order flow field solution is given by the form,

$$\phi_1 = \phi_1^0 + \sum_i^{N_{rec}} \phi_1^i \ \overline{P}_{R_{1_i}} \ ; \ \phi_1 = \left[U, V, \overline{P}, \overline{T}\right]_1 \tag{38}$$

The first part in the components field, ϕ_1^0, is the solution to the non-homogeneous form of the first-order equations with the first-order recess pressures, $\left\{\overline{P}_{R_{1_i}}\right\}_{i=1,..,N_{rec}} = 0$. The second part corresponds to the addition of the component solutions $\left\{\phi_1^i\right\}_{i=1,...,N_{rec}}$ determined from solution to the homogeneous form of the first-order equations, i.e. with $\{h_1\} = 0$, and a complex unit value for each recess pressure, i.e., $\left\{\overline{P}_{R_{1_i}}\right\}_{i=1,..,N_{rec}} = (1+i)$.

The numerical scheme for the first-order equations on the film lands follows closely the one adopted for the zeroth-order equations. The same steps are followed for the solution of both the homogeneous and non-homogeneous first-order flow equations. Once all field components have been calculated, the first-order flow field is substituted into the first-order mass flow equations for each recess, equation (27), and a linear system of complex algebraic equations is obtained for calculation of the first-order recess pressures $\left\{\overline{P}_{R_{1_i}}\right\}_{i=1,..,N_{rec}}$, i.e:

$$\sum_k^{N_{rec}} \left(\overline{M}_{\Gamma_{1_i}}^k + C_{R_i}^T \overline{T}_{R_{1\,i}}^k + \delta_{ik} C_{R_k}^P\right) \overline{P}_{R_{1\,k}} = -\left(M_{\Gamma_{1_i}}^0 + i\sigma \overline{\rho}_{R_{0_i}} \overline{A}_{R_{0_i}} h_{1\,i} + C_{R\,i}^T \overline{T}_{R_{1i}}^0\right); \ i = 1,2,...,N_{rec}$$

or (39)

$$\sum_k^{N_{rec}} \left\{\overline{\overline{S}}_{1_{i,k}}\right\} \overline{P}_{R_{1\,k}} = \{rhs_1\}_i \ ; \ i = 1,2,...,N_{rec}$$

where

$$M_{\Gamma_{1_i}}^0 = \oint_{\Gamma_i} \left(\overline{\rho}_0 h_1 \vec{u}_0 + \overline{\rho}_0 h_0 \vec{u}_1^0 + \overline{\rho}_1^0 h_0 \vec{u}_0\right) \cdot \vec{n} \, d\overline{\Gamma}_i \ ,$$

$$M^{k}_{\Gamma_i} = \oint_{\Gamma_i} \left(\overline{\rho}_0 \, h_0 \, \vec{u}_1^{\,k} + \overline{\rho}_1^{k} \, h_0 \, \vec{u}_0 \right) \cdot \vec{n} \; d\overline{\Gamma}_i \,, \tag{40}$$

are the 0_{th}- and k_{th}-component first-order flow rates into the film lands at the boundary of the i_{th}-recess *(э$_i$)*.

The first-order mass conservation equation (39) at the recesses has the same form as the zeroth-order equation (27). However, the first-order equation represents a system of algebraic equations in the complex number domain, while the zeroth-order equation contains only real numbers and variables. Note that the set $\{ \overline{P}^{k}_{R_1} \}_{k=1,\ldots Nrec}$ in equation (39) needs to be evaluated only once since the first-order equations are linear and the superposition principle applies. On the other hand, $\{ \overline{P}^{(new)}_{R_k} \}_{k=1,\ldots Nrec}$ in the non-linear equations (27) are calculated iteratively until the recess flows balance the orifice flows.

Once the zeroth-order and first-order flow field are obtained, the fluid film forces and the dynamic force coefficients are calculated by integration of the zeroth- and first-order pressure field over the bearing surface, see equations (30) and (31).

THE COMPUTER PROGRAM HYDROTHRUST

The computer program developed in Fortran 90 is named *hydrothrust* and runs as a console application in a personal computer under the MS Windows operating system. The software package includes a windows based help file (*hthrust.help*) and several examples featuring the options and capabilities of the program.

hydrothrust calculates the static and dynamic force performance characteristics for the following bearing types:

1. hydrostatic / hydrodynamic thrust bearings with orifice compensation,
2. annular face seal with a pressure drop from inner diameter to outer diameter,
3. plain hydrodynamic thrust bearings.

hydrothrust includes the following thermal models:

- adiabatic surfaces, i.e. insulated shaft and bearing surfaces.
- isothermal shaft at specified temperature and insulated (adiabatic) bearing.
- isothermal bearing at specified temperature and insulated (adiabatic) shaft.
- isothermal shaft and bearing surfaces.
- isothermal shaft and radial heat flow through bearing (stator).
- adiabatic shaft and radial heat flow through bearing (stator).

hydrothrust provides numerical predictions of:

- bearing flow rate or seal leakage
- friction torque, power dissipation and temperature rise,
- load capacity if bearing minimum film clearance is given, or bearing film clearance if the external thrust load is given.
- axial stiffness, damping and inertia force coefficients evaluated at a specified excitation frequency.

with the following (single phase) fluids:
(1) parahydrogen, (2) oxygen, (3) nitrogen, (4) methane, (5) water, (6) oil, (7) air, (12) barotropic fluid.

A detailed description of the program operation and input/output calculation options is given in the help file *hthrust.help*.

NUMERICAL RESULTS AND DISCUSSION

The analysis and computational program are applicable to a wide range of thrust bearing applications including low speeds and pressures with viscous mineral oils (laminar flow bearings). However, the present development constitutes an advanced model for high speed hydrostatic / hydrodynamic thrust bearings for implementation in modern compact cryogenic liquid turbopumps. Unfortunately, experimental results for this application are not (yet) available in the open literature. Yet, undoubtedly, the interest on this novel fluid film bearing technology will render shortly important advances and actual applications.

Numerical predictions for thrust bearings operating in the laminar flow regime are given as examples in the *hydrothrust* software bundled package. Comparisons have been

performed with numerical results of Hashimoto (1989) and Zirkelback and San Andrés (1996) for hydrodynamic thrust bearings. These examples are omitted here for brevity.

Two high speed hydrostatic/hydrodynamic thrust bearing applications are hereby discussed at length. The first one corresponds to a thrust bearing geometry for the advanced liquid hydrogen (*ALH*) turbopump at nominal operating conditions, and the second example refers to a dual application hydrostatic thrust bearing for implementation in commercial (oil free) R134a compressors.

Example of a hydrostatic thrust bearing for a cryogenic turbopump

Table 1 lists the geometry and operating conditions of a liquid hydrogen, eight recess hydrostatic bearing for an advanced cryogenic turbopump. The pump design is uniquely compact with a low number of parts, and relies on hydrostatic radial and thrust fluid film bearings for accurate positioning of the rotor. Sound design and reliable operation of the fluid film bearing elements also allow for unshrouded impellers with a significant increase in the pump mechanical efficiency.

Table 1. Hydrostatic thrust bearing for an advanced cryogenic fluid turbopump

Geometry, N_{rec}=8	**SI dimensions**	**English dimensions**
Inner diameter, D_{in}	48.26 mm	1.9 inches
Outer diameter, D_{out}	99.06 mm	3.9 inches
Recess diameter, D_R	73.66 mm	2.9 inches
Recess radial length, L_R	10.16 mm	0.4 inches
Recess arc length, I_R	22 E	
Recess depth, H_R	0.254 mm	0.0100 inches
Film clearance	0.038 mm	0.0015 inches
Recess/Bearing area ratio	0.25	
Orifice diameter	Varies	
Empirical parameters		
Orifice discharge coefficient, C_d	0.90	
Entrance loss coefficients, $>_{ri}$, $>_{ro}$, $>_{2u}$, $>_{2d}$	0.00	
Inlet swirl coefficient, ∀	0.50	
Reynolds numbers	Re_c=162,740	Re_Φ=125.2

Operating conditions	**SI units**	**English units**
Speed (Σ)	17,802 r/s	170,000 rpm
Surface speed, ΣR_{in} , ΣR_{out}	442 – 908 m/s	1450 – 2979 ft/s
Fluid: liquid hydrogen,		
Supply temperature, T_s	45 EK	81 ER
Supply pressure, P_s	393 bar	5,700 psia
Exit pressure, P_a=P_{Din}=P_{Dout}	81.6 bar	2,200 psia
Fluid properties (supply/discharge)		
Density, [Δ_s, Δ_a]	(81.6, 65.3) kg/m^3	(5.09, 4.08) lb/ft^3
Viscosity, [$\therefore_s$, $\therefore_a$]	(0.0173, 0.0095) mPa.s	(0.0025, 0.0014) ∴Reyns
Sound speed (v_s,v_a)	(1793, 1299) m/s	(5882, 4262) ft/s
Fluid bulk modulus ($1/\exists_P$)	1,206 bar	17,495 psi

The operating conditions are extraordinary in terms of the high rotational speed (170 krpm) and available supply pressures. Note the large values of the shaft collar surface speeds *(ΣR),* ranging from 442 to 908 m/s for the inner and outer radii, respectively. Furthermore, the large magnitude of the circumferential flow Reynolds number, $Re_c=\Delta_s \Sigma R_{out} C/\nu_s$ = 162,740, denotes a highly turbulent flow regime with dominance of fluid inertia effects.

The analysis example considers a fixed clearance *(C)* equal to 38:m and intends to determine the orifice diameter necessary to achieve the maximum axial thrust stiffness. The numerical computations are carried out for increasing values of the recess pressure ratio, $p_{ratio}=(P_R-P_a)/(P_s-P_a)$, spanning from 0.1 to 0.9. The optimum stiffness condition is achieved at a particular recess pressure ratio, typically around 0.50 for laminar flow conditions. The example assumes that the turbopump has two thrust bearings acting in parallel, both balancing the thrust from the uneven axial pressure distribution in the impellers. The author has not been able to find (yet) definite information regarding the magnitude of the thrust loads at the operating point.

The numerical computations demonstrate the paramount effect of fluid inertia on the film lands of the thrust bearing as well as at the edges of the bearing recesses. The following figures depict computed results from three fluid flow models,

a) full inertia, includes fluid inertia (advection and centrifugal) at the film lands and recess edges,
b) recess edge inertia, accounts only for the sudden pressure drop at the recess boundaries as the fluid flow accelerates towards the film lands,
c) no fluid inertia, i.e., equivalent to the solution of the turbulent flow field within the film bearing lands as given by the classical Reynolds equation.

Figure 4 depicts the calculated orifice diameter versus the p_{ratio} for the thrust bearing, and determined from the balance of flows through the orifices and the flow into the film lands. The model without fluid inertia renders the largest orifice diameters denoting larger flow rates (see later Figures 7) since fluid inertia acts as an additional flow resistance, in particular at the recess edges. Figure 5 shows the axial fluid film bearing reaction force versus the recess pressure ratio. The full inertia model renders approximately 23% less load capacity than the inertialess fluid flow model. As the p_{ratio} increases (larger orifice diameter) the load also increases proportionately. However, larger loads are also accompanied by larger flow rates and lower stiffness coefficients, as will be seen shortly. The bearing reaction force is approximately equal to 31.6 kN (7,100 lbs) at a p_{ratio}=0.55 for the full inertia model. The significant load magnitude is (tough) 23% of the bearing specific load given by $(P_s-P_a)A_B$.

Figures 6 depict the calculated pressure profiles for the thrust bearing as determined from the full inertial model. The top figure shows the pressure at the radial location corresponding to the recess (and orifice) diameter versus the circumferential coordinate and for decreasing pressure ratios. The bottom figures display the pressure contours and pressure surface over the bearing for a p_{ratio}=0.50. Note the large (sharp) drops in fluid pressure at the recess edges (downstream and radial). Note that the pressures in the film

lands are quite low, thus indicating a dominance of fluid inertia effects. Furthermore, for the lowest pressure ratio, p_{ratio}=0.1, the minimum pressure within the film lands is lower than the discharge pressure (151.7 bar) due to the rapid fluid acceleration as it leaves the recess volumes.

Figures 7 display the bearing mass flow rate *(M)* versus the recess pressure ratio (increasing orifice diameters). The bearing flow rate increases steadily as the p_{ratio} increases, and the full fluid inertia model shows the smallest flow rates. Figure 7(b) depicts the mass flow rates leaving the bearing through the outer (M_{Rout}) and inner (M_{Rin}) radii, and where $M=M_{Rout}+M_{Rin}$. Note that the flow through the inner diameter is much lower than the flow through the outer radius. The difference is most obvious for the full inertia model due to the centrifugal fluid inertia effect.

Figures 9 through 11 show the stiffness (K_{ZZ}), damping (C_{ZZ}), and inertia (M_{ZZ}) axial force coefficients versus the recess pressure ratio for the three flow models. Note that only the full fluid inertia model renders inertia force coefficients. The stiffness coefficient (K_{ZZ}) has an optimum value for a p_{ratio}~0.5-0.65 depending on the fluid flow model. Note that the full inertia model provides the lowest stiffness magnitudes while the recess edge inertia model predicts an optimum force coefficient for a larger recess pressure ratio. The damping coefficient (C_{ZZ}) has a maximum for low values of p_{ratio}, and the full inertia flow model provides the largest damping values. The predicted results show similar trends as in radial hydrostatic bearings operating at high Reynolds numbers (San Andrés, 1990). The test measurements of Franchek, et al. (1995) for water lubricated hydrostatic radial bearings provide further evidence on the effects of fluid inertia reducing the stiffness and increasing the damping coefficients for high rotational speed operation.

Figure 10 shows the inertia force coefficient (M_{ZZ}) to decrease steadily as the recess pressure ratio increases with a minimum value at a p_{ratio}~0.5. The negative value is due to the fluid compressibility and indicates the frequency dependency of the force coefficients. Note that for shaft vibrations with a frequency synchronous with the rotational speed, i.e. at 2,833 Hz, the inertia force coefficient although small could introduce (in general) a marked de-stiffening effect.

Figure 11 depicts the drag torque versus the recess pressure ratio for the three fluid flow models. The largest torque and associated power loss are determined from the no fluid inertia model. Note that at a $p_{ratio}=0.50$, the power loss, i.e. the product of the torque times the rotational speed, is equal to 97.4 kW (130.5 Hp). This large magnitude is essentially due to the smallness of the film clearance (0.038 mm).

Figures 12 and 13 depict the maximum values of the bulk-flow Reynolds number and fluid speed within the fluid film flow region. Note that the full inertia model predicts the largest fluid speeds and Reynolds numbers, thus explaining the larger damping coefficients since the viscous dissipation of energy is the greatest. The most important finding is related to the very large bulk-flow fluid speeds (and Reynolds numbers) which are as large as the shaft speed at the bearing outer diameter (~900 m/s). Note that the

sonic speed for LH_2 is just 1,300 m/s at the bearing discharge planes, and consequently, the flow Mach numbers are around 0.50 for most pressure ratios.

Example of a hydrostatic thrust bearing for a refrigerant compressor

Table 2 presents the geometry and operating conditions of a six recess hydrostatic thrust bearings with R134a refrigerant for a commercial compressor application. The bearing design demonstrates the successful extension (dual use) of the cryogenic fluid film bearing technology to a process fluid film bearing application. In this example, the bearing geometry is specified including the orifice diameter[1]. The operating film clearances, between 12.7 μm to 101.6 μm, are calculated for a range of thrust loads at two operating speeds, 10 and 16 krpm, and pressure drops equal to 5.17 and 10.34 bars (75 and 150 psi), respectively. The predictions include the full fluid inertia and recess edge inertia models to demonstrate the paramount effect of land fluid inertia on the performance characteristics of the thrust bearing.

Table 2. Hydrostatic thrust bearing for R134a compressor application

Geometry, N_{rec}=6	**SI dimensions**	**English dimensions**
Inner diameter, D_{in}	89.13 mm	3.51 inches
Outer diameter, D_{out}	126.8 mm	4.99 inches
Recess diameter, D_R	108.6 mm	4.28 inches
Recess radial length, L_R	11.68 mm	0.46 inches
Recess arc length, I_R	24 E	
Recess depth, H_R	0.508 mm	0.0200 inches
Film clearance	0.012 – 0.101 mm	0.0005-0.004 inches
Recess/Bearing area ratio	0.25	
Orifice diameter	1.70 mm	0.067 inches
Empirical parameters		
Orifice discharge coefficient, C_d	0.80	
Entrance loss coefficients, $>_{ri}$, $>_{ro}$, $>_{2u}$, $>_{2d}$	0.0, 0.0, 0.0, -0.5	
Inlet swirl coefficient, ∀	0.50	
Operating conditions	**SI units**	**English units**
Speed	1047.2 – 1,675 r/s	10,000 – 16,000 rpm
Fluid: R134a refrigerant		
Supply temperature, T_s	311 EK	560 ER (100 EF)
Supply pressure, P_s	18.96 - 24.10 bar	275 - 350 psia
Exit pressure, P_a=P_{Din}=P_{Dout}	13.80 bar	200 psia
Saturation pressure,	9.63 bar	139 psia
Fluid properties		
Density, Δ_a	1210 kg/m^3	75.54 lb/ft^3
Viscosity, $:_a$	0.000198 Pa.s	0.0288 :Reyns
Fluid bulk modulus ($1/\exists_P$)	1,820 bar	26,667 psi

Figure 14 shows the equilibrium film clearance (C) versus the thrust load for the two operating conditions at 10 krpm and 16 krpm. The full fluid inertia model predicts smaller film thickness than the recess edge fluid inertia model, and the bearing with the

[1] The orifice discharge coefficient selected is based on prior experiences with hydrostatic radial bearings.

larger pressure drop, i.e. P_s=24.1 bars, shows a larger load capacity. In the following, the calculated results are presented in dimensionless form in an attempt to identify unique trends independent of the individual physical parameters.

Figure 15 depicts the equilibrium recess pressure ratio, $p_{ratio}=(P_R-P_a)/(P_s-P_a)$, versus the dimensionless load capacity, $\bar{W}z=Wz/A_B(P_s-P_a)$, for the two operating conditions. The recess pressure ratio increases as the thrust load increases (decreasing film clearance), and the fluid inertia model predicts larger recess pressures since it acts as an additional flow resistance at the film lands. Figure 16a shows the bearing mass flow rate ($\bar{M}$) to decrease steadily as the load $\bar{W}z$ increases (smaller film thickness and larger p_{ratio}). The mass flow rate is made dimensionless with respect to $N_{rec}C_dA_o(\frac{1}{2}\rho_s[P_s-P_a])^{1/2}$ representing the orifice flows from supply to ambient conditions. The full fluid inertia model shows slightly smaller flow rates. Figure 16(b) depicts the mass flow rates leaving the bearing through the outer and inner radii, with $\bar{M}=\bar{M}_{Rout}+\bar{M}_{Rin}$. The recess edge inertia model predicts an inner radius flow slightly smaller than the outer radius flow since the flow area is smaller. However, the full inertia model which includes the effects of centrifugal fluid inertia shows an outer radius flow much larger than the inner radius flow, in particular at low loads (small recess pressures and large clearance). In fact, the flow through the inner radius could be negative, i.e. the fluid is actually drag into the bearing due to a local suction (less than ambient) pressure at the film lands. The opposite effect occurs at the bearing outer diameter where more fluid is thrown away due to the large centrifugal inertia force. This force is proportional to the circumferential flow Reynolds number, $Re_c=(\rho R_{out}C/\mu)$, which increases as the clearance also increases (see Figure 22 later for the magnitudes of the maximum flow Reynolds numbers in the bearing). The calculated results thus indicate that operation with large clearances may cause fluid starvation (not a full fluid film) in certain regions of the film lands.

Figure 17 shows the dimensionless stiffness coefficient, $\bar{K}_{zz}=K_{zz}C/A_B(P_s-P_a)$, versus the dimensionless load $\bar{W}_z$ at the two operating speeds and pressure supplies. The magnitudes of the stiffness coefficients are similar for both flow models, although the optimum stiffness occurs at a lower load ($p_{ratio}\sim 0.6$) for the full inertia model. Figure 18 shows the dimensionless damping coefficient, $\bar{C}_{zz}=C_{zz}C\Omega/A_B(P_s-P_a)$ to increase steadily for small to moderate values of the dimensionless load $\bar{W}_z$. However, a large increase in damping is apparent at the largest loads and due essentially to the smallness of the film clearance (see Figure 14). Note that the full fluid inertia model predicts much larger damping coefficients for the entire range of thrust loads.

Figure 19 shows the dimensionless inertia coefficient, $\bar{M}_{zz}=M_{zz}C\Omega^2/A_B(P_s-P_a)$ decreases as the dimensionless load $\bar{W}_z$ increases. The physical values of the inertia coefficient range between 1.8 to 5.2 kg and could affect substantially the dynamic stiffness of the bearing, $K_{zzd}=K_{zz}-M_{zz}\Omega^2$ as shown in Figure 20. A comparison with the results given in Figure 17 shows that the bearing dynamic stiffness $\bar{K}_{zzd}$ is approximately 20% lower than the value predicted by the recess edge inertia model. This reduction is a direct effect of the fluid inertia (centrifugal and advection) at the film lands.

Figure 21 shows the torque $\bar{To}_{**}$ versus the dimensionless load $\bar{W}_z$. The drag torque is made dimensionless with respect to the reference formulae $T_{oT} = \left(1 + 0.024\left[0.4^2\ Re_c\right]^{0.65}\right)\frac{\mu_s \Omega\ A_B R_{out}^2}{C}$, obtained using the turbulent shear friction factor from Constantinescu (1962). Note that a reference drag torque value based on laminar flow conditions would render dimensionless torque values one to two orders of magnitude larger than the ones depicted in the figure. The calculated results show a similar drag torque for the two operating conditions and decreasing as the dimensionless load increases. Of course, the physical magnitude of the drag torque increases as the load magnitude increases since the film clearance is smaller.

The maximum bulk-flow Reynolds numbers and half the magnitude of the nominal circumferential Reynolds number, ½ $Re_c=(\rho R_{out}C/2\mu)$, are shown versus the recess pressure ratio in Figure 22. The bulk-flow Reynolds number is based on the maximum calculated fluid speed in the bearing flow region. Larger Reynolds numbers are a direct result of the shaft speed and larger film clearance as the recess pressure ratio decreases (smaller loads). The calculated results show that the flow-Reynolds numbers are very similar to the nominal circumferential Reynolds number, and thus demonstrate the dominance of hydrodynamic effects. The full inertia model predicts larger Reynolds numbers, i.e. larger fluid speeds, due to the centrifugal inertial effects and the rapid acceleration as the fluid leaves a recess a flows into the film lands.

Figure 23 shows the predicted maximum and minimum dimensionless pressures, $(P_{max,min}-P_a)/(P_s-P_a)$, in the bearing flow region versus the recess pressure ratio, $p_{ratio}=(P_R-P_a)/(P_s-P_a)$. The predicted results are of importance since they reveal significant features about the full fluid inertia model. First, the maximum film pressures are larger than the recess pressure at the orifice discharge plane since due to viscous and centrifugal fluid inertia effects there is a marked raise in the pressure at the recess corner facing the downstream edge and outer diameter. Note that for a $p_{ratio}=1$ the peak film pressure is 40% above the supply value. Second, the minimum film pressures are lower than the discharge pressure ($\bar{P}=0$) and the lowest magnitudes are achieved at the lowest recess pressure ratios. The appearance of the subambient film pressures, nearly 40% below discharge value (recall P_a=12.8 bar, 200 psia), is a direct result of the fluid (inertia) acceleration just downstream of a recess edge. The recess edge inertia model does not predict any subambient pressures.

At the operating conditions, the refrigerant saturation pressure is 9.63 bar (139 psia), and in dimensionless form $(P_{saturation}-P_a)/(P_s-P_a)$ equals –0.81 and –0.405 for the cases with pressure drops (P_s-P_a)=5.17 and 10.34 bars (75 and 150 psi) at 10 and 16 krpm, respectively. Thus, the thrust bearing operating at the largest rotational speed is likely to show fluid vaporization at the downstream edge of a hydrostatic recess! The current model is not (yet) able to model properly two-phase flow conditions, although Arauz and San Andrés (1998) have advanced some relevant analytical work. Nonetheless, the predicted results caution the operation of the thrust bearing under such stringent fluid flow conditions.

Figure 24 displays the calculated pressure fields from the full fluid inertia model. The top plots show the pressure field at the pocket (orifice) diameter versus the angular coordinate for various recess pressure ratios. Note the sharp pressure drops at the downstream side of a bearing recess. The bottom figure depicts the pressure surface and contours for a $p_{ratio}=0.5$ at 16 krpm. Note the pressure raise towards the downstream edge of a recess, and immediately the large pressure drop causing a rapid acceleration of the fluid.

As a note aside the present discussion, it is worth mentioning that the procedure implemented to render dimensionless bearing performance variables (load, flow, stiffness, etc) gives meaningful results which could aid to a fast (and reliable) design of turbulent flow hydrostatic/hydrodynamic thrust bearings.

CONCLUSIONS

A bulk-flow analysis and computer program for prediction of the static load performance and dynamic force coefficients of angled injection, orifice-compensated hydrostatic / hydrodynamic thrust bearings have been completed. Advanced cryogenic fluid turbopumps are very compact, operate at extremely high shaft speeds, and require of hybrid (hydrostatic / hydrodynamic) radial and thrust fluid film bearings for accurate rotor positioning. Sound design and reliable operation of the fluid film bearing elements also allows for unshrouded impellers with a significant increase in the turbopump mechanical efficiency.

The analysis accounts for the bulk-flow mass, momentum and thermal energy transport, includes flow turbulence and fluid inertia (advection and centrifugal) effects on film lands and recesses, and incorporates cryogenic fluid properties using a NIST data base. The computer program predicts the flow rate, load capacity, power loss and axial dynamic force coefficients for rigid surface, tapered land hybrid thrust bearings.

Two high-speed hydrostatic/hydrodynamic thrust bearing applications are analyzed. The first one corresponds to a thrust bearing geometry for the advanced liquid hydrogen (*ALH*) turbopump at nominal operating conditions, and the second example refers to a dual application hydrostatic thrust bearing for implementation in commercial (oil free) R134a compressors.

The computed predictions reveal that the ALH bearing load capacity and flow rate increase with the recess pressure (i.e. increasing orifice diameters) at the nominal operating condition. The bearing axial stiffness has a maximum for a recess pressure ratio ~0.55, while the axial damping coefficient decreases as the recess pressure ratio increases. The computer results from three flow models are compared. These models are a) inertialess, b) fluid inertia at recess edges only, and c) full fluid inertia at both recess edges and film lands. The full inertia model predicts the lowest flow rate, axial load capacity and stiffness coefficient, yet it renders the largest damping and inertia force coefficients. Some fluid compressibility effects are apparent in the application. The most important findings are related to the reduction of the outflow through the inner radius and the appearance of subambient pressures on the bearing film lands.

The performance of the refrigerant hybrid thrust bearing is evaluated at two operating speeds and pressure drops. The computed results are presented in dimensionless form to evidence consistent trends in the bearing performance characteristics. As the applied axial load increases, the bearing film thickness and flow rate decrease while the recess pressures increase. The axial stiffness coefficient shows a maximum for a certain intermediate load (recess pressure ratio) while the damping coefficient steadily increases. The computed results evidence the paramount of centrifugal fluid inertia at low recess pressures (i.e. low loads), and where there is actually an inflow through the bearing inner diameter along with subambient pressures just downstream of the bearing recess edges. These results are solely due to centrifugal fluid inertia and advection transport effects.

RECOMMENDATIONS

Further research is recommended to extend the analysis and continue the software development to include bearing geometries and operating conditions more representative of actual practice. In addition, the enhanced computer program should aim to satisfy the needs of commercial turbomachinery applications and to render a design tool of a broad engineering use. The flow model is currently restricted to axial shaft (collar) motions without angular misalignment. Thus, the analysis of the bulk-flow for shaft dynamic tilts in two planes is of importance to determine restoring torques and moment force coefficients.

Many hydrodynamic thrust bearings are composed of rigid pads with machined tapered lands. However, this low-cost bearing configuration can only be optimized for a narrow range of operating load and (low) speed conditions. High performance turbomachinery requires of tilting pad hydrodynamic thrust bearings able to adapt and configure to wide ranges of loads and speed conditions. In these bearings the pads rotate about spherical pivots to form the (wedge) hydrodynamic film able to support an axial load and without the need of a machined tapered surface. Some particular tilting pad thrust bearings are also supported on complex structural (springs) elements allowing the control of axial angular rotor misalignments. The major disadvantages of tilting pad bearings are their cost, complexity in manufacturing and stack up of tolerances on assembly. Furthermore, conventional tilting pad bearings are not easily modified to allow for a hydrostatic feed and external pressurization.

Submerged water pumps integrate a particular type of hydrodynamic thrust bearing where each sector pad is attached to a bearing support with a structural (elastic) radial web designed to provide a low stiffness restraint to pad angular motions, thus forming the hydrodynamic film wedge which generates the load support. Furthermore, the flexural webs also offer a feasible path for a hydrostatic fluid feeding port, thus allowing for an increased bearing load capacity and immediate application in a cryogenic fluid environment. The structural pad supports could also be engineered for the bearing to control dynamic angular rotor misalignments.

The fluid mechanics of highly compressible fluid media operating at near sonic conditions and with two-phase flow generation and transition from liquid to gaseous

states are also regarded as important in the near future. The analyses of thrust foil bearings and spiral grooved thrust bearings are also noted as important for future work.

REFERENCES

Arauz, G., and L. San Andrés, 1998, “Analysis of Two Phase Flow in Cryogenic Damper Seals, I: Theoretical Model, ” *ASME Journal of Tribology*, Vol. 120, pp. 221-227. (ASME Paper 97-Trib-12).

Constantinescu, V.N., 1962, “Analysis of Bearings Operating in the Turbulent Flow Regime,” *ASME Journal of Lubrication Technology*, Vol. 82, pp. 139-151.

Franchek, N., D. Childs, and L. San Andrés, 1995, "Theoretical and Experimental Comparisons for Rotordynamic Coefficients of a High-Speed, High-Pressure, Orifice-Compensated Hybrid Bearings," ASME *Journal of Tribology*, Vol. 117, 2, pp. 285-290.

Hashimoto, H., 1989, “The Effects of Fluid Inertia Forces on the Static Characteristics of Sector-Shaped, High Speed Thrust Bearings in Turbulent Flow Regime,” ASME *Journal of Tribology*, Vol. 111, pp. 406-411.

Hashimoto, H., 1990, “Performance Characteristic Analysis of Sector-Shaped Pad Thrust Bearings in Turbulent Inertial Flow Regime Under Three Types of Lubrication Conditions, ASME *Journal of Tribology*, Vol.112, pp. 477-485.

Hirs, G.G., 1973, “A Bulk-Flow Theory for Turbulence in Lubricant Films,” ASME Journal of Lubrication Technology, Vol. 95, pp. 137-146.

McCarty, R.D., NBS Standard Reference Data Base 12, 1986, “Thermophysical Properties of Fluids, MIPROPS86,” National Bureau of Standards, Colorado.

Patankar, S. V., 1980, Numerical Heat Transfer And Fluid Flow, Hemisphere Publishing Corporation, McGraw-Hill.

Pelfrey, P., 1995, *Seal Flow Code Development Workshop*, NASA Lewis Research Center, Cleveland, OH, June.

Pinkus, O., and J.K. Lund, 1981, “Centrifugal Effects in Thrust Bearings Under Laminar Conditions, “ ASME Journal of Lubrication Technology, Vol. 103, pp. 126-136.

San Andrés, L., 1990, "Turbulent Hybrid Bearings with Fluid Inertia Effects", ASME *Journal of Tribology*, Vol. 112, pp. 699-707.

San Andrés, L., 1991, "Fluid Compressibility Effects on the Dynamic Response of Hydrostatic Journal Bearings," ***WEAR***, Vol. 146, pp. 269-283.

San Andrés, L., 1994, "Dynamic Force Response of Spherical Hydrostatic Journal Bearings for Cryogenic Applications", STLE *Tribology Transactions*, Vol. 37, 3, pp. 463-470.

San Andrés, L., 1995, “Thermohydrodynamic Analysis of Fluid Film Bearings for Cryogenic Applications,” *AIAA Journal of Propulsion and Power*, Vol. 11, No. 5, pp. 964-972.

San Andrés, L., 1996, “Turbulent Flow, Flexure-Pivot Hybrid Bearings for Cryogenic Applications,” *ASME Journal of Tribology,* Vol. 118, pp. 190-200.

San Andrés, L., 1997, “Analysis of Pressure due to Centrifugal Flow Effects in a Thrust Bearing,” Monthly Progress Report to NASA Marshall SFC, November.

San Andrés, L., and D. Childs, 1997, "Angled Injection - Hydrostatic Bearings, Analysis and Comparison to Test Results," ASME *Journal of Tribology,* Vol. 119, 1, pp. 179-187, (ASME Paper 96-TRIB-10).

Van Doormaal, J. P., and Raithby, G. D., 1984, “Enhancements of the SIMPLE Method for Predicting Incompressible Fluid Flows,” Numerical Heat Transfer, Vol. 7, pp. 147-163.

Yang, Z., 1992, “Thermohydrodynamic Analysis of Product-Lubricated Hydrostatic Bearings in Turbulent Regime,” Ph.D. Dissertation, December.

Yang, Z., San Andrés, L., and Childs, D. W., 1994, “Dynamic Forces Performance of Annular Gas Seals at Off-Center Conditions,” STLE *Tribology Transactions*, Vol. 37, 1, pp. 33-44.

Zirkelback, N., and L. San Andrés, 1996, "Simplified Analysis of Hydrodynamic Thrust Bearings ", Report # TRC-B&C-4-96, Texas A&M University, May.

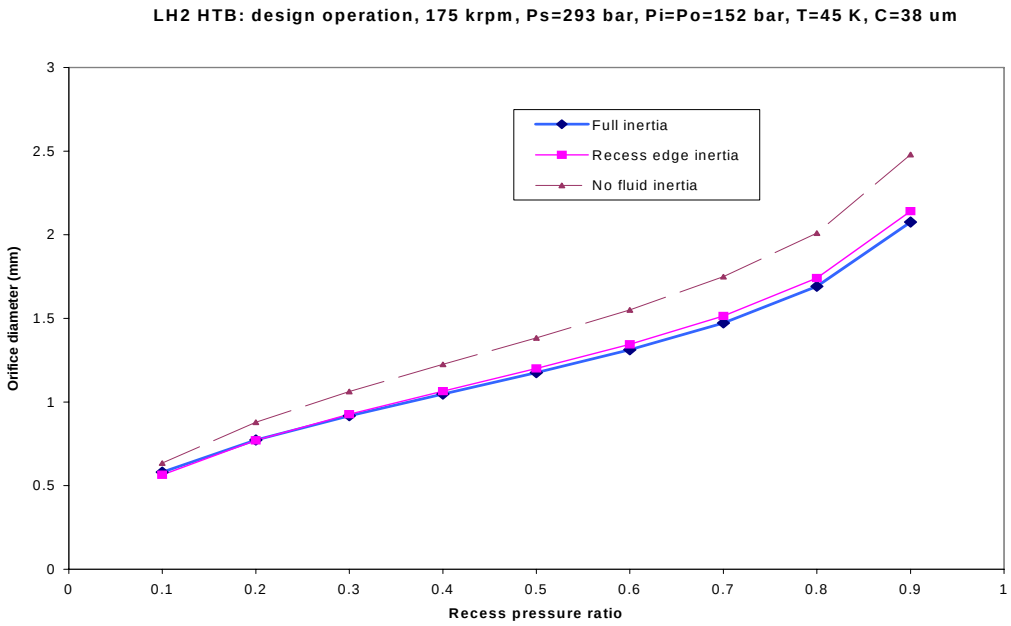

Figure 4. Orifice diameter vs. recess pressure ratio for ALH thrust bearing.
(Effects of fluid inertia at film lands and recess edges)

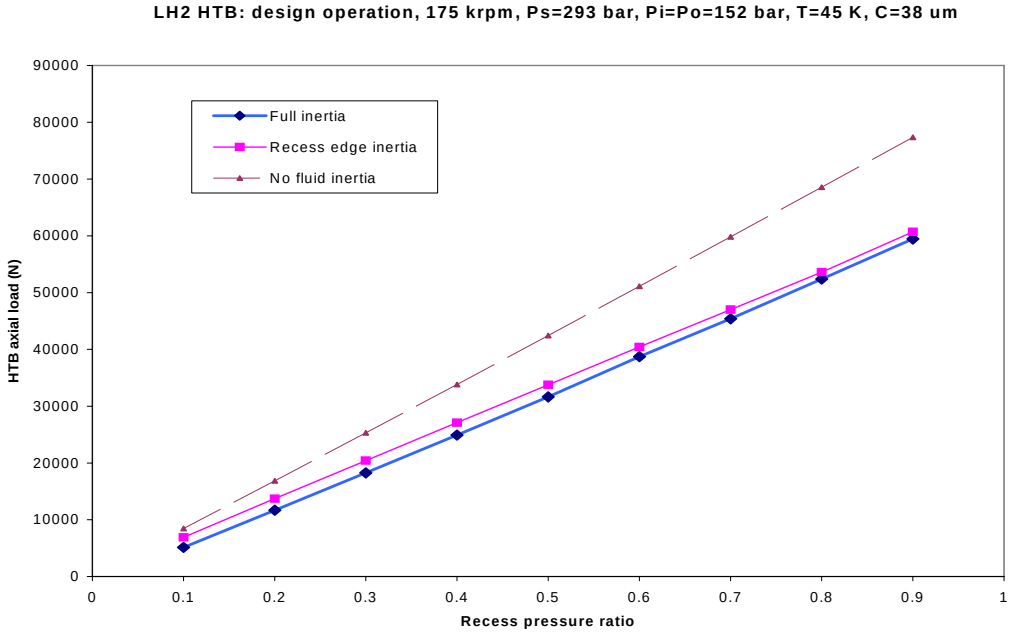

Figure 5. Fluid film force vs. recess pressure ratio for ALH thrust bearing.
(Effects of fluid inertia at film lands and recess edges)

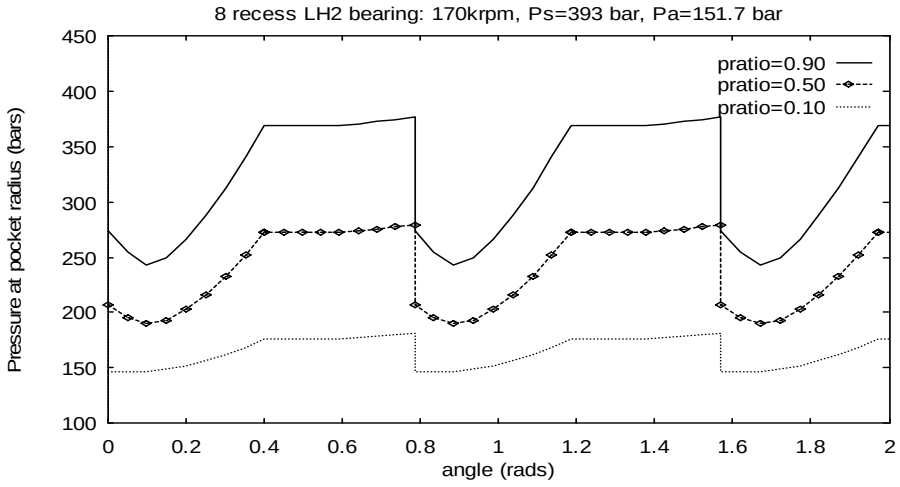

(a)

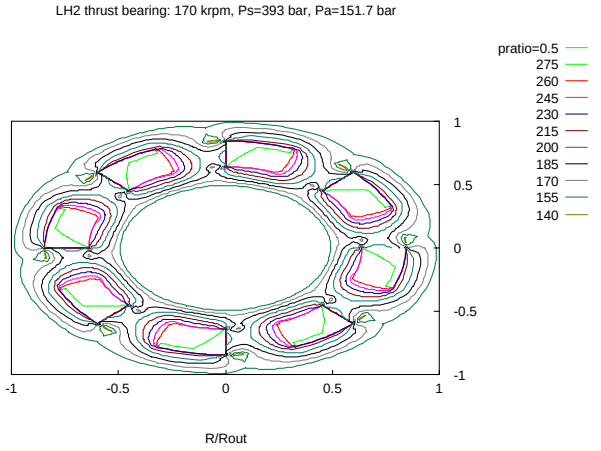

(b)

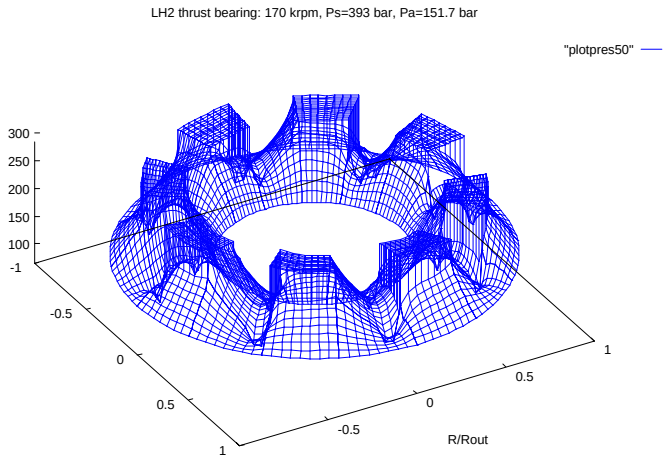

(c)

Figure 6. Pressure distributions for LH2 thrust bearing. (a) at pocket diameter for varying pressure ratios, (b) pressure contours and (c) pressure surfaces for p_{ratio}=0.50

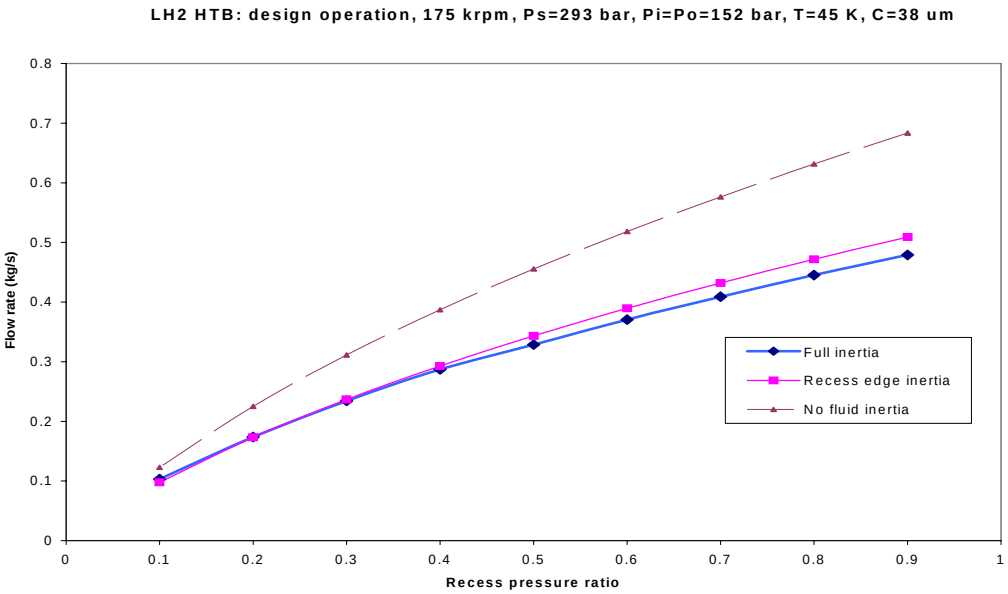

Figure 7(a). Flow rate vs. recess pressure ratio for ALH thrust bearing
(Effects of fluid inertia at film lands and recess edges)

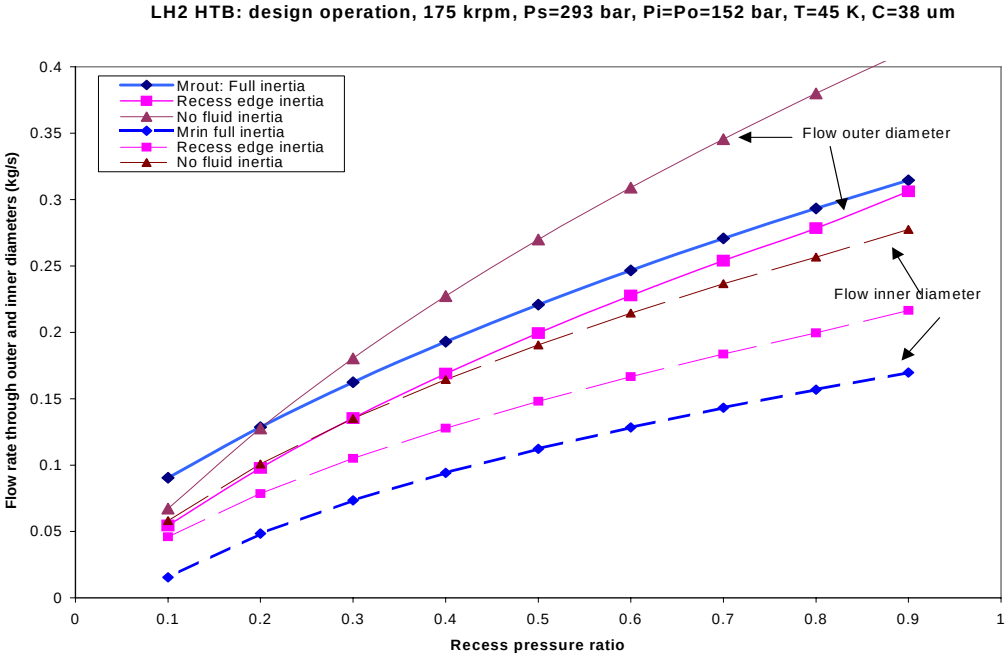

Figure 7(b). Flow rates through inner and outer radii vs. recess pressure ratio for ALH thrust bearing. (Effects of fluid inertia at film lands and recess edges)

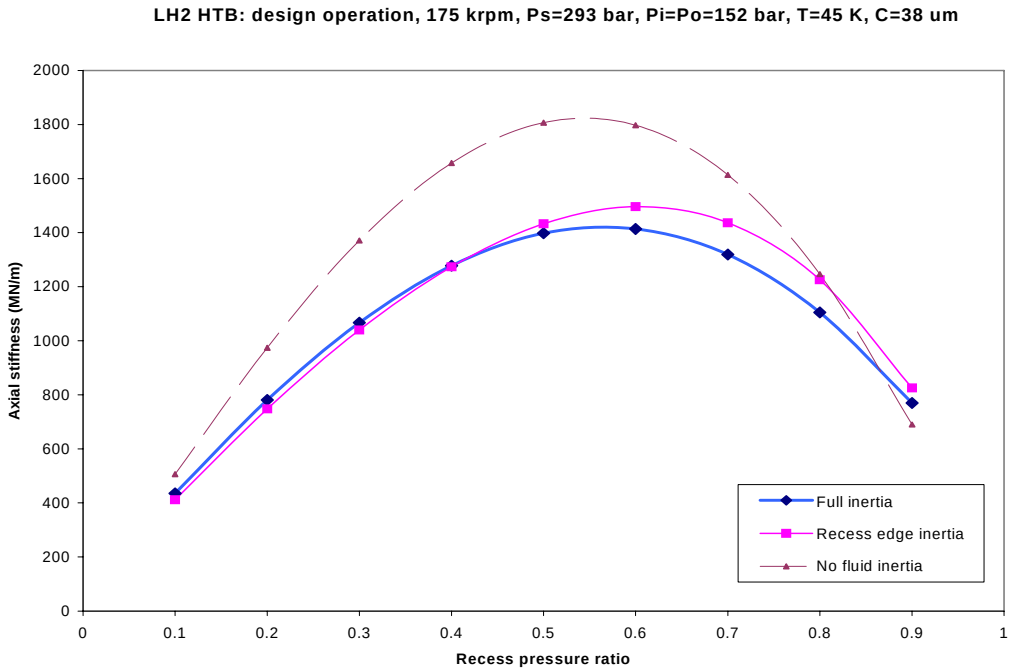

Figure 8. Axial stiffness coefficient (K_{zz}) vs. recess pressure ratio for ALH thrust bearing
(Effects of fluid inertia at film lands and recess edges)

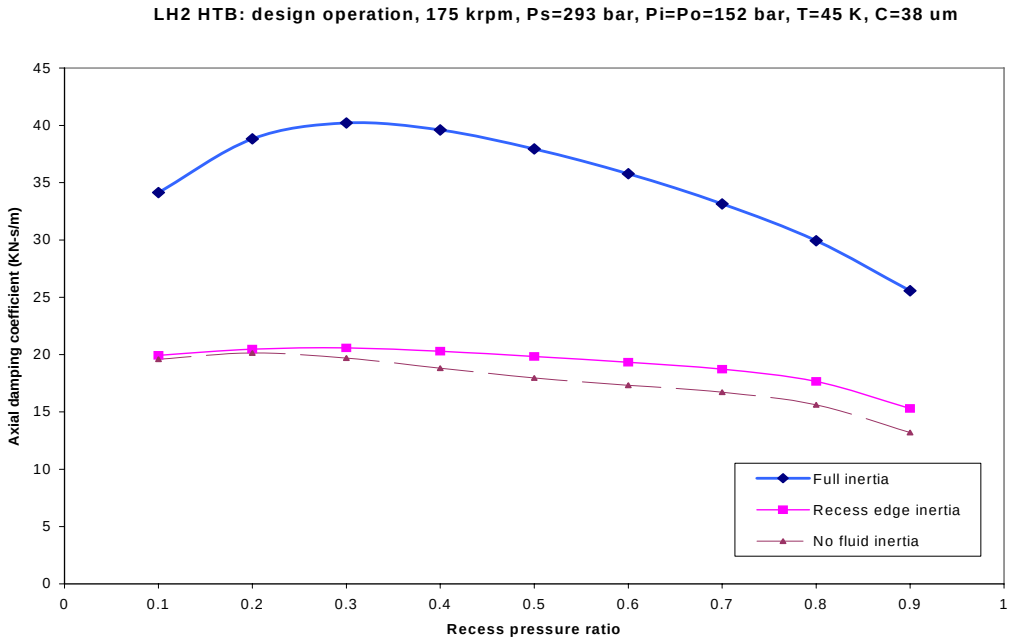

Figure 9. Axial damping coefficient (C_{zz}) vs. recess pressure ratio for ALH thrust bearing.

.

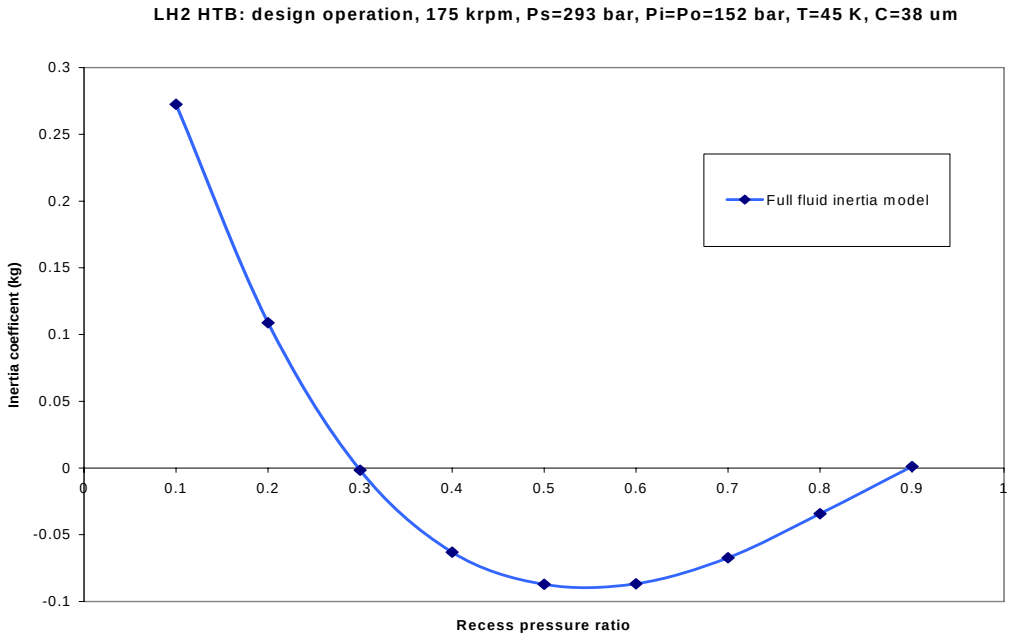

(Effects of fluid inertia at film lands and recess edges)

Figure 10. Axial inertia coefficient (M_{zz}) vs. recess pressure ratio for ALH thrust bearing

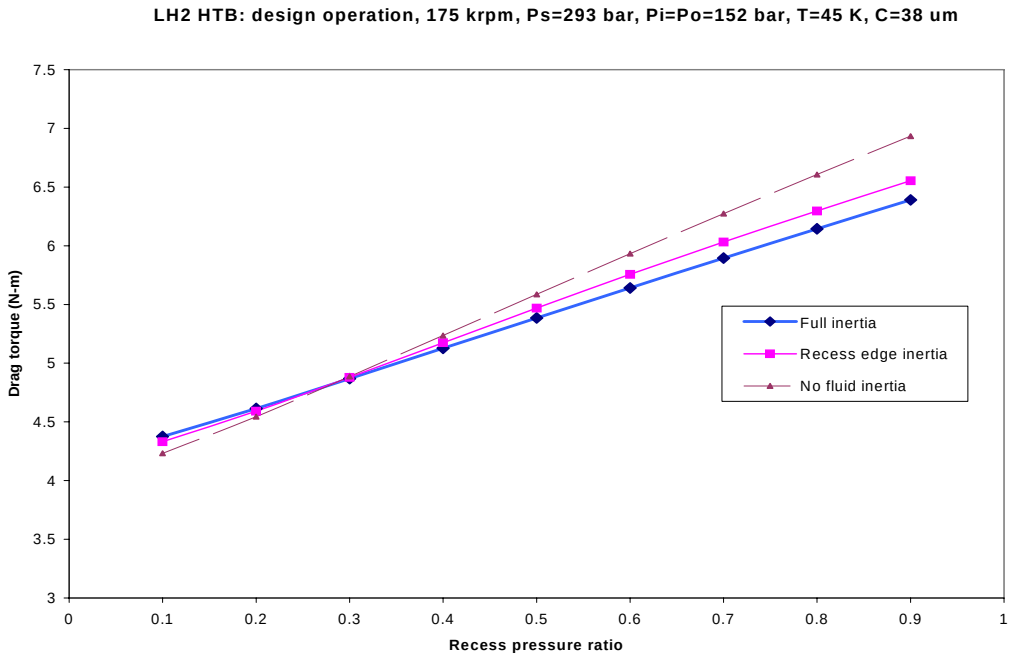

Figure 11. Drag torque vs. recess pressure ratio for ALH thrust bearing.
(Effects of fluid inertia at film lands and recess edges)

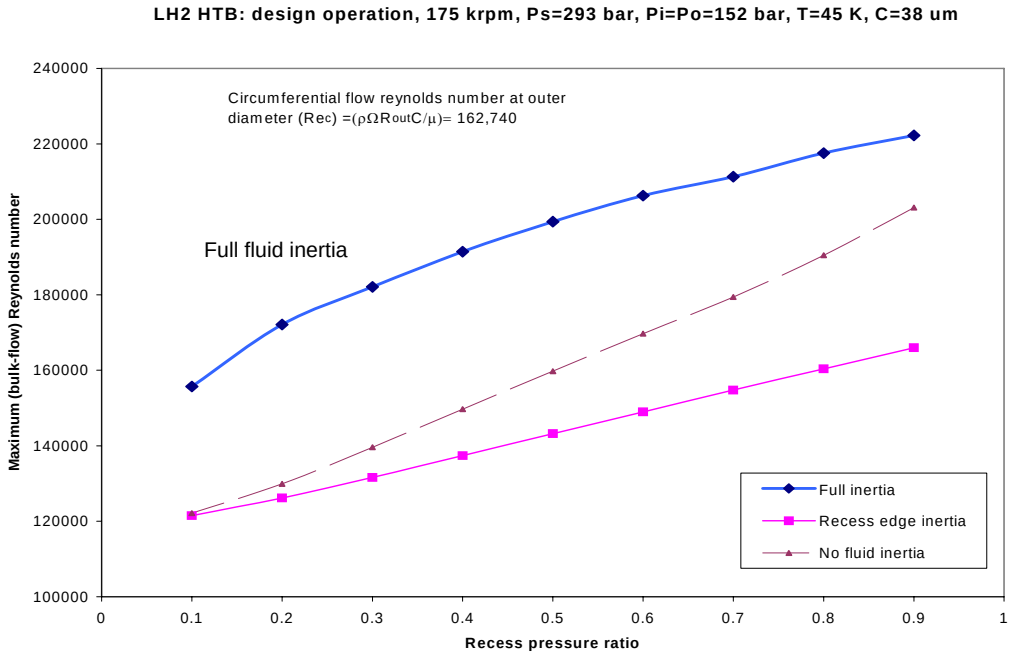

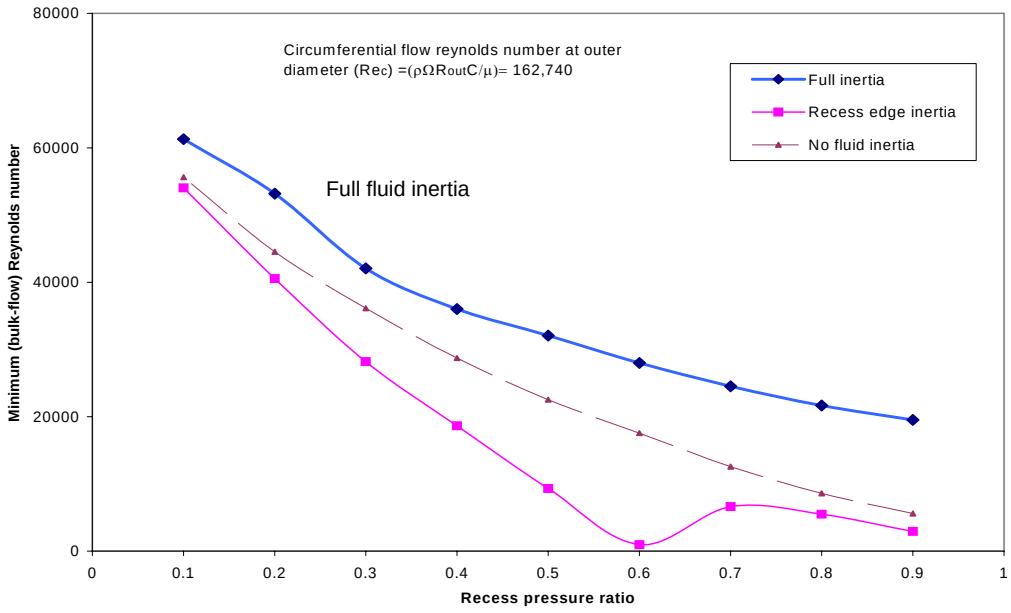

Figure 12. Maximum and minimum flow Reynolds numbers vs. recess pressure ratio for ALH thrust bearing.
(Effects of fluid inertia at film lands and recess edges)

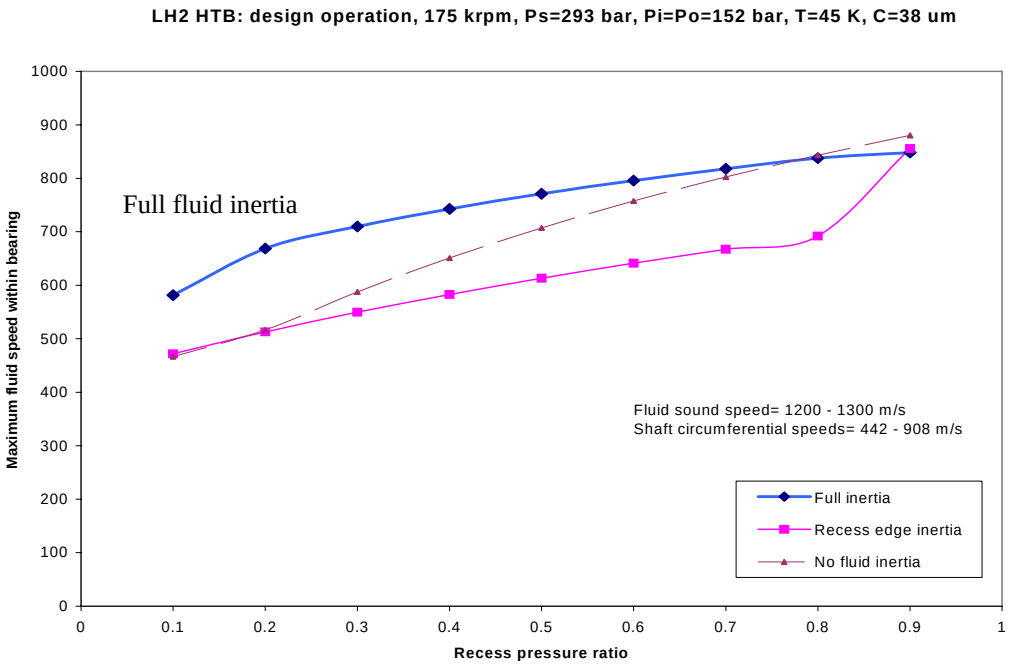

Figure 13. Maximum fluid speed flow Reynolds numbers vs. recess pressure ratio for ALH thrust bearing.
(Effects of fluid inertia at film lands and recess edges)

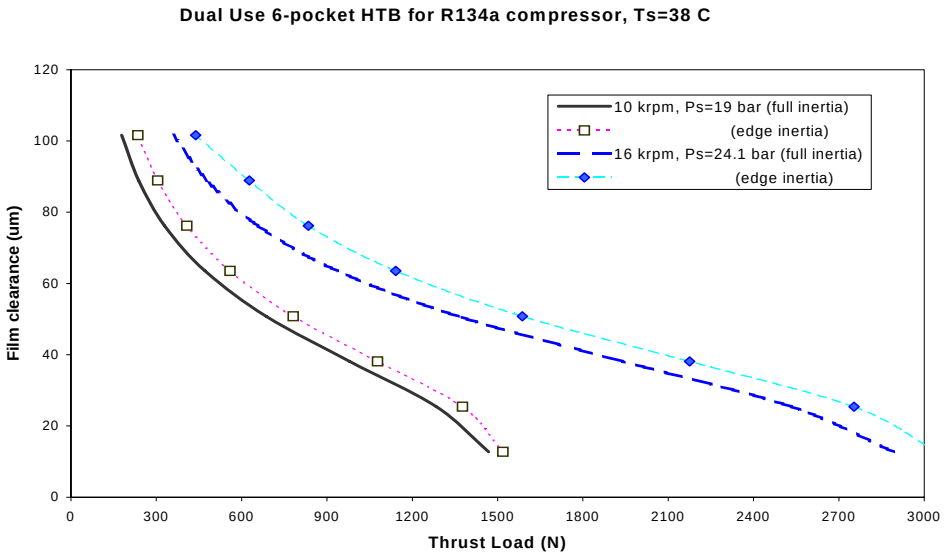

Figure 14. Film clearance (C) versus thrust load (W_Z) for refrigerant thrust bearing.
(Effects of fluid inertia at film lands and recess edges)

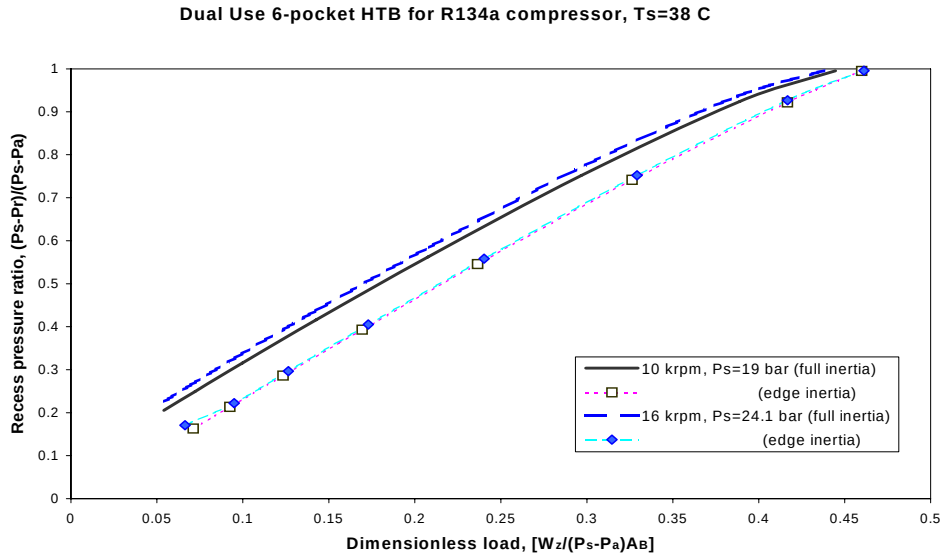

Figure 15. Recess pressure ratio versus dimensionless thrust load ($\bar{W}_Z$) for refrigerant thrust bearing.
(Effects of fluid inertia at film lands and recess edges)

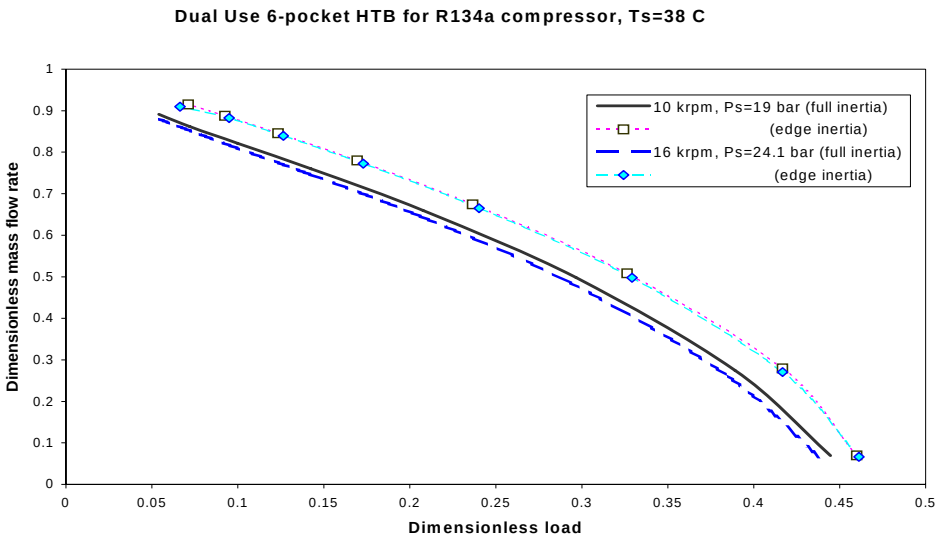

Figure 16(a). Dimensionless bearing mass flow rate versus thrust load ($\bar{W}_z$) for refrigerant thrust bearing.

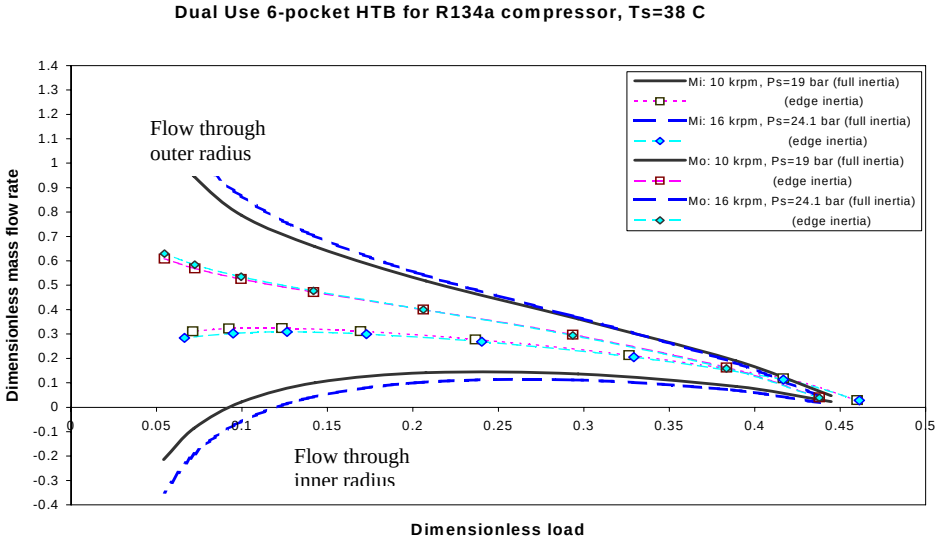

Figure 16(b). Mass flow rates (dim.) through inner and outer radii vs. versus thrust load ($\bar{W}_z$) for refrigerant thrust bearing.

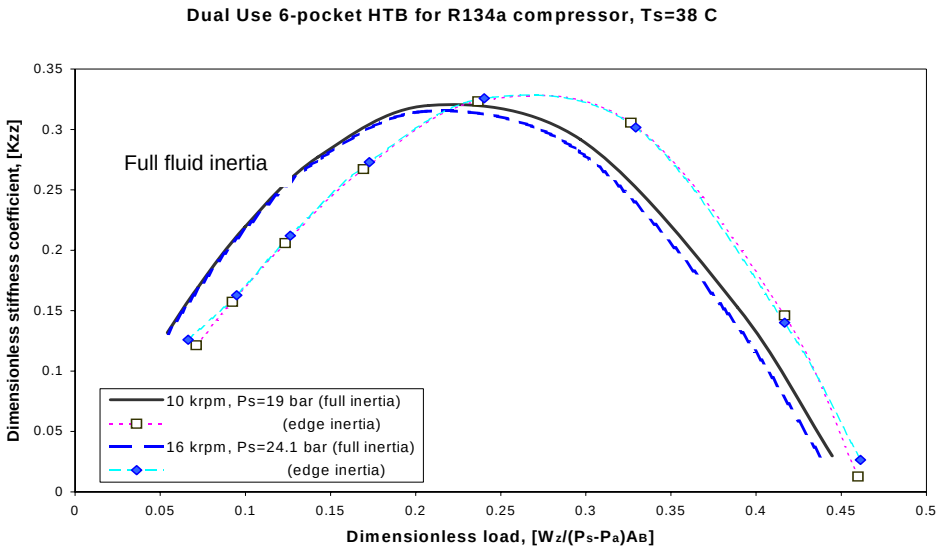

Figure 17. Dimensionless axial stiffness ($\bar{K}_{zz}$) coefficient vs. versus load ($\bar{W}_z$) for refrigerant thrust bearing.

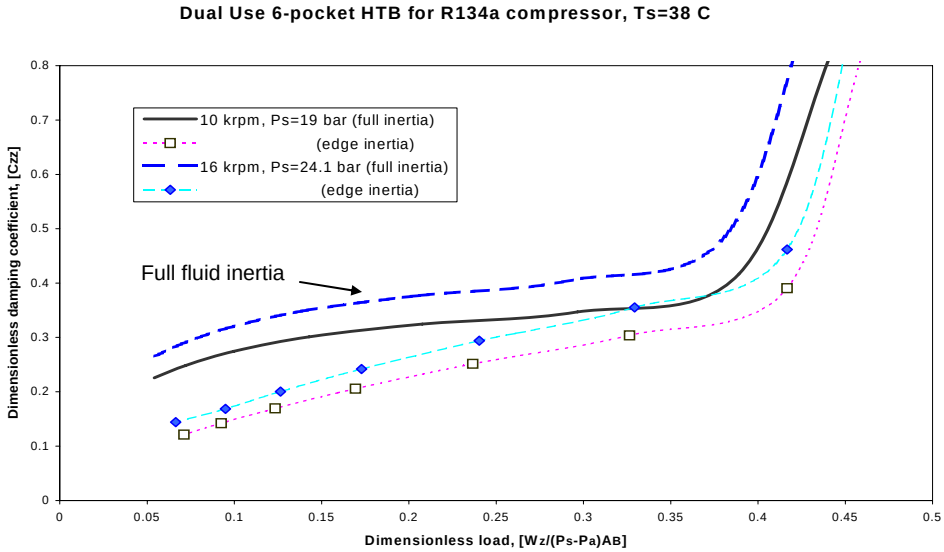

Figure 18. Dimensionless axial damping ($\bar{C}_{zz}$) coefficient versus load ($\bar{W}_z$) for refrigerant thrust bearing.

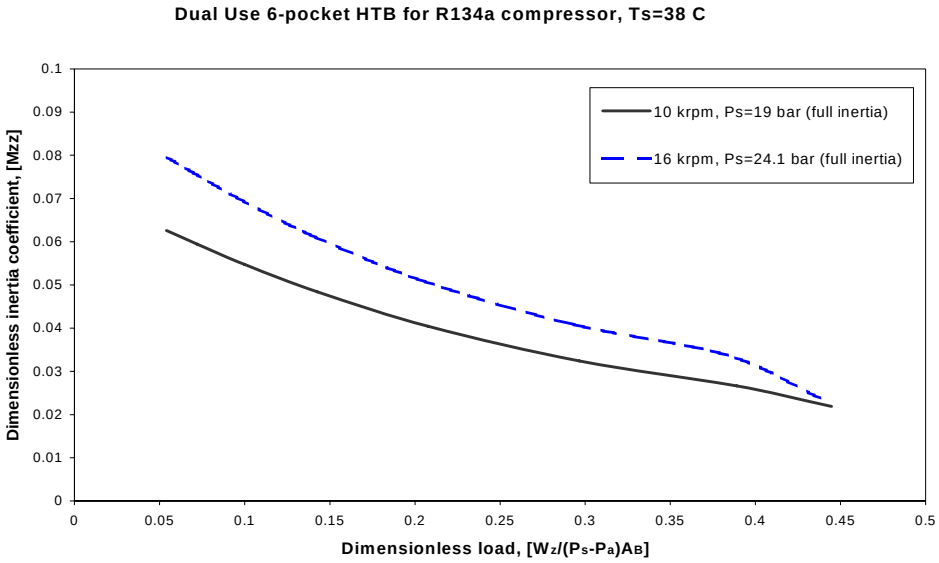

Figure 19. Dimensionless axial inertia ($\bar{M}_{zz}$) coefficient versus load ($\bar{W}_z$)for refrigerant thrust bearing.

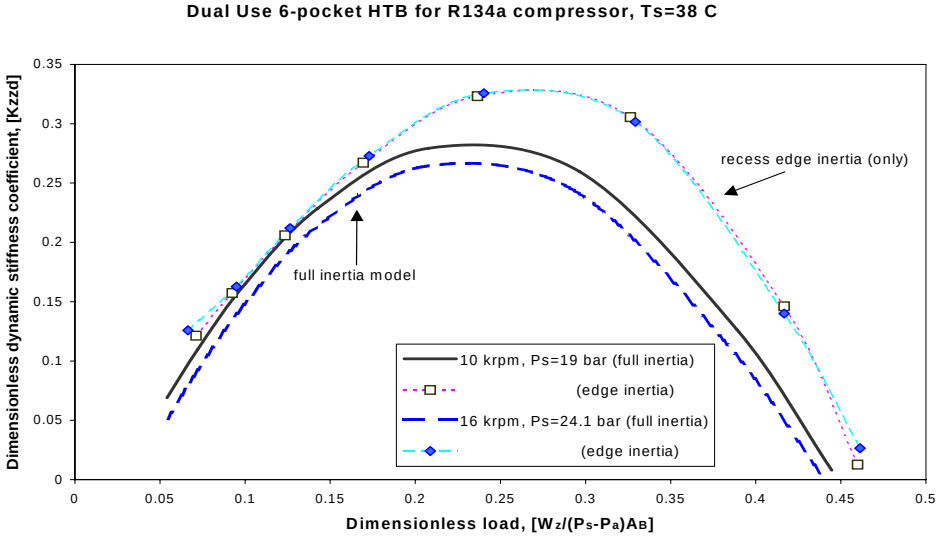

Figure 20. Dynamic stiffness coefficient ($\bar{K}_{zzd}= \bar{K}_{zz}- \bar{M}_{zz}\Omega^2$) versus load ($\bar{W}_z$)for refrigerant thrust bearing.

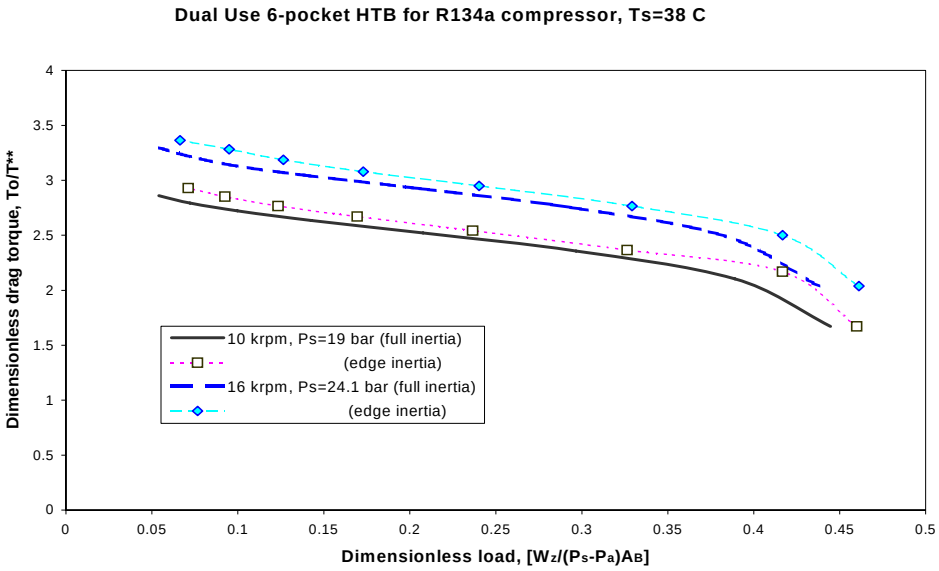

Figure 21. Dimensionless drag torque($\bar{T}o_{**}$). versus load ($\bar{W}z$) for refrigerant thrust bearing.

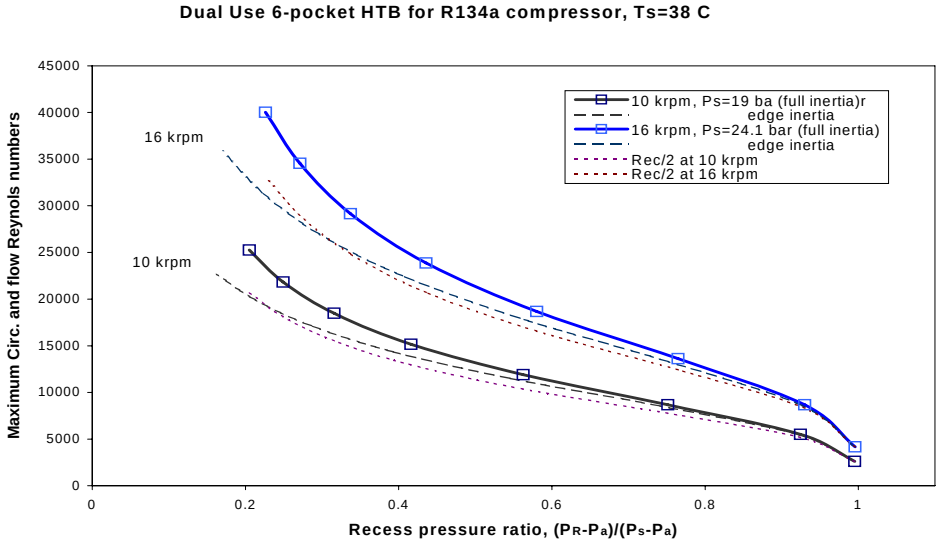

Figure 22. Maximum Reynolds numbers versus recess pressure ratio for refrigerant thrust bearing.

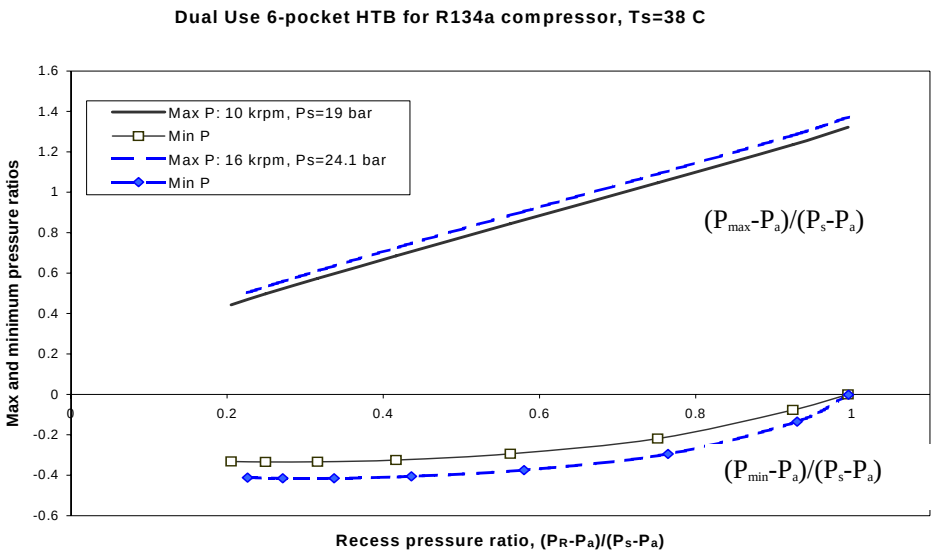

Figure 23. Maximum and minimum film (dimensionless) pressures versus recess pressure ratio for refrigerant thrust bearing.

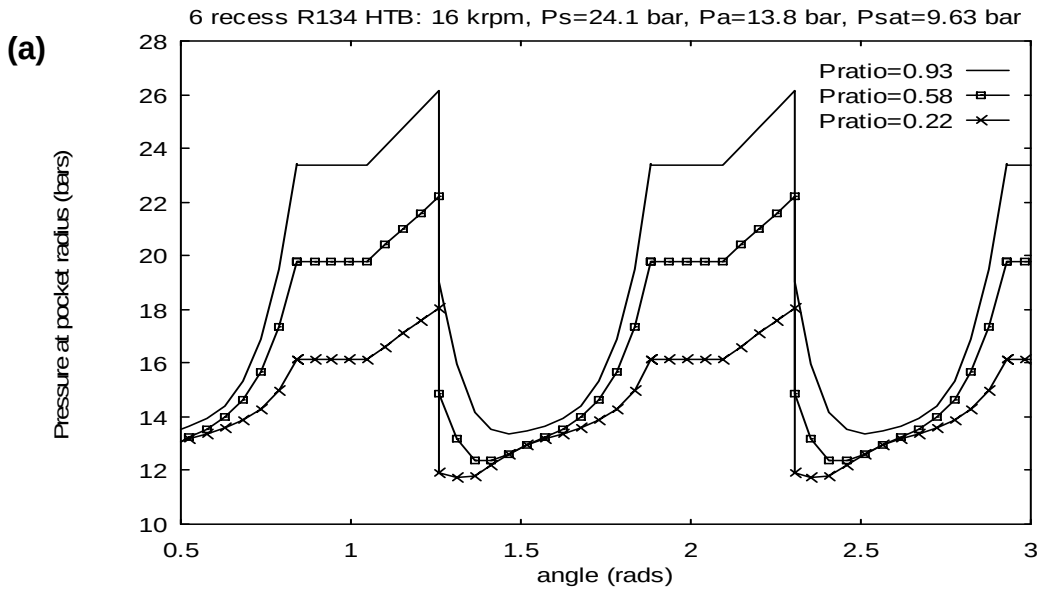

6 recess R134 HTB: 16 krpm, Ps=24.1 bar, Pa=13.8 bar, pratio=0.58

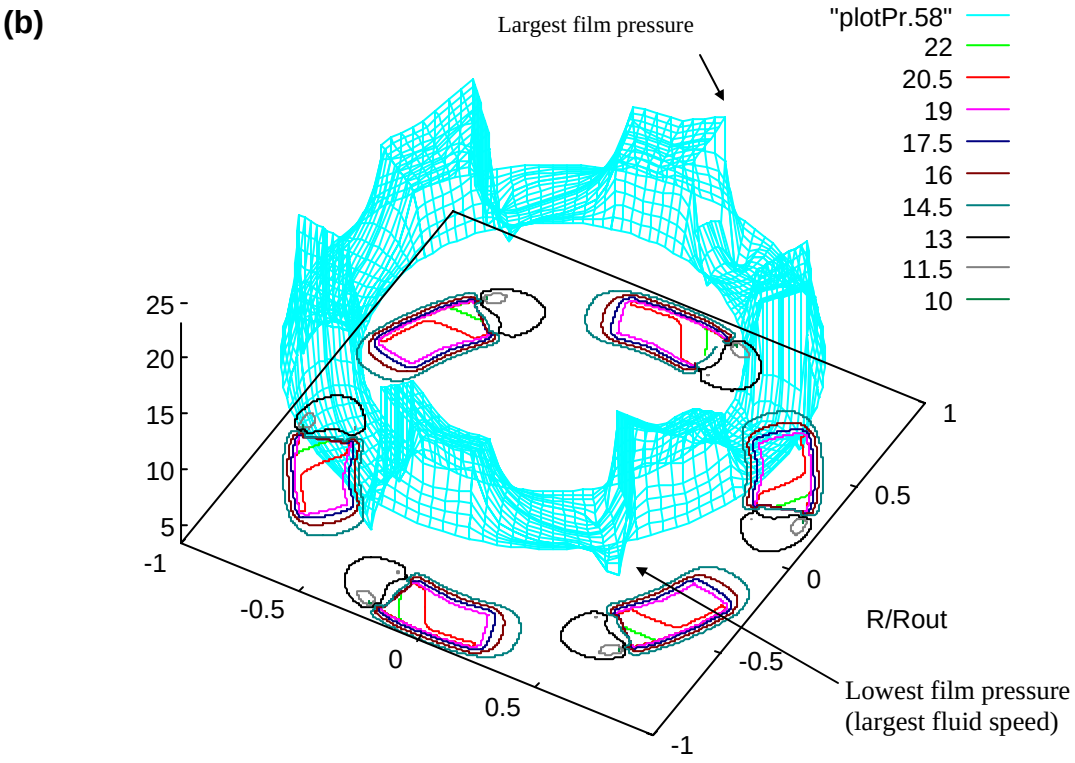

Figure 24. Film Pressures from full inertia model. (a) pressure at recess diameter for p_{ratio}=0.93, 0.58, 0.22, (b) pressure surface and contours for p_{ratio}=0.58

APPENDIX A

FIRST-ORDER WALL SHEAR STRESS COEFFICIENTS

The perturbed wall shear stress coefficients *((‘s)* for the first-order equations of radial and circumferential momentum and energy transport are given by the following expressions.

RADIAL MOMENTUM EQUATION:

$$\gamma_{rh} = \left(\frac{\bar{\mu}\ u_r}{h}\right)_0 \left[\frac{\partial \kappa_r}{\partial h} - 2\frac{\kappa_r}{h}\right]_0$$

$$\gamma_{r\mu} = \left(\frac{u_r}{h}\right)_0 \left[\bar{\mu}\frac{\partial \kappa_r}{\partial \bar{\mu}} + \kappa_r\right]_0 ; \quad \gamma_{r\rho} = \left(\frac{\bar{\mu}\ u_r}{h}\right)_0 \left[\frac{\partial \kappa_r}{\partial \bar{\rho}} - \frac{\kappa_r}{\bar{\rho}}\right]_0 - \left(\frac{h}{\bar{\rho}}\frac{\partial \bar{P}}{\partial r}\right)_0$$

$$\gamma_{rr} = \left(\frac{\bar{\mu}}{h}\right)_0 \left[\bar{\mu}_r \frac{\partial \kappa_r}{\partial u_r} + \kappa_r\right]_0 ; \quad \gamma_{r\theta} = \left(\frac{\bar{\mu}\ u_r}{h}\right)_0 \left[\frac{\partial \kappa_r}{\partial u_\theta}\right]_0$$

$$\gamma_{rP} = \gamma_{r\rho}\left(\frac{\partial \bar{\rho}}{\partial \bar{P}}\right)_0 + \gamma_{r\mu}\left(\frac{\partial \bar{\mu}}{\partial \bar{P}}\right)_0 ; \gamma_{rT} = \gamma_{r\rho}\left(\frac{\partial \bar{\rho}}{\partial \bar{T}}\right)_0 + \gamma_{r\mu}\left(\frac{\partial \bar{\mu}}{\partial \bar{T}}\right)_0$$

CIRCUMFERENTIAL MOMENTUM EQUATION:

$$\gamma_{\theta h} = \left(\frac{\bar{\mu}\ u_\theta}{h}\right)_0 \left[\frac{\partial \kappa_\theta}{\partial h} - 2\frac{\kappa_\theta}{h}\right]_0 - \frac{1}{2}\left(\frac{\bar{\mu}\ \Lambda\ r}{h}\right)_0 \left[\frac{\partial \kappa_S}{\partial h} - 2\frac{\kappa_S}{h}\right]_0$$

$$\gamma_{\theta\mu} = \left(\frac{u_\theta}{h}\right)_0 \left[\bar{\mu}\frac{\partial \kappa_\theta}{\partial \bar{\mu}} + \kappa_\theta\right]_0 - \frac{1}{2}\left(\frac{\Lambda\ r}{h}\right)_0 \left[\bar{\mu}\frac{\partial \kappa_S}{\partial \bar{\mu}} + \kappa_S\right]_0$$

$$\gamma_{\theta\rho} = \left(\frac{\bar{\mu} u_\theta}{h}\right)_0 \left[\frac{\partial \kappa_\theta}{\partial \bar{\rho}} - \frac{\kappa_\theta}{\bar{\rho}}\right]_0 - \frac{1}{2}\left(\frac{\bar{\mu}\Lambda\ r}{h}\right)_0 \left[\frac{\partial \kappa_S}{\partial \bar{\rho}} - \frac{\kappa_S}{\bar{\rho}}\right]_0 - \left(\frac{h}{\bar{\rho}}\frac{\partial \bar{P}}{r\,\partial\theta}\right)_0$$

$$\gamma_{\theta r} = \left(\frac{\bar{\mu}\ u_\theta}{h}\right)_0 \left[\frac{\partial \kappa_\theta}{\partial u_r}\right]_0 - \frac{1}{2}\left(\frac{\bar{\mu}\ \Lambda\ r}{h}\right)_0 \left[\frac{\partial \kappa_S}{\partial u_r}\right]_0$$

$$\gamma_{\theta\theta} = \left(\frac{\bar{\mu}}{h}\right)_0 \left[\kappa_\theta + u_\theta \frac{\partial \kappa_\theta}{\partial u_\theta}\right]_0 - \frac{1}{2}\left(\frac{\bar{\mu}\ \Lambda\ r}{h}\right)_0 \left[\frac{\partial \kappa_S}{\partial u_\theta}\right]_0$$

$$\gamma_{\theta p} = \gamma_{\theta\rho}\left[\frac{\partial\overline{\rho}}{\partial\overline{P}}\right]_0 + \gamma_{\theta\mu}\left[\frac{\partial\overline{\mu}}{\partial\overline{P}}\right]_0 \;;\quad \gamma_{\theta T} = \gamma_{\theta\rho}\left[\frac{\partial\overline{\rho}}{\partial\overline{T}}\right]_0 + \gamma_{\theta\mu}\left[\frac{\partial\overline{\mu}}{\partial\overline{T}}\right]_0$$

ENERGY TRANSPORT EQUATION

$$\gamma_{T\theta} = \frac{Re_{P^*}}{E_c}\left\{\overline{C}_{P0}\overline{\rho}_0 h_0 \frac{\partial\overline{T}_0}{r\,\partial\theta} + 2h_0\left[\frac{f_{B1}u_{\theta 0}}{\kappa_{BO}}\overline{Q}_{BO} + \frac{f_{S1}(u_{\theta 0} - \Lambda r)}{\kappa_{SO}}\overline{Q}_{SO}\right]\right\}$$

$$- \;\overline{\beta}_{T0}\,\overline{T}_0\,h_0\frac{\partial\overline{P}}{r\,\partial\theta} - \frac{\overline{\mu}_0}{h_0}\left[\kappa_{\theta 0}\left(2u_{\theta 0} + \frac{\Lambda r}{2}\right) - \Lambda r\,\kappa_{SO}\right]$$

$$- \;\overline{\mu}_0\left[(u_{c0} + 2u_{c1})(u_{\theta 0} - \Lambda r)\,f_{S1} + u_{c0}u_{\theta 0}\,f_{B1}\right]$$

$$\gamma_{Tr} = \frac{Re_{P^*}}{E_c}\left[\overline{C}_{P0}\overline{\rho}_0 h_0\frac{\partial\overline{T}_0}{\partial r} + 2h_0\,u_{r0}\left(\frac{f_{B1}}{\kappa_{BO}}\overline{Q}_{BO} + \frac{f_{S1}}{\kappa_{SO}}\overline{Q}_{SO}\right)\right] - \overline{\beta}_{T0}\,\overline{T}_0\,h_0\frac{\partial\overline{P}_0}{\partial r}$$

$$- \;\frac{\overline{\mu}_0}{h_0}(2\kappa_{r0}\,u_{r0}) - \overline{\mu}_0\,u_{r0}\left[u_{c0}(f_{B1} + f_{S1}) + 2u_{c1}\,f_{S1}\right]$$

$$\gamma_{TP} = \left[\gamma_{T\rho}\frac{\partial\overline{\rho}}{\partial\overline{P}} + \gamma_{T\mu}\frac{\partial\overline{\mu}}{\partial\overline{P}} + \gamma_{T\beta}\frac{\partial\overline{\beta}_T}{\partial\overline{P}} + \gamma_{TK}\frac{\partial\overline{K}}{\partial\overline{P}} + \gamma_{C_P}\frac{\partial\overline{C}_P}{\partial\overline{P}}\right]_0$$

$$\gamma_{TT} = \frac{Re_{P^*}}{E_c}\left(\overline{H}_{BO} + \overline{H}_{SO}\right) - \overline{\beta}_{T0}\,h_0\left(u_{\theta 0}\frac{\partial\overline{P}_0}{r\,\partial\theta} + u_{r0}\frac{\partial\overline{P}_0}{\partial r}\right)$$

$$+ \left[\gamma_{T\rho}\frac{\partial\overline{\rho}}{\partial\overline{T}} + \gamma_{T\mu}\frac{\partial\overline{\mu}}{\partial\overline{T}} + \gamma_{T\beta}\frac{\partial\overline{\beta}_T}{\partial\overline{T}} + \gamma_{TK}\frac{\partial\overline{K}}{\partial\overline{T}} + \gamma_{C_P}\frac{\partial\overline{C}_P}{\partial\overline{T}}\right]_0$$

$$\gamma_{Th} = \frac{Re_{P*}}{E_c}\left[\overline{C}_{P0}\overline{\rho}_0\left(u_{\theta 0}\frac{\partial \overline{T}_0}{r\,\partial\theta} + u_{r0}\frac{\partial \overline{T}_0}{\partial r}\right) + \frac{2}{h_0}\left(\frac{C_{cB}}{\kappa_{BO}}\overline{Q}_{BO} + \frac{C_{cS}}{\kappa_{SO}}\overline{Q}_{SO}\right)\right] - \frac{\Lambda}{2}\frac{\partial P_0}{\partial\theta}$$

$$- \overline{\beta}_{T0}\overline{T}_0\left(u_{\theta 0}\frac{\partial \overline{P}_0}{r\,\partial\theta} + u_{r0}\frac{\partial \overline{P}_0}{\partial r}\right) - \frac{\overline{\mu}_0}{h_0^2}\left[u_{c0}\left(C_{cS} + C_{cB}\right) + 2u_{c1}C_{cS}\right]$$

$$\gamma_{T\mu} = \frac{b_m}{h_0}\left[\frac{1}{2}u_{c0}\left(\gamma_S + \gamma_B\right) + u_{c1}\,\gamma_S\right] - \frac{Re_{P*}}{\overline{\mu}_0 E_c}\left[\frac{2}{3}\overline{Q}_{BS0} + \frac{\gamma_B b_m}{\kappa_{BO}}\overline{Q}_{BO} + \frac{\gamma_S b_m}{\kappa_{SO}}\overline{Q}_{SO}\right]$$

$$\gamma_{T\rho} = \frac{Re_{P*}}{E_c}\left[\overline{C}_{P0}\,h_0\left(u_{\theta 0}\frac{\partial \overline{T}_0}{r\,\partial\theta} + u_{r0}\frac{\partial \overline{T}_0}{\partial r}\right) + \frac{1}{\overline{\rho}_0}\left(\overline{Q}_{BS0} + \frac{\gamma_B b_m}{\kappa_{BO}}\overline{Q}_{BO} + \frac{\gamma_S b_m}{\kappa_{SO}}\overline{Q}_{SO}\right)\right]$$

$$- \frac{\overline{\mu}_0}{\overline{\rho}_0 h_0}\left\{u_{c0}\left[\kappa_{\theta 0} + \frac{b_m}{2}\left(\gamma_S + \gamma_B\right)\right] + u_{c1}\left(\kappa_{S0} + b_m\gamma_S\right)\right\}$$

$$\gamma_{T\beta} = - h_0\,\overline{T}_0\left(u_{\theta 0}\frac{\partial \overline{P}_0}{r\,\partial\theta} + u_{r0}\frac{\partial \overline{P}_0}{\partial r}\right)$$

$$\gamma_{TK} = \frac{2}{3}\,\frac{Re_P^*}{E_c}\,\frac{\overline{Q}_{BS0}}{\overline{K}_0}$$

$$\gamma_{Cp} = \frac{Re_{P*}}{E_c}\left[\overline{\rho}_0 h_0\left(u_{\theta 0}\frac{\partial \overline{T}_0}{r\,\partial\theta} + u_{r0}\frac{\partial \overline{T}_0}{\partial r}\right) + \frac{1}{3}\frac{\overline{Q}_{BS0}}{\overline{C}_{P0}}\right]$$

where

$$C_{cS} = \frac{1}{2}\left[Re_{SO}\,C_S + b_m\right]\gamma_S\,; \quad C_{cB} = \frac{1}{2}\left[Re_{BO}\,C_B + b_m\right]\gamma_B\,,$$

$$C_S = c_m\frac{r_S}{H_0}\,; \quad C_B = c_m\frac{r_B}{H_0}\,,$$

$$Re_{SO} = Re_P \left(\frac{\overline{\rho}_0}{\overline{\mu}_0} \right) h_0 \left[(u_{\theta 0} - \Lambda r)^2 + u_{r0}^2 \right]^{1/2} ; \; Re_{BO} = Re_P \left(\frac{\overline{\rho}_0}{\overline{\mu}_0} \right) h_0 \left[u_{\theta 0}^2 + u_{r0}^2 \right]^{1/2}$$

$$\gamma_S = \frac{-a_m \cdot e_m}{\left[(f_{S0} / a_m) - 1 \right]^{(1/e_m - 1)}} \; ; \quad \gamma_B = \frac{-a_m \cdot e_m}{\left[(f_{B0} / a_m) - 1 \right]^{(1/e_m - 1)}} \; ,$$

$$f_{S0} = a_M \left[1 + \left(c_M \frac{r_S}{H_0} + \frac{b_M}{Re_{S0}} \right)^{e_M} \right] ; \; f_{B0} = a_M \left[1 + \left(c_M \frac{r_B}{H_0} + \frac{b_M}{Re_{B0}} \right)^{e_M} \right]$$

$$f_{S1} = \frac{\left(Re_P \, \overline{\rho}_0 / \overline{\mu}_0 \right)^2 h_0}{2 \, Re_{SO}} \left[f_{S0} + \beta_S \gamma_S \right] ; \quad f_{B1} = \frac{\left(Re_P \, \overline{\rho}_0 / \overline{\mu}_0 \right)^2 h_0}{2 \, Re_{BO}} \left[f_{B0} + \beta_B \gamma_B \right] ;$$

$$\beta_S = b_m / Re_{SO} \; ; \quad \beta_B = b_m / Re_{BO} \; ,$$

$$u_{c0} = u_{\theta 0}^2 + u_{r0}^2 + u_{\theta 0} \frac{\Lambda r}{2} ; \quad u_{c1} = \frac{(\Lambda r)^2}{4} - u_{\theta 0} \Lambda \, r \, ,$$

$$\overline{Q}_{BO} = \overline{H}_{BO} \left(\overline{T}_0 - \overline{T}_{BO} \right) ; \quad \overline{Q}_{SO} = \overline{H}_{SO} \left(\overline{T}_0 - \overline{T}_{SO} \right) ; \quad \overline{Q}_{BS0} = \overline{Q}_{BO} + \overline{Q}_{SO}$$

and the following coefficients for evaluation of the Moody's friction factors,

$$a_M = 0.001375; \; b_M = 5 \cdot 10^5 \; ; \; c_M = 1 \cdot 10^4 \; ; \; e_M = \frac{1}{3}$$

APPENDIX B

Revised January 7, 2005

ALGEBRAIC BULK-FLOW EQUATIONS ON THE THIN FILM LANDS OF A THRUST BEARING

The flow field is represented by a series of discrete nodal bulk-flow velocities, fluid pressures and temperatures on staggered grids (Patankar, 1980). The dimensionless zeroth- and first-order bulk flow field variables $\{u_r, u_\theta, \overline{P}, \overline{T}\}_{0,1}$ are represented by the discrete (algebraic) fields $\{U, V, \overline{P}, \overline{T}\}$, and $\{U_1, V_1, \overline{P}_1, \overline{T}_1\}$, respectively. Figure B.1 shows the arrangement of staggered control-volumes for discretization of the thin film flow equations in a polar coordinate system *(r,θ)*.

The continuity equation, circumferential and radial momentum transport equations, and the energy transport equation are integrated on the P-, U-, V-, T-control volumes depicted in Figure B.1, in order to obtain a set of algebraic difference equations for the discrete flow variables.

ADDITIONAL NOMENCLATURE

A	coefficients of discrete algebraic equations
D	coefficients relating velocity to differences of pressure corrections
h	dimensionless film thickness
m	mass flow rates across faces of control-volumes
S	source terms in algebraic equations
(r,θ)	radial and angular polar coordinates
$\{U, V, \overline{P}, \overline{T}\}$	discrete zeroth-order circumferential and radial velocities, pressure and temperature
$\{U, V, \overline{P}, \overline{T}\}_1$	discrete first-order circumferential and radial velocities, pressure and temperature
$\{u', v', \overline{p}'\}$	correction velocities and pressures
δr, rδθ	sizes of control volume in radial and circumferential directions

Superscripts

u	refers to U-control volume (circumferential direction)
v	refers to V-control volume (radial direction)
P	refers to P-control volume (continuity and pressure correction equations)
T	refers to T-control volume (energy transport equation)
*	estimated flow variable.
‘	correction flow variable

Subscripts

p	refers to nodal value of variable at center of control volume
E,W, S,N	refers to values of variables at East, West, South and North nodes relative to p-value
e,w, s,n	refers to values of variables on east, west, south and north (face) sides of control volume.
1	first-order (perturbed) flow variable

Operators

$|| o, a || = \max(0, a)$; $\langle a, b \rangle_1 = a_1 b_0 + a_0 b_1$

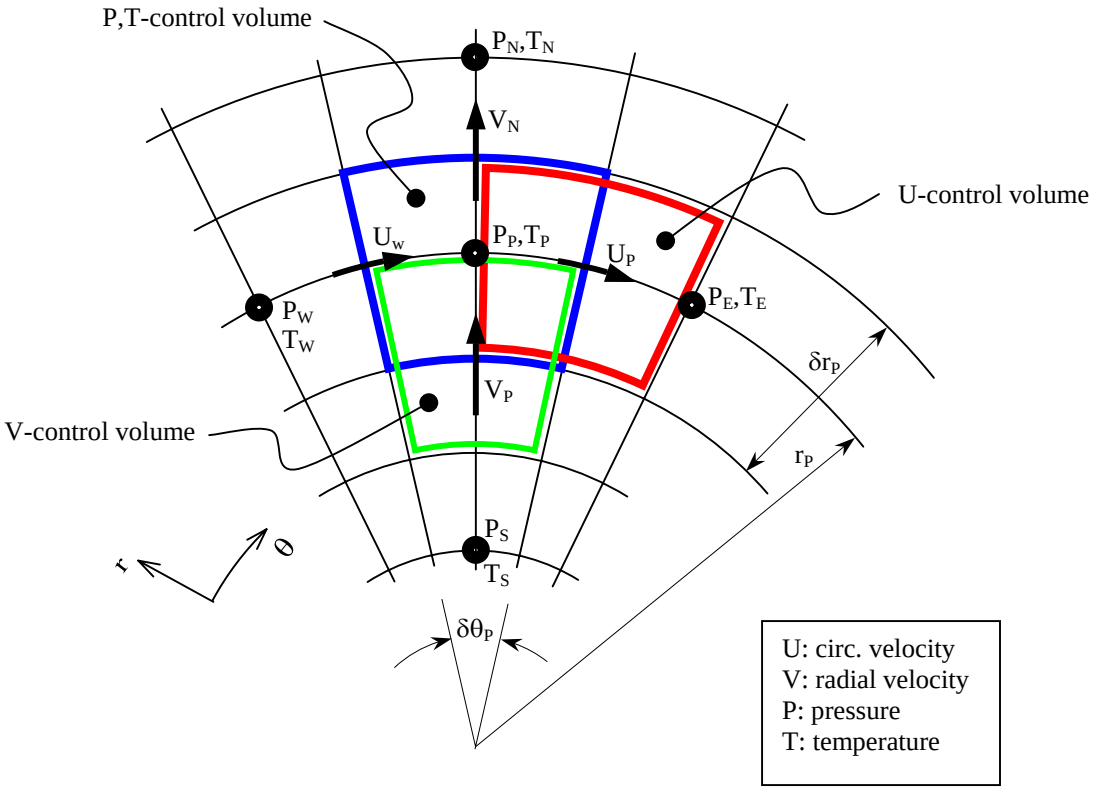

Figure B.1. Staggered control volumes for integration of bulk-flow equations in polar coordinates (r,θ)

Continuity (mass conservation) algebraic equations:

zeroth-order equation:

$$m_e^P - m_w^P + m_n^P - m_s^P = 0 \tag{B.1}$$

first-order equation:

$$m_{1e}^P - m_{1w}^P + m_{1n}^P - m_{1s}^P + i\sigma \langle \bar{\rho} h \rangle_1^P r_P^P \delta r_P^P \delta\theta_P^P = 0 \tag{B.2}$$

where

$$\begin{aligned} &m_e^P = (\bar{\rho} hU)_e^P \delta r_p^P; \quad m_w^P = (\bar{\rho} hV)_w^P \delta r_p^P; \quad m_{1e}^P = \langle \bar{\rho} hU \rangle_{1e}^P \delta r_p^P; \quad m_{1w}^P = \langle \bar{\rho} hV \rangle_{1w}^P \delta r_p^P; \\ &m_s^P = (\bar{\rho}\ hV)_s^P r_s^P \delta\theta_p^P; \; m_n^P = (\bar{\rho}\ hV)_n^P r_n^P \delta\theta_p^P; \; m_{1s}^P = \langle \bar{\rho}\ hV \rangle_{1s}^P r_s^P \delta\theta_p^P; \; m_n^P = \langle \bar{\rho}\ hV \rangle_{1n}^P r_n^P \delta\theta_p^P; \end{aligned} \tag{B.3}$$

and the following notation

$$\begin{aligned} \langle \bar{\rho} h V \rangle_1 &= \bar{\rho}_1 h_0 V_0 + \bar{\rho}_0 h_1 V_0 + \bar{\rho}_0 h_0 V_1; \\ \langle \bar{\rho} h U \rangle_1 &= \bar{\rho}_1 h_0 U_0 + \bar{\rho}_0 h_1 U_0 + \bar{\rho}_0 h_0 U_1; \\ \langle \bar{\rho} h \rangle_1 &= \bar{\rho}_1 h_0 + \bar{\rho}_0 h_1 \end{aligned} \tag{B.4}$$

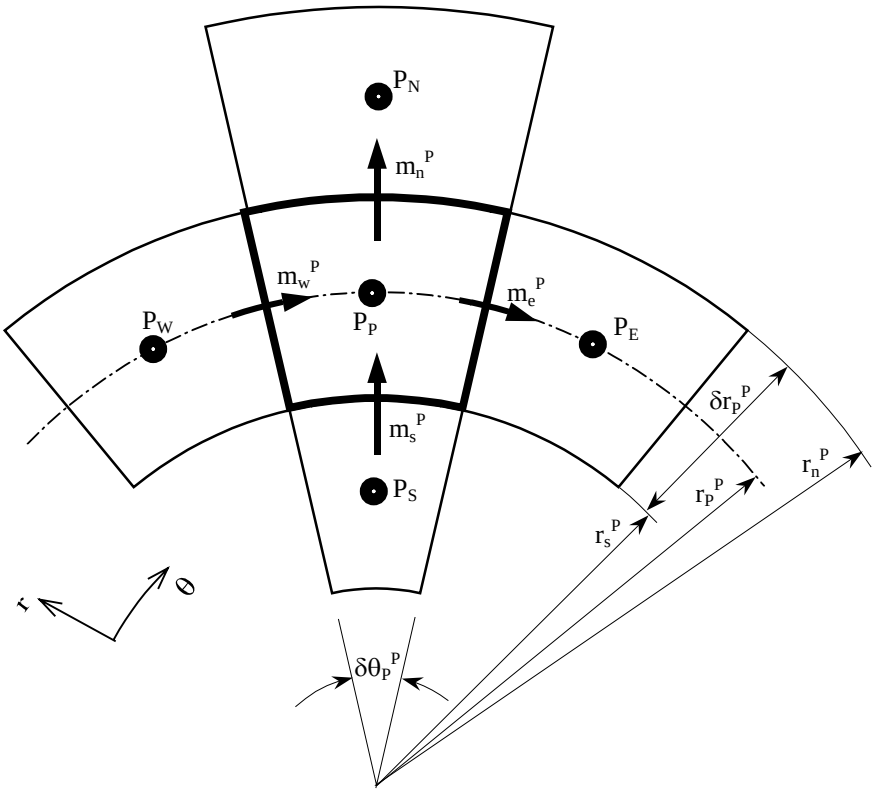

Figure B.2. P-control volume for integration of continuity equation and pressure correction equation

Circumferential momentum transport algebraic equation:

zeroth-order equation:

$$A_p^u U_p = A_E^u U_E + A_W^u U_W + A_S^u U_S + A_N^u U_N + S_{\Lambda p}^u - S_{\theta r}^u + h_p^u (\overline{P}_p - \overline{P}_E)^u \, \delta r_p^u \tag{B.5}$$

first-order equation:

$$A_{1p}^u U_{1p} = A_E^u U_{1E} + A_W^u U_{1W} + A_S^u U_{1S} + A_N^u U_{1N} + S_{1Sp}^u + h_p^u (\overline{P}_{1p} - \overline{P}_{1E})^u \, \delta r_p^u \tag{B.6}$$

where

$$A_p^u = A_E^u + A_W^u + A_S^u + A_N^u + S_p^U \tag{B.7}$$

$$\begin{aligned} A_{1p}^u = {} & A_E^u + A_W^u + A_S^u + A_N^u + \left\{ \gamma_{\theta\theta} + i \, \overline{\rho} \, h \, Re_\sigma \right\}_P^u r_p^u \, \delta r_p^u \, \delta\theta_p^u + \\ & Re_{p*} \left(m_e - m_w \right)^u + Re_{p*} \left(\overline{\rho} \, h \, V \right)_p^u \, \delta r_p^u \, \delta\theta_p^u \end{aligned} \tag{B.8}$$

with the zeroth- and first-order source terms,

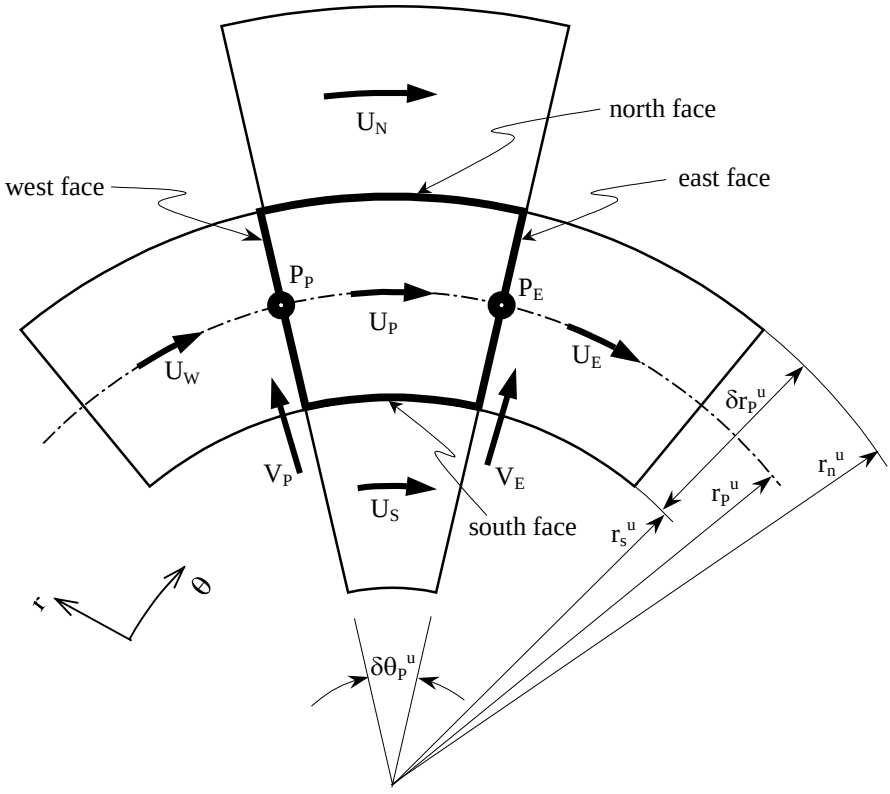

Figure B.3. U-control volume for integration of circumferential bulk-flow momentum equation

$$S_p^u = \left(\frac{\bar{\mu}\,\kappa_\theta}{h}\right)_p^u r_p^u\,\delta r_p^u\,\delta\theta_p^u; \qquad S_{\Lambda p}^u = \left(\frac{\bar{\mu}\,\kappa_s}{h}\right)_p^u \left[\frac{\Lambda}{2} r_p^u\right] r_p^u\,\delta r_p^u\,\delta\theta_p^u;$$
$$S_{\theta r}^u = \mathrm{Re}_{p*}\left(\bar{\rho}\,hV\right)_p^u U_p\,\delta r_p^u\,\delta\theta_p^u; \tag{B.9}$$

$$-S_{1Sp}^u = \left\{\gamma_{\theta h}\,h_1 + \gamma_{\theta P}\,\bar{P}_1 + \gamma_{\theta T}\,\bar{T}_1\right\}_p^u r_p^u\,\delta r_p^u\,\delta\theta_p^u + V_{1p}\left\{\gamma_{\theta r}\,r_p^u\,\delta r_p^u\,\delta\theta_p^u + \mathrm{Re}_{P*}\left(\bar{\rho}\,h\right)_p^u \delta\theta_p^u\left[\left(U_n - U_s\right)^u r_p^u + U_p\,\delta r_p^u\right]\right\} \tag{B.10}$$

and

$$\gamma_{\theta P} = \gamma_{\theta\rho}\left(\partial\bar{\rho}/\partial\bar{P}\right)_0 + \gamma_{\theta\mu}\left(\partial\bar{\mu}/\partial\bar{T}\right)_0; \quad \gamma_{\theta T} = \gamma_{\theta\rho}\left(\partial\bar{\rho}/\partial\bar{P}\right)_0 + \gamma_{\theta\mu}\left(\partial\bar{\mu}/\partial\bar{T}\right)_0 \tag{B.11}$$

with the fluid flow advection coefficients,

$$A_E^u = \mathrm{Re}_{p_*} \| 0, -m_e^u \|, \quad m_e^u = \left(\bar{\rho}\,hU\right)_e^u \delta r_p^u; \qquad A_W^u = \mathrm{Re}_{p_*} \| 0, +m_w^u \|, \quad m_w^u = \left(\bar{\rho}\,hU\right)_w^u \delta r_p^u;$$
$$A_S^u = \mathrm{Re}_{p_*} \| 0, +m_s^u \|, \quad m_s^u = \left(\bar{\rho}\;hV\right)_s^u r_s^u \delta\theta_p^u; \quad A_N^u = \mathrm{Re}_{p_*} \| 0, -m_n^u \|, \quad m_n^u = \left(\bar{\rho}\;hV\right)_n^u r_n^u \delta\theta_p^u; \tag{B.12}$$

where the operator $\| 0, a \| = \max(0, a)$

Radial momentum transport algebraic equation:

zeroth-order equation:

$$A_p^v V_p = A_E^v V_E + A_W^v V_W + A_S^v V_S + A_N^v V_N + S_{r\theta}^v + h_p^v (\overline{P}_S - \overline{P}_p)^v \, r_p^v \delta\theta_p^v \qquad \text{(B.13)}$$

first-order equation:

$$A_{1p}^v V_{1p} = A_E^v V_{1E} + A_W^v V_{1W} + A_S^v V_{1S} + A_N^v V_{1N} + S_{1Sp}^v + h_p^u (\overline{P}_{1S} - \overline{P}_{1p})^v \; r_p^v \, \delta\theta_p^v \qquad \text{(B.14)}$$

where

$$A_p^v = A_E^v + A_W^v + A_S^v + A_N^v + S_p^v \qquad \text{(B15)}$$

$$A_{1p}^v = A_E^v + A_W^v + A_S^v + A_N^v + \left\{\gamma_{rr} + i\,\overline{\rho}\, h\, Re_\sigma\right\}_p^v r_p^v \, \delta r_p^v \, \delta\theta_p^v + Re_{p*}\left(m_n - m_s\right)^v \qquad \text{(B.16)}$$

with the zeroth- and first-order source terms,

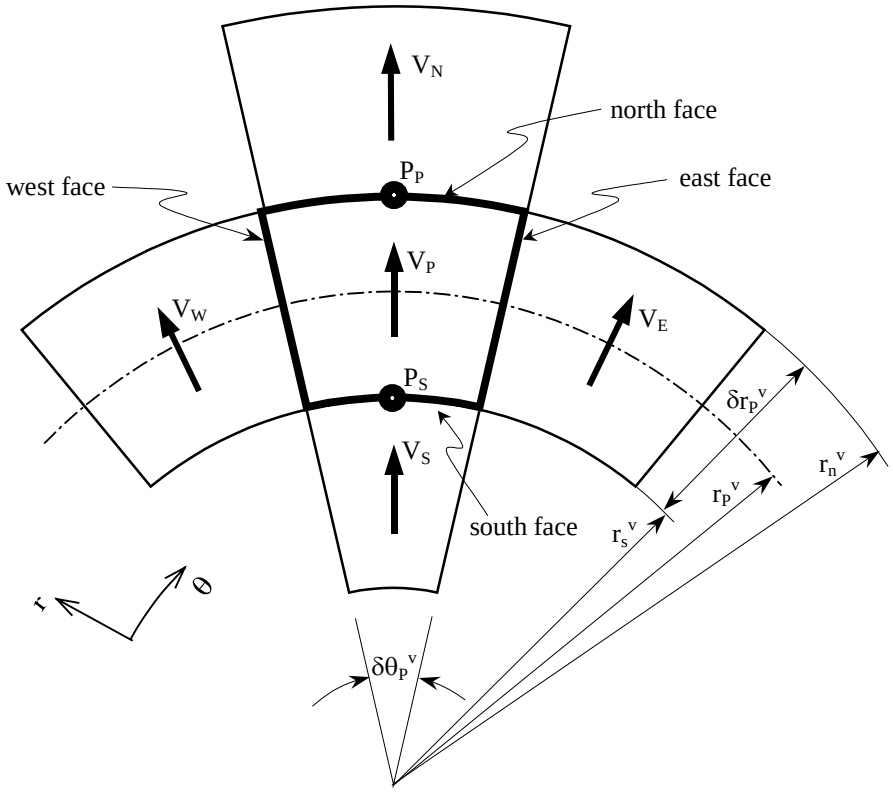

Figure B.4. V-control volume for integration of radial bulk-flow momentum equation

$$S_p^v = \left(\frac{\bar{\mu}\,\kappa_r}{h}\right)_p^v r_p^v\,\delta r_p^v\,\delta\theta_p^v; \qquad S_{r\theta}^v = Re_{p*}\left(\bar{\rho}\,hU^2\right)_p^v \delta r_p^v\,\delta\theta_p^v; \tag{B.17}$$

$$\begin{aligned} -S_{1Sp}^v = &\left\{\gamma_{rh}\,h_1 + \gamma_{rP}\,P_1 + \gamma_{rT}\,\bar{T}_1\right\}_p^v r_p^v\,\delta r_p^v\,\delta\theta_p^v + \\ &U_{1p}\left\{\gamma_{r\theta}\; r_p^v\,\delta r_p^v\,\delta\theta_p^v + Re_{P*}\left(\bar{\rho}\,h\right)_p^v \delta r_p^v\left[\left(V_e - V_w\right)^v - 2\,U_p\,\delta\theta_p^v\right]\right\} \end{aligned} \tag{B.18}$$

and

$$\gamma_{rP} = \gamma_{r\rho}\left(\partial\bar{\rho}/\partial\bar{P}\right)_0 + \gamma_{r\mu}\left(\partial\bar{\mu}/\partial\bar{T}\right)_0; \quad \gamma_{rT} = \gamma_{r\rho}\left(\partial\bar{\rho}/\partial\bar{P}\right)_0 + \gamma_{r\mu}\left(\partial\bar{\mu}/\partial\bar{T}\right)_0 \tag{B.19}$$

with the fluid flow advection coefficients,

$$\begin{aligned} &A_E^v = Re_{p_*}\,\|\,0,-m_e^v\,\|, \quad m_e^v = \left(\bar{\rho}\,hU\right)_e^v \delta r_p^v; \quad A_W^v = Re_{p_*}\,\|\,0,+m_w^v\,\|, \quad m_w^v = \left(\bar{\rho}\,hU\right)_w^v \delta r_p^v; \\ &A_S^v = Re_{p_*}\,\|\,0,+m_s^v\,\|, \quad m_s^v = \left(\bar{\rho}\,hV\right)_s^v r_s^v \delta\theta_p^v; A_N^v = Re_{p_*}\,\|\,0,-m_n^v\,\|, \quad m_n^v = \left(\bar{\rho}\,hV\right)_n^v r_n^v \delta\theta_p^v; \end{aligned} \tag{B.20}$$

Energy transport algebraic equation:

zeroth-order equation:

$$A_p^T \overline{T}_p = A_E^T \overline{T}_E + A_W^T \overline{T}_W + A_S^T \overline{T}_S + A_N^T \overline{T}_N + S_p^T \tag{B.21}$$

first-order equation:

$$A_{1p}^T \overline{T}_{1p} = A_E^T \overline{T}_{1E} + A_W^T \overline{T}_{1W} + A_S^T \overline{T}_{1S} + A_N^T \overline{T}_{1N} + S_{1p}^T \tag{B.22}$$

where

$$A_p^T = A_E^T + A_W^T + A_S^T + A_N^T + S_{p1}^T + \| 0, S_{p2}^T \| \tag{B.23}$$

$$A_{1p}^T = A_E^T + A_W^T + A_S^T + A_N^T + \left\{ \gamma_{TT} + i \overline{\rho}\, \overline{C}_p h \left(Re_\sigma / E_c \right) \right\}_p^v r_p^v \, \delta r_p^v \, \delta\theta_p^v \tag{B.24}$$

with the zeroth- and first-order source terms,

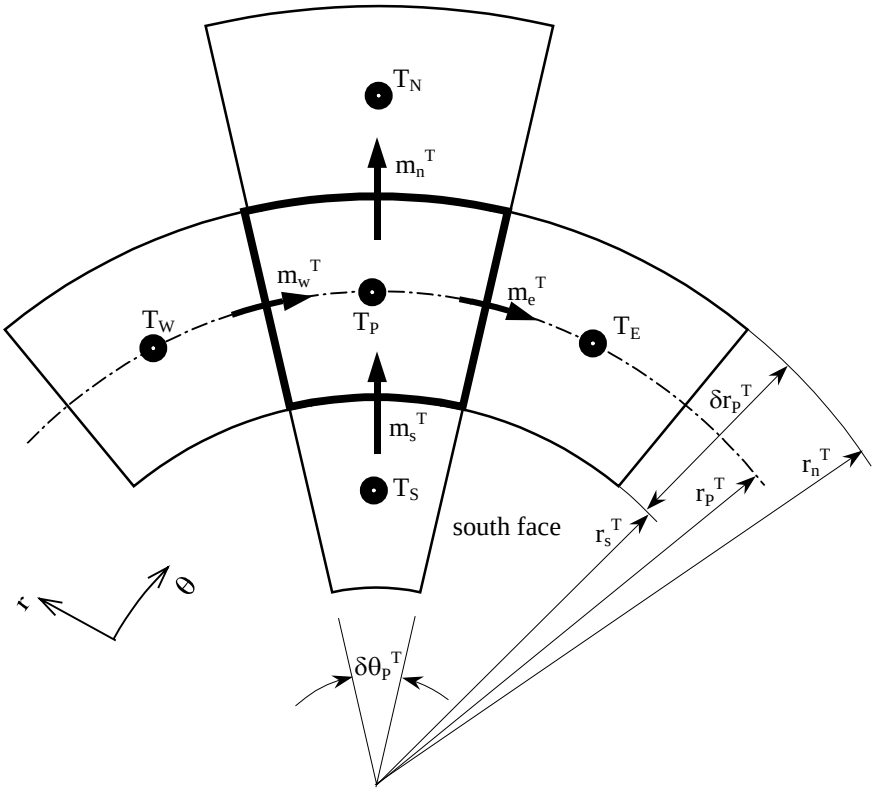

Figure B.5. T-control volume for integration of energy transport (fluid temperature) equation

$$S_p^T = \frac{\overline{\mu}_p^T}{h_p^T}\left(\kappa_\theta\left[U^2+V^2+\frac{1}{2}U\Lambda r\right]+\kappa_s\,\Lambda r\left[\frac{1}{4}\Lambda r - U\right]\right)_p^T r_p^T\,\delta r_p^T\,\delta\theta_p^T \; + \\ \frac{\Lambda r_p^T}{2} h_p^T\left(\overline{P}_e-\overline{P}_w\right)^T \delta r_p^T + (\mathrm{Re}_{p*}/E_c)(\overline{H}_B\overline{T}_B+\overline{H}_S\overline{T}_S)_p^T\, r_p^T\,\delta r_p^T\,\delta\theta_p^T + \| 0, -S_{p2}^T \|\overline{T}_p^T \tag{B.25}$$

$$S_{p1}^T = (\mathrm{Re}_{p*}/E_c)(\overline{H}_B+\overline{H}_S)_p^T\, r_p^T\,\delta r_p^T\,\delta\theta_p^T \tag{B.26}$$

$$S_{p2}^T = -\overline{\beta}_T\, h_p^T\left\{U_p^T\left[\overline{P}_e-\overline{P}_w\right]^T\delta r_p^T + V_p^T\left[\overline{P}_n-\overline{P}_s\right]^T r_p^T\,\delta\theta_p^T\right\} \tag{B.27}$$

$$S_{1p}^T = -\left\{\gamma_{Th}\,h_1+\gamma_{T\theta}\,U_1+\gamma_{Tr}\,V_1+\left(\gamma_{TP}-i\,\sigma\overline{\beta}_T\,h\,\overline{T}\right)P_1\right\}_p^v r_p^v\,\delta r_p^v\,\delta\theta_p^v \\ +\left(\overline{\beta}_T\overline{T}\,h\,U+h\frac{\Lambda r}{2}\right)_p^T\left(\overline{P}_{1e}-\overline{P}_{1w}\right)^T\delta r_p^T+\left(\overline{\beta}_T\overline{T}\,h\,V\right)_p^T\left(\overline{P}_{1n}-\overline{P}_{1s}\right)^T r_p^T\delta\theta_p^T \tag{B.28}$$

with the fluid flow advection coefficients,

$$\begin{aligned} A_E^T &= \overline{C}_p(\mathrm{Re}_{p*}/E_c)\,\|0,-m_e^T\|, & m_e^T &= (\overline{\rho}\,hU)_e^T\,\delta r_p^T; \\ A_W^T &= \overline{C}_p(\mathrm{Re}_{p*}/E_c)\,\|0,+m_w^T\|, & m_w^T &= (\overline{\rho}\,hU)_w^T\,\delta r_p^T; \\ A_S^T &= \overline{C}_p(\mathrm{Re}_{p*}/E_c)\,\|0,+m_s^T\|, & m_s^T &= (\overline{\rho}\,hV)_s^T\,r_s^T\,\delta\theta_p^T; \\ A_N^T &= \overline{C}_p(\mathrm{Re}_{p*}/E_c)\,\|0,-m_n^T\|, & m_n^T &= (\overline{\rho}\,hV)_n^T\,r_n^T\,\delta\theta_p^T; \end{aligned} \tag{B.29}$$

Pressure correction equations

Let the flow variables be given as

$$U = U^* + u';\; V = V^* + v';\; \overline{P} = \overline{P}^* + \overline{p}'; \tag{B.30}$$

$$U_1 = U_1^* + u_1';\; V_1 = V_1^* + v_1';\; \overline{P}_1 = \overline{P}_1^* + \overline{p}_1'$$

where the (*) fields are assumed to satisfy the momentum equations but not the continuity equation. The (‘) fields are corrections to be determined from satisfaction of the mass flow continuity equation(s), zeroth and first-order. The fields above are substituted into the momentum transport equations, and implementing the *SIMPLEC* method (Van Doormal and Raithby, 1984), the following relationships between the correction velocities and pressure are obtained:

$$u_p' = D_p^u\left(\overline{p}_p'-\overline{p}_E'\right)^u; \quad v_p' = D_p^v\left(\overline{p}_S'-\overline{p}_p'\right)^v \\ u_{1p}' = D_p^u\left(\overline{p}_{1p}'-\overline{p}_{1E}'\right)^u; \quad v_{1p}' = D_p^v\left(\overline{p}_{1S}'-\overline{p}_{1p}'\right)^v \tag{B.31}$$

where

$$D_p^u = \frac{\left(h_p^u\,\delta r_p^u\right)}{A_p^u - \sum_{nb} A_{nb}^u}; \qquad D_p^v = \frac{\left(h_p^v\, r_p^v\,\delta\theta_p^v\right)}{A_p^v - \sum_{nb} A_{nb}^v}; \text{ with } \sum_{nb} A_{nb} = A_E + A_W + A_N + A_S \tag{B.32}$$

Substitution of the assumed flow fields into the continuity equation leads to the following pressure correction equations:

<u>zeroth-order equation:</u>

$$A_p^P \bar{p}'_p = A_E^P \bar{p}'_E + A_W^P \bar{p}'_W + A_S^P \bar{p}'_S + A_N^P \bar{p}'_N + S_p^P \tag{B.33}$$

<u>first-order equation:</u>

$$A_p^P \bar{p}'_{1p} = A_E^P \bar{p}'_{1E} + A_W^P \bar{p}'_{1W} + A_S^P \bar{p}'_{1S} + A_N^P \bar{p}'_{1N} + S_{1p}^P \tag{B.34}$$

where

$$\begin{aligned} A_p^P &= \sum_{nb} A_{nb}^P = A_E^P + A_W^P + A_S^P + A_N^P \\ A_E^P &= \left(\bar{\rho}\,h\right)_e^P \delta r_p^P\, D_p^u; \qquad A_S^P = \left(\bar{\rho}\,h\right)_s^P r_s^P\,\delta\theta_p^P\, D_p^v \\ A_W^P &= \left(\bar{\rho}\,h\right)_w^P \delta r_p^P\, D_W^u; \quad A_N^P = \left(\bar{\rho}\,h\right)_n^P r_n^P\,\delta\theta_p^P\, D_N^v \end{aligned} \tag{B.35}$$

and the mass flow source terms are:

$$S_p^P = -\left(m_e^* - m_w^* + m_n^* - m_s^*\right)^P \tag{B.36}$$

$$S_{1p}^P = -\left[\left(m_{1e}^* - m_{1w}^* + m_{1n}^* - m_{1s}^*\right)^P + i\,\sigma\left\langle\bar{\rho}\,h\right\rangle_1^P r_p^P\,\delta r_p^P\,\delta\theta_p^P\right] \tag{B.37}$$

are evaluated with the (*) fields.

THE NUMERICAL SOLUTION PROCEDURE

The governing difference equations on the bearing film lands are solved iteratively. The steps in the numerical solution are summarized as follows:

a) Initial guesses for the recess pressures and the film fields for pressure ($\bar{P}$ *), velocities (U*, V*) and temperature ($\bar{T}$) are calculated.
b) The coefficients for the circumferential momentum transport equation (B.5) along the first row of U-control volumes (off the bearing recess middle plane) in the film lands between recesses are calculated, and the transport equation is solved using the tridiagonal matrix algorithm (TDMA).

c) The treatment under step b) is repeated for the radial momentum transport equation along the second row of V-control volumes, equation (B.13). Note that the line-by-line solution procedure sweeps in the radial direction from the recesses towards the bearing outer (and inner) planes.
d) The coefficients of the pressure correction equation (B.33) on the first row (coinciding with the first U-control volume row but between the first and the second V-control volume rows) are calculated and the pressure correction equation is solved by the TDMA procedure.
e) The velocities and pressures upstream and along the current row are corrected by adding the correction fields to the estimated flow fields (U*, V*, $\overline{P}$ *).
f) The coefficients of the energy equation (B.21) are calculated, and the equation is solved using the TDMA to render the temperature field in the T-control volume row. The fluid properties, functions of the local pressure and temperature, are immediately updated at this stage.
g) Steps b) to f) are repeated for all subsequent rows until the bearing exit boundaries (inner and outer) are reached. The inlet velocities at the recess boundaries and entering the film lands are obtained by satisfying the local flow continuity constraint at the control volumes facing the recess boundaries.
h) The iterative procedure above is repeated until the sum of (absolute value) residuals of mass flows on the control volumes $\left[\sum_{\text{domain}} S_p^P, \left\| \sum_{\text{domain}} S_{1p}^P \right\| \right]$ is below a prescribed tolerance value, typically 0.1% of the global mass flow rate.
i) Once a solution to the flow field in the film lands has been obtained, the recess temperatures are calculated through the global energy balance equation at the bearing recesses.
j) The zeroth-order flow rates from recess into the film lands are evaluated and compared with the orifice flow rates. In general, a difference exists between these two flow rates, and a Newton-Raphson scheme is implemented to update the recess pressures and to satisfy the flow continuity requirement at each recess. A thorough discussion on this step is given in the main text of the report.

Steps (b) through (j) are successively repeated until the difference of the orifice inlet and exit flow rate for each recess is below a tolerable value (about 0.6%).

The governing difference equations on the bearing film lands are solved iteratively. An approximate solution for the flow field variables is used to initiate the calculations. The velocity components are first calculated from the circumferential and radial momentum transport equation using an estimated pressure field, and then a pressure correction equation based on the continuity equation provides corrected pressure and velocity fields. Solution to the energy transport equation also renders an estimate of the temperature field. The updated pressure and velocity fields are substituted again into the momentum and pressure correction equations resulting in (generally) more accurate velocity and pressure field solutions.